UNIVERSITY OF PISA

Department of Information Engineering

PhD PROGRAM IN INFORMATION ENGINEERING (XXXII Cycle)

Radiofrequency Magnetic Field Devices for Biomedical Applications:

Magnetic Hyperthermia – Magnetic Resonance Imaging – Wireless Power Transfer

Tutors:

Prof. Ing. Agostino Monorchio

Ing. Nunzia Fontana

Ing. Giulio Giovannetti

Candidate:

Danilo Brizi

The Coordinator of the PhD Program

Prof. Fulvio Gini

Academic Year: 2018/2019

ACKNOWLEDGMENTS

Pursuing a Ph.D. degree is an unpredictable and fascinating journey, which I had the huge honor to share with wonderful people that helped me to grow enormously from a personal and professional point of view.

And, in this sense, I first have to address my personal thanks and deep gratefulness to my supervisor and mentor, Prof. Agostino Monorchio. His encouragements and continued scientific and human support have been a stable column, always present during this journey, to lean against in the toughest moments. I have learned a lot from him, not only as an engineer but also as an individual.

Even if he is not among my tutors, I would wish to express my sincere gratitude to Prof. Gianluca Lazzi. He represented a significant component in my Ph.D., since he hosted and supervised me during my 1-year visiting period in his lab. This period definitely improved my professional skills and, more important, I had the luck to be involved in extremely fascinating and cutting-edge research activities.

A special thanks have to be also addressed to my others tutors, Ing. Nunzia Fontana and Ing. Giulio Giovannetti: I could always counted on their help on my way. Especially with Nancy, we have shared countless (and funny!) experimental experiences that enriched me a lot.

Then, to all the MRLab and IBT members and friends: the human bonds I share with you made each working day a pleasure rather than a duty.

Finally, because the best goes last, I would like to thank my family: my mother Mariella, my father Enzo and my sister, Giusy, together with her husband, Luciano, and their beautiful and sweet children, Giulia and Matteo. Without them, nothing of what I have had the privilege to do would have been possible, from all the points of view. Simply, I love you.

SUMMARY

Electromagnetism is the branch of physics involving the analysis of electromagnetic fields (EMF) and their propagation. Since the 19th century, a huge development has been made in this topic and it is still currently exponentially growing. Personalities like Ampere, Biot, Savart, Faraday, Maxwell, Tesla provided all the physical and mathematical basis to analyze and describe electromagnetic static and dynamic phenomena in vacuum and inside generic media [1].

As a matter of fact, electromagnetism and biological life share a strong and deep interconnection: all the living processes are originating upon a fundamental electromagnetic event, precisely a change in the cellular membrane electrical potential [2], [3]. Hence, biological life is unsurprisingly affected by such interactions in a so complex way that it was required to define a specific discipline to study, investigate and characterize them: bioelectromagnetism. It is defined as all the electromagnetic phenomena involving living beings and it claims a very long history. It is meaningful to discover that the first written evidence of the therapeutic use of electromagnetic fields dates back even to ancient Egyptians (4000 B.C.); in a hieroglyph, the benefic effect produced by the electric shock of a particular catfish for chronic headaches is reported [2]. Obviously, it took a long time before bioelectromagnetism started to be studied in a proper scientific way: most of the developments in this discipline have been carried out along the last century, as it happens for all the major contributions in medical sciences.

Today, it is well known that living beings continuously produce electromagnetic waves: for instance, the heart and the brain emit electric and magnetic signals that can be registered and exploited to infer important information about the physiological status of such organs. However, as well as biological activities produce EMF, so scientists have learned to use EMF to excite tissues and develop new and powerful therapeutic and diagnostic devices. Nowadays, it is unimaginable to think about healthcare without a number of electromedical instrumentation: electrocardiograms, electroencephalograms, defibrillators, radiofrequency and microwaves ablation and hyperthermic devices, magnetic resonance imaging scanners, pacemakers, biomedical implants.

From the general electromagnetic theory, it descends that electric and magnetic fields are strictly correlated each other; in particular, Maxwell equations predict that they must coexist, thus there cannot be an electric field without its magnetic counterpart. However, for healthcare purposes, we tend often to separate the techniques that use the electric field from the ones employing magnetic field as therapeutic or diagnostic mean. This is due to the fact that tissues interactions are profoundly different in the two cases [4], pushing the research to develop applications for both these physical entities. In order to develop continuously novel healthcare devices, a large part of the electromagnetic spectrum has been already used: from DC to few GHz, every frequency range finds a peculiar and unique interaction with human beings.

In the present work, the attention is drawn towards magnetic field applications for biomedical devices, exploiting the radiofrequency (RF) range from 300 kHz to 300 MHz. In this range, a lot of different applications have been proposed in the literature; in particular, the dissertation will cover three main topics: Magnetic Particle Hyperthermia (MPH), Magnetic Resonance Imaging (MRI) and resonant inductive Wireless Power Transfer (WPT).

In detail, Chapter 1 is devoted to present the work about Magnetic Particle Hyperthermia developed in collaboration with the Italian National Research Council Institute of Clinical Physiology (IFC-CNR) and with the research center of Colorobbia S.p.A. (Ce.Ri.Col, Sovigliana Vinci, Firenze). We first address the development of a fast and efficient electromagnetic characterization method for colloidal magnetic fluids with nanoparticles, which is a fundamental step for optimizing their use [5]; secondly, the design of a novel focusing RF radiating system to perform safe and efficient hyperthermic treatments for superficial tumors is investigated [6], [7].

In Chapter 2, the inductive mutual coupling, arising when arrangements of multiple RF MRI coils are used, is faced. In particular, we propose an innovative approach to solve this issue, employing small spiral resonators, precisely designed and positioned between the RF coils. Hence, the electromagnetic characterization of the employed resonators has been firstly carried out, developing a method to extract an accurate and reliable lumped equivalent circuital model [8]. Then, this step has been followed by the analytical formulation of a

framework to design a decoupling filter using such resonators [9]–[12]; in particular, this study was conducted in collaboration with the University of L'Aquila (L'Aquila, Italy).

Chapter 3 introduces the topic about resonant inductive Wireless Power Transfer. We present the design of an extremely compact, low-frequency metasurface, able to bring significant benefits to WPT applications [13], [14], despite the ultra-thin thickness. After that, the possibility to finely control efficiency, gain and magnetic field distribution in a WPT device is investigated and an analytical framework to design arrays of concentric non-resonant loops for tunable WPT devices is presented [15]. The author has conducted the WPT research activities at the Keck School of Medicine of University of Southern California (Los Angeles, California, USA), under the supervision of Prof. Gianluca Lazzi, during a 1 year research appointment as a visiting Research Scholar (1 May 2018 – 30 April 2019).

LIST OF PUBLICATIONS

International Journals

1. D. Brizi, N. Fontana, G. Giovannetti, A. Flori, L. Menichetti, S. Doumett, G. Baldi, A. Monorchio., "A Novel Approach for Determining the Electromagnetic Properties of a Colloidal Fluid with Magnetic Nanoparticles for Hyperthermia Applications," *IEEE J. Electromagn. RF Microw. Med. Biol.*, vol. 2, no. 1, pp. 70–77, Mar. 2018.

2. D. Brizi, N. Fontana, F. Costa, and A. Monorchio, "Accurate Extraction of Equivalent Circuit Parameters of Spiral Resonators for the Design of Metamaterials," *IEEE Trans. Microw. Theory Tech.*, vol. 67, no. 2, pp. 626–633, Feb. 2019.

3. D. Brizi, N. Fontana, G. Giovannetti, L. Menichetti, L. Cappiello, S. Doumett, C. Ravagli, G. Baldi, A. Monorchio, "A Radiating System for Low Frequency Highly Focused Hyperthermia with Magnetic Nanoparticles," *IEEE J. Electromagn. RF Microw. Med. Biol.*, 2019, doi: 10.1109/JERM.2019.2945833.

4. D. Brizi, N. Fontana, F. Costa, G. Tiberi, A. Galante, M. Alecci, A. Monorchio, "Design of Distributed Spiral Resonators for the Decoupling of MRI Double-Tuned RF Coils," *IEEE Trans. Biomed. Eng.*, 2020, doi: 10.1109/TBME.2020.2971843.

5. D. Brizi, J. Stang, A. Monorchio, and G. Lazzi, "A Compact Magnetically Dispersive Surface for Low Frequency Wireless Power Transfer Applications," *IEEE Trans. Antennas Propag.*, 2020, doi: 10.1109/TAP.2020.2967320.

6. D. Brizi, J. Stang, A. Monorchio, and G. Lazzi, "On the Design of Non-Resonant Coils Planar Arrays for Tunable Wireless Power Transfer Applications," *IEEE Trans. Microw. Theory Tech.*, 2020, doi: 10.1109/TMTT.2020.2983145.

7. D. Brizi, N. Fontana, M. Tucci, S. Barmada, A. Monorchio, "A Spiral Resonators Passive Array for Resonant Inductive Wireless Power Transfer Applications with Limited Exposure to Electric Near Field", *IEEE Trans. Electromagnetic Compatibility, accepted for publication*.

International Conferences: Papers

8. D. Brizi, A. Monorchio, and N. Fontana, “A novel coil for highly focused magnetic hyperthermia with nanoparticles,” in *2017 IEEE International Symposium on Antennas and Propagation & USNC/URSI National Radio Science Meeting*, San Diego, CA, July 2017, pp. 1223-1224.

9. N. Fontana, F. Costa, D. Brizi, G. Tiberi, G. Galante, M. Alecci, A. Monorchio., “Decoupling of dual-tuned MRI coils by using distributed magnetic traps,” *12th Eur. Conf. Antennas Propag. EuCAP 2018*, London, April 2018, pp. 1-5.

10. D. Brizi, N. Fontana, F. Costa, G. Tiberi, and A. Monorchio, “On the Optimization of Distributed Magnetic Traps in MRI Coils Decoupling,” in *2018 IEEE International Symposium on Antennas and Propagation & USNC/URSI National Radio Science Meeting*, Boston, MA, July 2018, pp. 893-894.

11. D. Brizi, A. Monorchio, and G. Lazzi, “An Ultra-thin Low-frequency Metamaterial for Wireless Power Transfer Applications,” in *2018 IEEE International Symposium on Antennas and Propagation & USNC/URSI National Radio Science Meeting*, Boston, MA, July 2018, pp. 2555-2556.

12. N. Fontana, D. Brizi, F. Costa, G. Tiberi, and A. Monorchio, “On the Decoupling Robustness of Distributed Magnetic Traps in Biological Loaded Dual Tuned MR coils,” in *2019 IEEE International Symposium on Antennas and Propagation & USNC/URSI National Radio Science Meeting*, Atlanta, GA, USA, 2019, pp. 759-760.

13. D. Brizi, N. Fontana, S. Barmada, A. Monorchio, "A Multi-Transmitter Configuration for High-Safety Wireless Power Transfer Applications", *2019 International Applied Computational Electromagnetics Society Symposium (ACES)*, Miami, FL, USA, April 2019, pp. 1-2.

14. J. Stang et al., "Recent Advances in Computational and Experimental Bioelectromagnetics for Neuroprosthetics," *2019 International Conference on Electromagnetics in Advanced Applications (ICEAA)*, Granada, Spain, 2019, pp. 1382-1382.

15. F. Costa et al., "Wireless Detection of Water Level by Using Spiral Resonators Operating in Sub-Ghz Range," *2019 IEEE International Conference on RFID Technology and Applications (RFID-TA)*, Pisa, Italy, 2019, pp. 197-200.

International Conferences: Abstracts

16. D. Brizi, J. Stang, A. Monorchio, G. Lazzi, "Planar array of non-resonating concentric coils for high-flexibility Wireless Power Transfer applications", *URSI EM Theory Symposium, EMTS 2019*, San Diego, CA, May 2019.

17. D. Brizi, J. Stang, A. Monorchio, G. Lazzi, "Array of Non Resonant Coils for Receiver Size Reduction in Wireless Power Transfer Applications", *2019 IEEE International Symposium on Antennas and Propagation & USNC/URSI National Radio Science Meeting*, July 2019, Atlanta.

18. M. Machnoor, D. Brizi, J. Stang, G. Lazzi, "Maximization of the Efficiency in a Multi-Coil Wireless Power Transfer Systems for Biomedical Applications", *2019 IEEE International Symposium on Antennas and Propagation & USNC/URSI National Radio Science Meeting*, July 2019, Atlanta.

List of publication is updated to Apr. 2020

LIST OF ABBREVIATIONS

AC: *Alternating Current*

DC: *Direct Current*

DLS: *Dynamic Ligth Scattering*

DMT: *Distributed Magnetic Trap*

DT: *Double Tuned*

EMF: *Electro-Magnetic Field*

FID*: Free Induction Decay*

FOV: *Field of View*

FFR: *Field Free Region*

ICNIRP: *International Commission on Non-Ionizing Radiation Protection*

ICP-OES: *Inductively Coupled Plasma Optical Emission Spectroscopy*

IEC: *International Electrotechnical Commission*

LRT: *Linear Response Theory*

MPH: *Magnetic Particle Hyperthermia*

MRI: *Magnetic Resonance Imaging*

NMR: *Nuclear Magnetic Resonance*

PEC: *Perfect Electric Conductor*

PLGA-PEG: *Poly Lactic acid-co-Glycolic Acid Polyethylene Glycol*

RF*: Radio Frequency*

SAR: *Specific Absorption Rate*

SNR: *Signal-to-noise ratio*

SR: *Spiral Resonator*

WPT: *Wireless Power Transfer*

XRD: *X-Ray Diffraction technique*

TABLE OF CONTENTS

1 CHAPTER 1: MAGNETIC HYPERTHERMIA WITH NANOPARTICLES

1.1 Introduction

Since long time, it has been established in the scientific community that hyperthermia can have positive therapeutic effect on tumors; as a matter of fact, a mild temperature rise (up to 47 °C, above whom biological tissues undergo to a direct necrosis due to thermal ablation) is responsible for cancerous cells thermo-sensibilization, thus making them more susceptible to drugs' effect or additional radiations. Thus, hyperthermia is generally integrated with other widely diffused therapies, such as chemotherapy and radiotherapy, mitigating their severe side effects and enhancing their effectiveness [16], [17]. Notably, hyperthermia has a long story in clinical applications. Several methodologies have been already developed, exploiting different physical principles to deliver heat to target tissues: ultrasound, capacitive, microwave and magnetic particle hyperthermia (MPH) are some of the most popular and diffused techniques.

In particular, Magnetic Particle Hyperthermia (MPH) – which employs nanoparticles as a carrier to induce localized heating in a pathological area – is rapidly emerging as a potential and efficient cancer therapy thanks to its unique advantages [18]–[26]. Indeed, the very low frequency of the applied magnetic field (hundreds of kHz) allows excellent penetration depths; moreover, nanoparticles can be functionalized (i.e., the surface can be equipped with drugs or specific membrane receptors), thus achieving a targeting capability at cellular level. Instead [27], microwave hyperthermia suffers from poor penetration depth due to the high operative frequencies (from hundreds of MHz to few GHz); capacitive hyperthermia produces a non-uniform heating in tissues characterized by a high value of impedance (i.e. bones); similar drawbacks can be highlighted also for ultrasound hyperthermia, where the interfaces between tissues with different values of acoustic impedance reflect back the energy. Therefore, MPH can be a valuable alternative to other hyperthermic techniques.

Physically, magnetic nanoparticles are characterized by high values of the magnetic susceptibility loss component; hence, they strongly interact with a radiofrequency magnetic field in the range of hundreds of kHz [28]–[30], releasing a significant heat amount. As it will be widely discussed in the following, the heat release optimization – fundamental for effective clinical treatments – requires a fine tuning between the behavior of nanoparticles' complex

magnetic susceptibility and the distribution, frequency and amplitude of the applied radiofrequency (RF) magnetic field [31], [32].

1.2 Magnetic Nanoparticles and Interactions with an RF magnetic field

Several typologies of synthesized magnetic nanoparticles can be found in the literature, differing for chemical composition and shape; the most common materials are iron oxides (mostly, maghemite and magnetite), cobalt and gold ferrite, in a spherical or cubic aspect [32]. Nonetheless, they all share some features: nanometric dimension (in the range of 1:100 nm) and a strong magnetic behavior (i.e., they vigorously interact with an external RF magnetic field). Evidently, chemical composition and shape primarily affect their physical properties, especially regarding the spectral magnetic susceptibility behavior.

For their interesting properties, colloidal suspensions of magnetic nanoparticles have been quickly adopted in clinical environment, in combination with electromagnetic fields (EMF). Generally speaking, two main modalities are employed to deliver a fluid containing magnetic nanoparticles inside tissues: a direct percutaneous injection or a systemic administration through an opportune nanoparticles' surface functionalization [16]. Nevertheless, nanoparticles must satisfy a fundamental requisite to be employed inside biological tissues, i.e. biocompatibility. Thus, since they are non cytotoxic and well-tolerated, iron oxides (magnetite and maghemite) with an opportune surface coating (usually, PLGA-PEG) are prevalently used.

As quite natural, one of the first clinical applications of nanoparticles was related to MRI imaging [33]. Indeed, they introduce dishomogenities in the MRI static field due to their magnetic behavior, modifying accordingly the spin-spin relaxation time (T_2). Hence, they can be used as a powerful contrast agent, especially for liver lesions detection (Fig. 1.1).

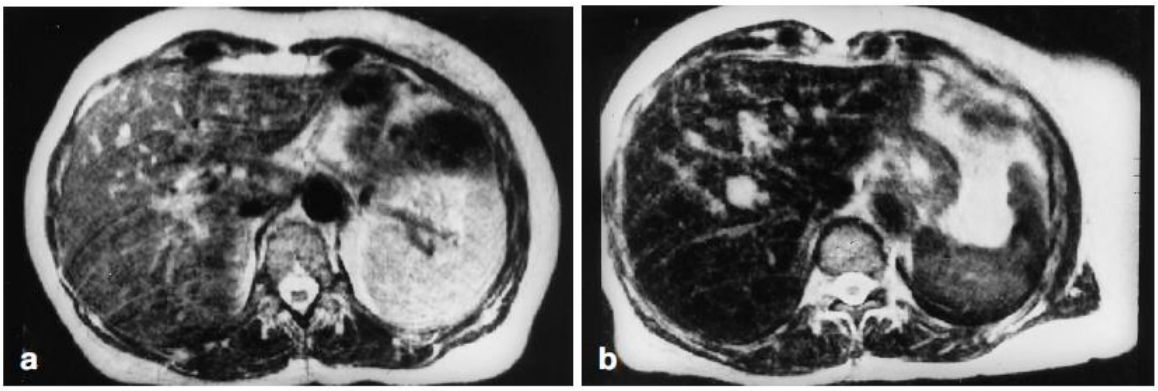

Figura 1.1 - Detection of malignant lesions with iron oxide nanoparticles: (a) normal image; (b) T_2-weigthed image [33].

However, as addressed in this work, they are mainly employed for hyperthermia, since their complex magnetic susceptibility shows a significant loss component. Interestingly, as we have already briefly mentioned, nanoparticles can be also equipped with drugs to be released when exposed to the RF magnetic field. Hence, multifunctional and theranostic platforms can be realized [34], [35] (Fig. 1.2).

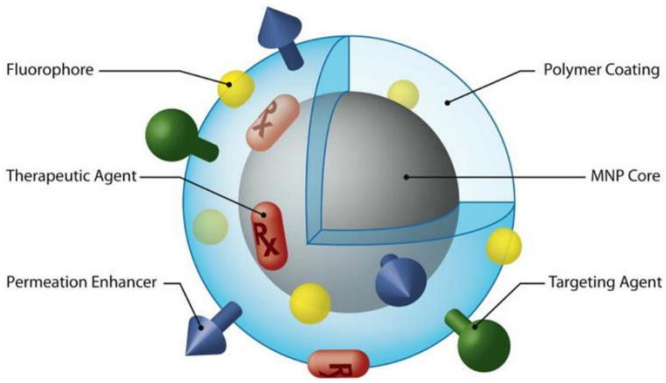

Figura 1.2 – Schematic representation of a nanoparticle's surface functionalization.

Nonetheless, the knowledge of the particles response when exposed to an external RF magnetic field is crucial in order to fully exploit their thermic potentiality and to design an effective radiating system. In other words, we need to characterize the frequency behavior of the complex magnetic susceptibility from which the heat release is dependent.

As generally accepted in the scientific community, the Linear Response Theory (LRT) [31] can be applied to describe the complex magnetic susceptibility of a fluid containing

nanoparticles exposed to an external RF magnetic field, under the hypothesis of low amplitude and for a limited range of frequencies [36]. Nevertheless, such conditions are typical for common magnetic hyperthermia applications, due to exposition limit guidelines [37]. These limits are also responsible for preventing MPH being used for direct tissue ablation, since very high field values would be required. The single nanoparticle can be represented as a magnetic dipole, which undergoes to a Debye single order relaxation phenomenon. Hence, as reported in [31], the complex magnetic susceptibility can be expressed as follows:

$$\chi(f) = \chi'(f) - j\chi''(f) \tag{1.1}$$

$$\chi'(f) = \frac{\chi_0}{1+(2\pi f\tau)^2} \tag{1.2}$$

$$\chi''(f) = \chi_0 \frac{2\pi f\tau}{1+(2\pi f\tau)^2} \tag{1.3}$$

where χ_0 is the equilibrium susceptibility value and τ(s) is the effective relaxation time of the fluid, obtained as a superposition of Brownian and Néel relaxation times (τ_B and τ_N, respectively). The Brownian relaxation involves the mechanical movement of the entire nanoparticle in the solution whereas Néel relaxation concerns the interaction of the RF magnetic field with the magnetic dipole that represents each single nanoparticle. These two physical phenomena are predominant under low field amplitude conditions. As already mentioned, the attention is directed to the frequency range around hundreds of kHz for hyperthermia purpose; however, it may be important knowing that magnetic nanoparticles normally exhibit further susceptibility peaks at higher frequencies (GHz range) due to ferromagnetic resonance [18]. Since these high frequency phenomena do not affect the magnetic susceptibility in the hyperthermic range, they are usually not included in the model.

The Brownian relaxation time can be expressed as [38], [39]:

$$\tau_B = \frac{3V_H\eta}{k_BT} \tag{1.4}$$

where V_H (m^3) is the hydrodynamic volume of the nanoparticles, η (Pa s) is the sample viscosity, k_B (m^2 kg s^{-2} K^{-1}) is the Boltzmann constant and T (K) the temperature of the sample.

Instead, the following equation describes the Néel relaxation time [38]:

$$\tau_N = \tau_0 e^{KV_C/k_B T} \tag{1.5}$$

where τ_0 (s) is the attempt time, K (J m^{-3}) is the anisotropy constant of the nanoparticles and V_C (m^3) is the magnetic volume of the nanoparticle's core.

Finally, the effective relaxation time τ is obtained as:

$$\tau = \left(\frac{1}{\tau_N} + \frac{1}{\tau_B}\right) \tag{1.6}$$

Under low field amplitude hypothesis, we can theoretically assume the validity of the Rosensweig's equation for the Specific Absorption Rate (SAR) release (W/kg) [31]:

$$SAR = \frac{\mu_0 \pi \chi'' f H_0^2}{\phi \rho} \tag{1.7}$$

where we indicate with μ_0 (H/m) the vacuum magnetic permeability, with χ" the imaginary component of the sample complex magnetic susceptibility (loss component), with ϕ the volume fraction and ρ (kg/m^3) the density of nanoparticles, whereas f (Hz) and H_0 (A/m) are the frequency and the amplitude of the applied field, respectively.

1.3 A novel Approach for the Electromagnetic Properties Determination of a Colloidal Fluid with Magnetic Nanoparticles

As described in eq. (1.7), particles power release is linearly dependent from the magnetic susceptibility loss component χ". In the perspective of a hyperthermic treatment, this aspect is of crucial relevance; indeed, the selection of the frequency, which corresponds to the loss component highest value, would maximize the heat release (and, consequently, the hyperthermic treatment effectiveness). Hence, the magnetic susceptibility estimation of the employed magnetic fluid is essential.

Despite the relatively simple mathematical modeling of the phenomenon, to the best of our knowledge, there is a lack in literature regarding magnetic susceptibility estimations in an environment able to mimic the real clinical application of magnetic hyperthermia. An ideal sample should present clinical exposure conditions for magnetic field (in particular, frequency in the range of hundreds of kHz), clinically deliverable nanoparticles concentration (few mg/mL) and a medium able to mimick biological tissues.

On the contrary, although several works addressed the problem of the direct magnetic susceptibility measurements over a wide range of frequency (carried out with coaxial cable configurations), they typically evaluated frequency range (from MHz to GHz) far away from magnetic hyperthermia conditions [29], [30], [40]–[42]. Further, some groups achieved the low frequency complex susceptibility characterization, but resorting to highly expensive instrumentation (i.e. susceptometers) [38], [43]; besides, also AC magnetometers have been used to measure SAR released by nanoparticles under a radiofrequency magnetic field exposition in a quite large frequency band [44]–[46]; however, in all the cases, no particularly realistic assumption was adopted about the suspension medium.

In order to overcome these limits, we propose a general analytical method to determine the magnetic properties of a colloidal magnetic fluid, starting from *in vitro* Specific Absorption Rate (SAR) measurements, easier to obtain compared to a direct susceptibility probing [5]. More importantly, our aim is evaluating nanoparticles behavior in a phantom mimicking biological tissues, using a mixture of water, agar and nanoparticles with a typical clinical concentration. By adjusting the agar concentration and the conductivity of the sample, it is also possible to replicate specific tissue properties [47].

In detail, we first process experimental SAR measurements obtained by exposing a magnetic fluid sample to an RF magnetic field at different operative conditions (amplitude and frequency). Afterwards, we analytically extract the magnetic susceptbility values, through Linear Response Theory indirect equations.

1.3.1 Nanoparticles sample

In order to apply the proposed method, we fabricated a magnetic fluid sample. It consisted in a vial with a total volume V_{vial} = 2 cm^3, filled with water, agar and magnetite (Fe_3O_4) nanoparticles. The overall mass of the fluid was m_{vial} = 1.04 g, thus the density was ρ_{vial} = 0.52 g/ cm^3. The iron concentration was determined by ICP-OES after acidic digestion of the sample with nitric (at 65% w/w) and hydrochloric acids (at 37% w/w). Specifically, magnetite nanoparticles were at the 0.12% of volume fraction (ϕ = 0.0012), whereas the agar was at the 4%. Considering a density for the magnetite of $\rho_{Fe_3O_4}$ = 4.9 g/ cm^3, the total magnetite mass can be calculated as: $m_{Fe_3O_4} = \rho_{Fe_3O_4} \times V_{vial} \times \phi$ = 0.0118 g (equal to 5.9 mg/mL).

Precisely, uncoated magnetite nanoparticles were produced by using polyol technique; each single nanoparticle presented a mean diameter of 10 ± 2.6 nm, measured with x-ray diffraction technique (XRD). They were organized in the form of nanoclusters, whose mean size and polydispersity index were determined by dynamic light scattering (DLS), resulting in 56.9 ± 0.4 nm and 0.16 ± 0.01, respectively (indicating a narrow size distribution). Finally, the clusters were externally coated with a biocompatible polymeric PLGA-PEG shell.

1.3.2 Magnetic susceptibility characterization method

Since our procedure is based on the nanoparticles power release evaluation, we first exposed the sample at different RF magnetic field amplitudes and frequencies, acquiring the related *in vitro* SAR measurements (Table 1.1). We used a commercial heat station (Fives Celes Lu C2 Power Supply, Fivesgroup, France) as an inductive system. The magnetic fluid was contained in the vial placed in the center of the inner volume of a solenoid (Fig. 1.3).

We derived SAR measurements (W/g of Fe_3O_4) from temperature monitoring (recorded every second), through an optical fiber thermometer (CEAM, Vr18CR-PC). We exploited the initial slope of the heating process:

$$SAR = \frac{CV}{m_{Fe_3O_4}} \frac{dT}{dt} \tag{1.8}$$

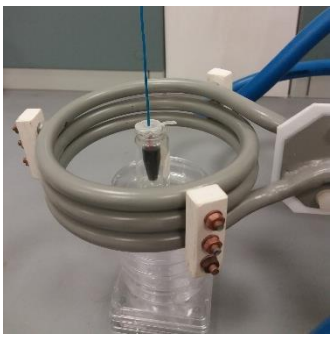

Fig. 1.3 Experimental set-up for SAR measurements.

Table 1.1
Experimental SAR Measurements Obtained *in vitro* (per gram of magnetite)

Field Amplitude (kA/m)	Field Frequency (kHz)	SAR (W/g $_{Fe3O4}$)
9.3	103	14.8
9.0	183	30.0
10.7	203	31.8
7.9	254	28.5
4.1	340	24.5
5.7	340	30.9
7.4	340	46.4
4.8	423	21.1
6.1	423	28.6
7.3	423	45.9
8.8	423	71.3

where C (J/L/K) is the specific heat capacity of the sample, V (L) is the sample volume, and $m_{Fe_3O_4}$ is the mass of iron oxide in the sample. Notably, the sample overall specific heat capacity is well approximated by the water value, since it has the major contribution with respect to the other components.

Instead, from eq. (1.7), we indirectly obtained the values of the imaginary component χ'' for each experimental combination of frequency and amplitude (Table 1.1). As can be seen from the data, our experimental conditions respected the hypothesis of low amplitude of the magnetic field; therefore, it was theoretically possible to apply the mathematical modeling previously described on our sample of magnetite nanoparticles.

From experimental evidence, it is well known that the presence of agar increases the sample viscosity, thus suppressing the free movement of nanoparticles (Brownian relaxation).

Hence, we considered only the Néel relaxation phenomenon, as usual in a clinical environment [36], [48]–[52].

Exploiting eq. (1.3), we combine two χ" values obtained from SAR measurements at two distinct frequencies (f_1 and f_2) in a second order equations system, thanks to which extracting χ_0 and τ (the latter two considered independent from frequency):

$$\chi_0 = \frac{\chi_1''[1+(2\pi f_1\tau)^2]}{(2\pi f_1\tau)} \tag{1.9}$$

$$\tau = \sqrt{\frac{\chi_1'' f_2 - \chi_2'' f_1}{4\pi^2 f_1 f_2(\chi_2'' f_2 - \chi_1'' f_1)}} \tag{1.10}$$

In order to give robustness to the extraction method, we calculate the mean values $\overline{\chi_0}$ and $\bar{\tau}$ using all the combination of frequency couples available from experimental set-up. Under the LRT hypothesis, we construct the curve described in eq. (1.3). Then, to refine the result, we optimized $\overline{\chi_0}$ and $\bar{\tau}$ through a distance least square minimization between this analytical curve and the experimental loss component data indirectly derived from eq. (1.7). Finally, we also obtain the frequency behavior of the magnetic susceptibility real term substituting $\overline{\chi_0}$ and $\bar{\tau}$ in equation (1.2). The complex magnetic permeability simply follows.

$$\mu_r(f) = 1 + \chi(f) \tag{1.11}$$

It must be noticed that the procedure is very rapid and general: it can also be applied to any type of magnetic nanoparticles.

1.3.3 Validation of the analytical method

We replicated the SAR experimental measurements with a commercial electromagnetic simulation software based on the method of Moments (Feko Suite, Altair, Troy, MI, USA), using the magnetic permeability values extracted with the proposed analytical approach and the dielectric properties of the water (ε_r = 80 and σ_s = 0.6 S/m) to describe the fabricated magnetic fluid sample. Our aim is to verify if we can obtain the same SAR values we experimentally measured, thus validating the proposed characterization method.

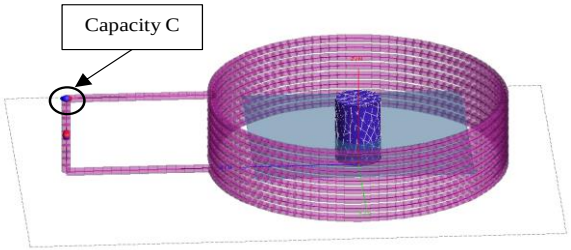

Fig. 1.4 3D CAD representation of the experimental set-up.

We designed a solenoid similar to the one experimentally used in terms of electromagnetic properties (Fig. 1.4). Through the capacitive load *C*, we tuned the coil to resonate at each experimental frequency. Then, we adjusted the coil input power to replicate also the magnetic field amplitudes reached in every experimental SAR measurement (Table 1.1).

We modeled the nanoparticles vial with a cylinder, placed in the center of the solenoid, assigning to it the extracted complex magnetic permeability (eq. (1.11)).

Thereafter, we performed numerical simulations for each operative condition reported in Table 1.1, and we calculated SAR taking into account both electric and magnetic losses [53]:

$$SAR = \frac{\sigma_s |E|^2}{2\rho_{vial}} + \frac{\sigma_m |H|^2}{2\rho_{vial}} \tag{1.12}$$

where E (V/m) and H (A/m) are the electrical and magnetic field amplitudes, whereas ρ_{vial} is the density of the sample contained in the vial. The electrical and magnetic conductivities, σ_s and σ_m, can be expressed as follows:

$$\sigma_s = \omega \varepsilon_0 \varepsilon_r tan\delta_s \tag{1.13}$$

$$\sigma_m = \omega \mu_0 \mu_r tan\delta_m \tag{1.14}$$

in which $tan\delta_s$ and $tan\delta_m$ are the electric and magnetic loss tangent, while ε_r and μ_r are the sample dielectric relative permittivity and magnetic relative permeability, respectively. It must be noted that the numerical SAR estimations described in (1.12) are given per gram of fluid. In order to be compared with the values reported in Table 1.1 they must be converted to per gram of magnetite.

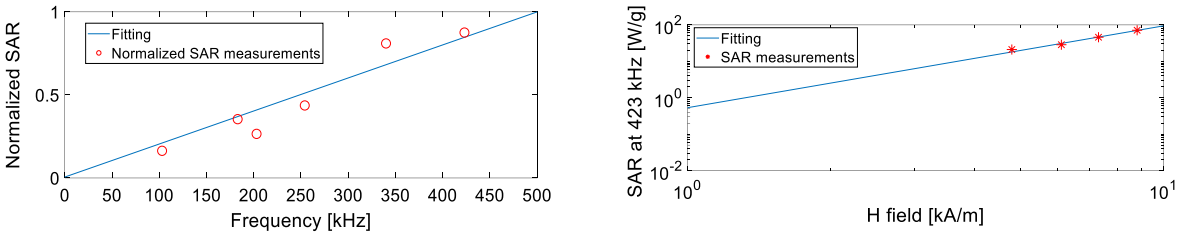

(a) (b)

Figure 1.5 (a) Linear dependence of the SAR measurements from the frequency. (b) Quadratic dependence of the SAR measurements from the amplitude of the magnetic field.

1.3.4 Results

We studied the behavior of the available SAR experimental measurements versus the frequency and versus the amplitude of the RF magnetic field in order to verify the validity of the Rosensweig's equation (1.7), which is the basis of the proposed method. In particular, we firstly normalized the SAR data with the square of the applied amplitude of the magnetic field: in this way, we obtained a new data set dependent only from the frequency. Starting from this new data set, we performed a polynomial fitting, obtaining a linear function ($f(x) = 0.002x$), as expected (Fig. 1.5(a)).

Then, we replicated the procedure in order to display the dependence of the SAR measurements on the square amplitude of the magnetic field; therefore, we fitted the data with a power law model. SAR measurements at 423 kHz have a dependence with the amplitude of the magnetic field slightly more than quadratic ($f(x) = 0.533x^{2.247}$), thus confirming a good agreement with the theoretical model of eq. (1.7) (Fig. 1.5(b)). This analysis confirmed and validated the LRT adoption in order to extract the complex magnetic susceptibility values.

Fig. 1.6(a) reports the loss component values χ'' extracted from the direct inversion of eq. (1.7), using the experimental SAR values. Then, as explained in the procedure, we extracted the different τ and χ_0 values (eq. (1.9) and (1.10)). In particular, only valid couples were considered, discarding those which make the argument of eq. (1.10) negative. It must be noted that the size and the shape of the nanoparticles constituting the sample will present a

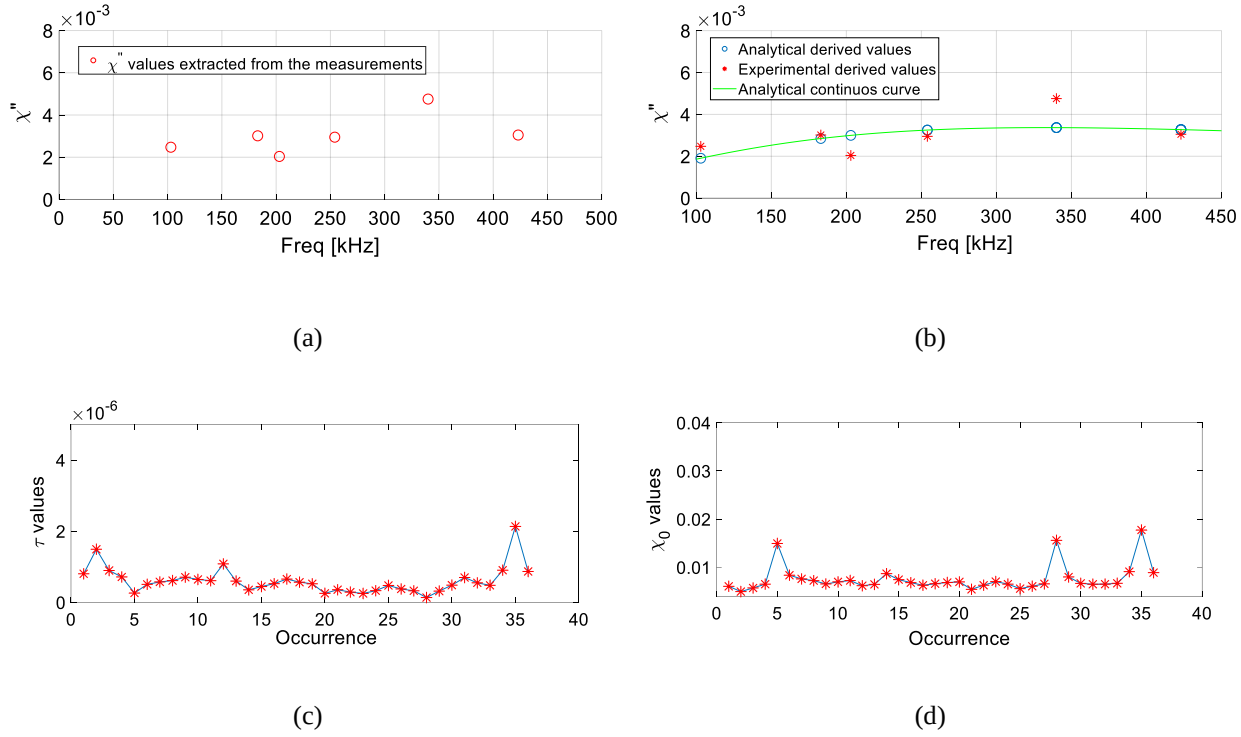

Figure 1.6 (a) Imaginary component of complex magnetic susceptibility extracted from inverting (1.7), averaging for 340 kHz and 423 kHz (multiple acquisitions). (b) Comparison between experimentally derived loss component values and the analytical curve obtained with our procedure. (c) and (d) τ and χ_0 vectors, extracted from experimental loss component values following the proposed analytical approach.

certain distribution, simply due to production issues. As a consequence, in general both τ_B and τ_N will vary (eq. (1.4) and eq. (1.5)). Nevertheless, as the following graphs (Fig. 1.6 (c) and (d)) show, the series of the extracted χ_0 and τ had a small range of variability, confirming that the size distribution of the nanoparticles is narrow. The obtained mean values, $\overline{\chi_0}$ and $\bar{\tau}$, resulted in 0.0076 and 6.055×10^{-7} s, respectively. Finally, in order to make the fitting more robust, we performed the refinement of $\overline{\chi_0}$ and $\bar{\tau}$ minimizing the distance between the analytical curve (obtained through eq. (1.3)) and the experimental values (least square algorithm), obtaining 0.0067 and 4.791×10^{-7} s. The optimized fitting curve is showed in Fig. 1.6 (b). Therefore, we observed that, for our specific sample of nanoparticles, an RF magnetic field in the range of frequencies around 340 kHz corresponds to the best heating conditions, where the maximum of the susceptibility loss component is achieved.

After that, we presented the analytical characterization of the nanoparticles of magnetite,

performed with our analytical procedure, in terms of the complex magnetic permeability (Table 1.2). These values were calculated using eq. (1.2), eq. (1.3) and eq. (1.11).

Table 1.2
Complex permeability values extracted through the analytical method

Field Frequency	μ_r'	μ_r''
103	1.0061	0.0019
183	1.0052	0.0028
203	1.0049	0.0030
254	1.0043	0.0033
340	1.0033	0.0034
423	1.0026	0.0033

Finally, we performed numerical simulations in order to validate our analytical approach based on the SAR experimental measurements (as described in the previous subsection). In particular, the numerical software, when implementing eq. (1.12), considers the density of the overall fluid, ρ_{vial}. This means that, in this way, the results would be SAR estimation per gram of fluid. In order to make comparable the experimental SAR (given as W/g of magnetite) and the numerical one, the SAR equation implemented by the software was multiplied by the factor $m_{vial}/m_{Fe_3O_4}$ = 88.14. We obtained a satisfying agreement between the experimental results and the analytical modeling, thus validating our proposed approach (Fig. 1.7).

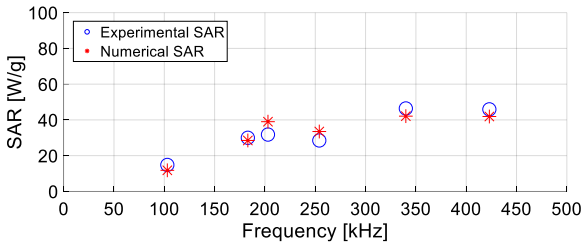

Figure 1.7. Comparison between numerical and experimental SAR measurements.

1.3.5 Conclusions

In this work, we proposed a general analytical approach to determine the electromagnetic properties of a colloidal magnetic fluid with nanoparticles and agar.

The knowledge of the electromagnetic properties is useful to predict the behavior of the nanoparticles at different radiation settings. In particular, this enables to find out the best

heating condition in the context of magnetic hyperthermia treatments. In our study, we were able to set the best operative range of frequencies for our specific sample of nanoparticles. It must be pointed out that our method can be a rapid and alternative procedure compared to the direct measurement of magnetic permeability. Moreover, it is possible to apply the method for any type of magnetic nanoparticles and to mimic tissues-like environments, exploiting agar properties. Finally, we validated the analytical approach by an electromagnetic simulation software, which is based on the Method of Moments. We successfully replicated the experimental SAR measurements via numerical approach, demonstrating that the analytical extraction of the nanoparticles' magnetic permeability is feasible and effective. The development of standardized methods for the characterization of the nanoparticles, combined with an optimal design of clinical RF coils, can enable the widespread adoption of the magnetic hyperthermia for an efficient cancer treatment. Furthermore, the use of numerical software in this kind of applications will allow efficient and low-cost experimental set-up planning for magnetic hyperthermia treatments. To conclude, the numerical approach will also support the development of new and innovative nanostructured hyperthermic agents, opportunely modifying the analytical modeling of the nanoparticles' behavior.

1.4 A Radiating System for Low Frequency Highly Focused Hyperthermia with Magnetic Nanoparticles

Despite the described advantages compared to existing methodologies, MPH presents also critical aspects to be carefully considered. The principal risk factor is the MPH fluid diffusion towards regions adjacent to the tumor area (i.e., outside the therapeutic target), which is still an open problem. Indeed, the concurrent presence of a radiofrequency magnetic field and a magnetic fluid in a healthy region can lead to unwanted hyperthermic effects and local cellular damages. In particular, the treatment of abdominal lesions represents a crucial issue due to the proximity of sensible organs (liver and kidneys), whose biological function is the MPH fluid extraction from the vascular system. Secondly, the lack of RF magnetic field focusing causes a significant RF exposition for healthy tissues; notably, several side effects

have been reported in the main international guidelines and in the literature, especially with respect to undesired stimulation of peripheral nerves and muscles [37], [54]. Unfortunately, it is a matter of fact that the focusing of a very low frequency magnetic field (hundreds of kHz) on a delimited area is difficult due to the respective huge wavelength.

So far, the most common MPH works presented in literature fail to concentrate the RF magnetic field in a precise and delimited area [55]. Thus, different solutions have been proposed to face the magnetic fluid diffusion issue [27], [56]. In particular, it is well recognized that the superposition of a static magnetic field to the RF field eliminates almost completely the response of the magnetic nanoparticles and, consequently, the heat release in the tissues [57]–[60]. Hence, the challenging problem of the RF field focusing is bypassed through the easier creation of a uniform DC magnetic field distribution with a small field free region (FFR); in this way, only the tissue portion in the FFR will respond to the hyperthermic treatment. Although able to achieve an efficient heating confinement, the lack of RF field focusing and the design complexity (due to the coexistence of DC and AC coils) represent the main limits of the technique.

To overcome such limitations, we propose an MPH radiating system able to focus the magnetic field in the required frequency range using a single coil and suitable for superficial treatments [6], [7]. The configuration herein presented significantly simplifies hardware requirements preserving, at the same time, a targeted and precise hyperthermic treatment. Moreover, the healthy tissue area exposed to the RF field is greatly reduced, leading towards safer clinical applications.

1.4.1 Nanoparticles sample

In order to perform the following experimental procedures, we first preparared suitable nanoparticles' samples. In this case, we employed uncoated magnetite (Fe_3O_4) nanoparticles, suspended in diethylene glycol and presenting an average hydrodynamic diameter of 24.9 ± 0.3 nm. The polydispersity index was determined by dynamic light scattering (DLS), resulting in a value of 0.089 ± 0.011.

In order to set the RF coil specification about resonant frequency, we realized a first aqueous sample using magnetite at 0.12 % and agar at 4% in volume fraction. In this way, the viscosity was high enough to simulate a biological tissue (real scenario). Following the procedure developed in section 1.3.2, we characterized the frequency behavior of the sample magnetic susceptibility and we found 340 kHz as the best working condition for heat release. This optimization step is necessary because nanoparticles' magnetic susceptibility is strongly dependent on the sample composition. As introduced in Section 1.3.2, along with the single nanoparticle size and coating, also the presence of agar strongly influences the susceptibility behavior [48]–[52]. Indeed, the viscosity increase is responsible for a limitation of the Brownian relaxation phenomenon. Thus, keeping in mind the final goal to use the RF coil in a real-scenario hyperthermic treatment, it turned out natural to choose the working frequency maximizing the heat release in a tissue-mimicking sample.

In addition, we realized also a second aqueous sample, using the same volume fraction of nanoparticles but without agar. As it will be described in the next section 1.4.4, the reason was to create a more fluid sample that we were able to deposit easily in different shapes (thin film, drops…), thanks to which visualizing the magnetic field focusing properties of our coil through the temperature distribution maps.

1.4.2 Numerical design of the coil

The design procedure was carried out through the CAD environment of a commercial electromagnetic software, based on the Method of Moments (Feko Suite, Altair, Troy, MI, USA). Along with the resonant frequency maximizing the heat release for a given sample (determined in the previous section), a field amplitude supporting an effective clinical application (in the order of 15-20 kA/m [61]) is required. In addition, in order to avoid additional instrumentation for the creation of a superimposed DC magnetic field, we desire an RF coil able to produce a superficial focal spot, suitable, for instance, for melanoma and breast cancer treatments. Therefore, we designed the coil with the aim of satisfying three main specifications: *a)* resonance frequency around 340 kHz; *b)* capability to produce high magnetic field amplitude (15-20 kA/m); *c)* presence of a sharp superficial spot. We proposed a

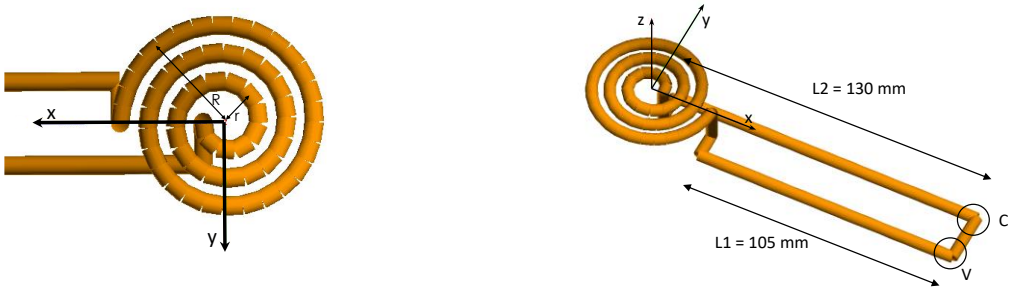

(a) (b)

Fig. 1.8 (a) Particular of the CAD model showing the proposed pancake geometry. (b) Complete CAD model of the coil for focused MPH treatments.

planar 3-turns spiral geometry (i.e. “pancake”) as focusing coil. This peculiar shape allows the concentration of the magnetic field in a spot coinciding with the region included in the inner turn of the helix [62], [63], making it suitable for treatments requiring a penetration depth of few centimeters. The inner radius *r* was chosen equal to 5 mm whereas the outer radius *R* equal to 25 mm (see Fig. 1.8(a)). The compact size of the coil contributes to maintain negligible the induced eddy currents, which are responsible of an undesired and unspecific heat deposition in the biological tissues [18], [62]. The hollow copper tube presented a diameter of 4.6 mm with a conductor thickness of 1 mm, necessary to allow the flux of a cooling liquid. The lengths of the two straight conductors (L_1 and L_2 in Fig. 1.8(b)) connected to the pancake coil were designed to provide enough operative space between the generator and the samples to perform experiments. Since the numerical estimation of the total inductance of the RF coil was 0.331 µH, the whole structure was made resonant at 340 kHz with a capacitive load C of 0.66 µF.

After the design process, we performed free space numerical simulations to verify the achievement of the desired specifications. The results shown in Fig. 1.9(a) demonstrate that the coil produces a good magnetic field focusing on the planes parallel to the coil plane ($z = 0$, see the CAD model in Fig. 1.8). For instance, 10 mm far from the coil plane ($z = 10$ mm), the magnetic field has a focal spot diameter of 10 mm with an amplitude about 15-20 kA/m. As pointed out before, the coil is suitable for superficial treatments, in the order of few centimeters.

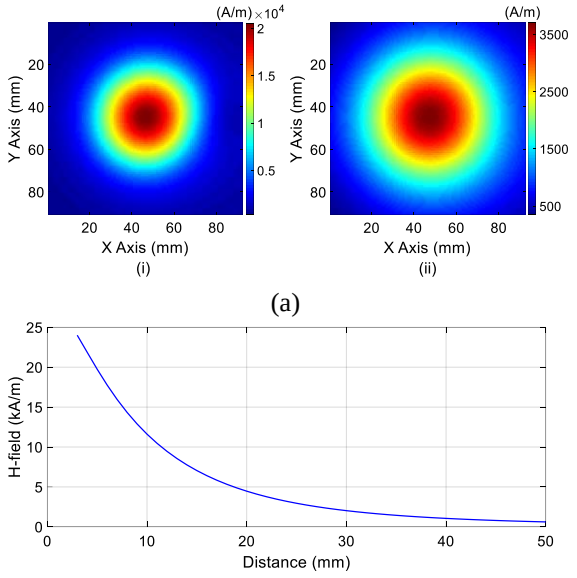

Fig. 1.9 (a) Magnetic field distribution in the plane distant 10 mm (z = 10 mm, (i)) and 30 mm (z = 30 mm, (ii)) from the pancake coil plane. It is evident from comparison how both the amplitude and the focusing of the magnetic field drop moving away from the coil plane. (b) Magnetic field amplitude along the coil axis (z axis).

Indeed, the amplitude of the magnetic field decreases very quickly moving away from the coil plane: the near field components of the electromagnetic radiation roughly drop according to the cube of the distance from the radiating source (Fig. 1.9(b)). In addition, the focusing performance of the coil degrades moving away from the coil plane (i.e. along z direction).

Finally, it is worth noticing that the coil has a strong inductive behavior, due to its peculiar geometry. Accordingly, the amplitude of the electric field in the near field region is more than five times lower with respect to the magnetic field, as demonstrated in Fig. 1.10. This aspect is an important requirement in terms of treatment safety, since the electric field can increase the Specific Absorption Rate (SAR) in a non-desired manner.

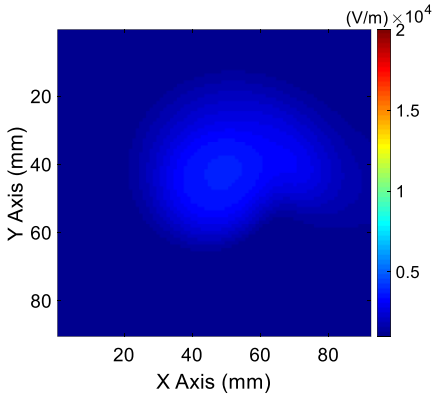

Fig. 1.10 Electric field distribution in the plane distant 10 mm from pancake coil plane. It can be noticed the significantly lower amplitude of the electrical field respect to the magnetic field, at the same distance from the coil plane.

1.4.3 Prototype of the coil

After the design and the numerical verification of its performances, we fabricated a prototype of the coil.

The handcrafted prototyping process considered the compatibility requirement for the coil with a specific high-power RF signal generator (NovaStar 5 kW, Ameritherm Inc., Scottsville, USA) (Fig. 1.11(a)). This generator allows choosing manually a discrete number of combinations for the internal inductive and capacitive loads, realizing a rough tuning of the connected coil. Then, an automatized function finds the best resonance condition for the particular coil, internally refining the tuning. Finally, the user can choose the desired power value (0-5 kW) delivered by the generator in order to match the specifications of a certain application. The leads L_1 and L_2 (Fig. 1.8 (b)) were equipped at their terminations with appropriate hydraulic connectors, mechanically matching the junction at the generator's power line (Fig. 1.11(b)). The hydraulic connectors allow the flux of the cooling liquid and create the electrical connection with the signal generator. As designed, the copper conductor is a hollow tube with an external diameter of 4.6 mm and copper thickness of 1 mm. In this way, the coil was able to sustain the water flow imposed by the generator cooling system (2.8 liters per minute at 2.72 atmospheres), guaranteeing safety requirement compliance.

(a) (b)

Fig. 1.11 (a) Front view of the control unit of the generator NovaStar 5 kW, Ameritherm Inc. (b) Fabricated coil prototype.

We performed workbench measurements of the coil in order to verify the inductance of the prototype before connecting it to the generator. In particular, we used a Vector Network Analyzer (E5071C ENA, Keysight, Santa Rosa, USA) to measure the impedance of the coil, including the hydraulic connectors. The measured inductance was 0.285 μH, in good agreement with the numerical estimation (i.e., a 13.9 % variation). We selected a capacitive load of 0.66 μF among the available values for the generator, as planned during the numerical design. Once the coil was connected, the generator showed a resonance frequency of 355 kHz (a 4.41 % deviation with respect to the numerical design), thus demonstrating the effectiveness of the entire design process. The small shift in the resonance frequency compared to our numerical design can be mainly addressed to the constructive imperfections of the coil (in particular, the step of the planar spiral was not perfectly constant), to the hydraulic connectors and to the unavoidable tolerances of capacitors and inductors inside the signal generator.

1.4.4 Experimental trials with magnetite nanoparticles

We performed different experimental MPH trials with the fabricated magnetite samples to demonstrate the focusing effectiveness of our radiating system and its hyperthermic efficacy in a real environment, even in absence of a targeted spatial distribution of nanoparticles.

The first experimental set-up consisted of a thin slice on a glass slide of the liquid magnetic sample (without agar), exposed to the RF magnetic field radiated by the coil.

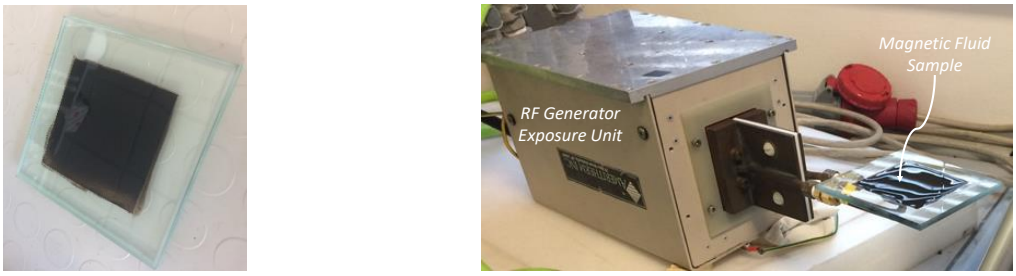

(a) (b)

Fig. 1.12 (a) Thin slice of magnetic nanoparticles fluid deposited on a 10 cm × 10 cm glass support through serigraph printing. (b) Exposure unit of the generator with the thin film of magnetic nanoparticles fluid placed over the coil.

The nanoparticles slice had a 6 cm × 6 cm square shape and it was layered by serigraph printing on a 10 cm × 10 cm glass slide (Fig. 1.12(a)), positioned centered over the pancake coil (Fig. 1.12(b)); the generator power output was set at 3 kW for a total exposure time of 240 seconds. The rise of the temperature was continuously monitored with an IR thermal camera (ThermaCAM™ E300, FLIR Systems Inc., Meer, Belgium). It may be worth noticing that the measured temperature map is a very effective way to visualize the magnetic field distribution. Indeed, the temperature time derivative depends proportionally to the power released by the magnetic fluid (Specific Absorption Rate, SAR [W/$g_{Fe_3O_4}$]), according to eq. (1.8). By solving the simple differential equation, we obtain the temperature time dynamic *T(t)*:

$$T(t) = \frac{m_{Fe_3O_4}}{CV} SAR(t - t_0) + T_0 \tag{1.15}$$

where T_0 e t_0 are the initial temperature and time, respectively. As also explained in eq. (1.7), SAR release is proportional, in turn, to the square of the applied RF magnetic field amplitude. Substituting eq. (1.7) in eq. (1.15), we can conclude that the temperature distribution at any instant directly follows the square of the magnetic field amplitude.

$$T(t) = \frac{m_{Fe_3O_4}}{CV} \frac{\mu_0 \pi \chi'' f H_0^2}{\phi \rho_{Fe_3O_4}} (t - t_0) + T_0 \tag{1.16}$$

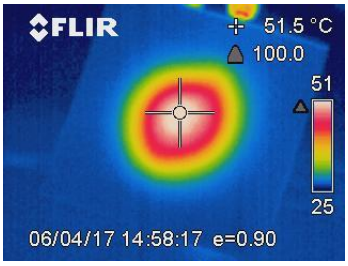

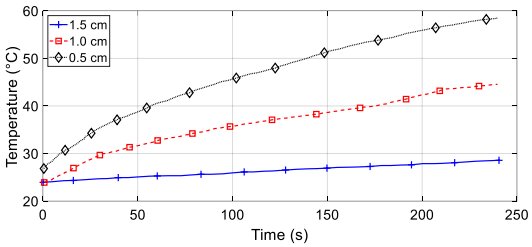

(a) (b)

Fig. 1.13 (a) Temperature map obtained 150 seconds after the exposure start of the magnetic nanoparticles thin film to the focused RF magnetic field. The small hot spot is evident at the center of the coil, thus demonstrating the focusing of the magnetic field. (b) We replicate 3 times the experiment: the temperature increase is greater when the distance of the sample from the coil plane is lower. Hence, the magnetic field amplitude diminishes when the sample is moving away from the coil plane, in good agreement with the numerical simulations.

Therefore, the magnetic field distribution produced by the coil can be qualitatively visualized from the temperature map, considering a certain uncertainty due to heat diffusion process.

We replicated this set-up changing the distance between the coil plane and the magnetic fluid thin-film sample. Specifically, the same sample was placed at 0.5, 1 and 1.5 cm from the coil plane. In this way, we wanted to experimentally verify the magnetic field amplitude drop moving away from the coil plane, as numerically predicted.

Comparing the result in Fig. 1.13(a), we can conclude that the measured temperature map – although approximated – shows an excellent agreement with the magnetic field distribution estimation obtained with the numerical simulation software. Moreover, as displayed in Fig. 1.13(b), the temperature reached by the sample decreases when it is placed at 0.5, 1 and 1.5 cm from the coil plane, respectively, confirming the validity of the design process and indicating that the proposed system is suited for superficial treatments.

The second experimental set-up consisted of exposing a Petri dish (diameter: 6 cm, height: 1.3 cm) to the RF magnetic field. We placed several drops of the liquid magnetic fluid on the top of the Petri dish. The drops – each with a volume of 10 µL – were deposited on two concentric circumferences with radii r_1 = 1 cm and r_2 = 2 cm, respectively (Fig. 1.14(a)). As in the previous case, we monitored the temperature distribution on the top of the Petri dish with the IR thermal camera during the RF exposure, pointed out the sharp spatial gradient of the heating process achievable with our system in addition to the first experiment (Fig. 1.14(b)).

(a) (b)

Fig. 1.14 (a) Magnetic nanoparticles drops on the top of a Petri dish (diameter 6 cm, height 1.3 cm). The two highlighted circumferences present a radius of 1 cm and 2 cm, respectively. (b) Experimental set-up (on the left) and temperature map of the surface of the petri dish after 40 seconds from the exposure start (on the right). Again, the targeted distribution of the magnetic field is well evident.

Along with the design specification of a well-focused magnetic field, the other important feature that the RF coil must satisfy is a sufficient level of the field amplitude, suitable to perform efficient hyperthermic treatments. Therefore, we used a third experimental set-up to verify the SAR level reached by our radiating system in an environment mimicking a real scenario. An Eppendorf vial with a volume of 2 mL was filled with the sample made of magnetite nanoparticles, water and agar. This solution mimics a biological tissue with high viscosity (e.g. bone), inside which the nanoparticles have a limited mobility (thus, they are less responsive to the external RF field because of the Brownian relaxation suppression). We placed the vial in the center, 0.8 cm over the pancake coil (Fig. 1.15(a)). We set the power of the signal generator to 1.2 kW, exposing the vial for 300 seconds; an optical fiber thermometer (CEAM Vr18CR-PC, Pozzale, Italy) was used to monitor continuously and accurately the temperature dynamic during the RF exposition. Fig. 1.15(b) shows the temperature dynamic obtained placing the optical thermometer at the center of the vial and at half of its height: we observed a total increment of the sample temperature of 9 °C. Finally, we obtained the SAR value by calculating the initial slope of the temperature curve, following (1.8). The calculated SAR value was quite large (20.15 $W/g_{Fe_3O_4}$), showing that the proposed RF coil and the adopted signal generator are able to heat both efficiently and precisely a desired target.

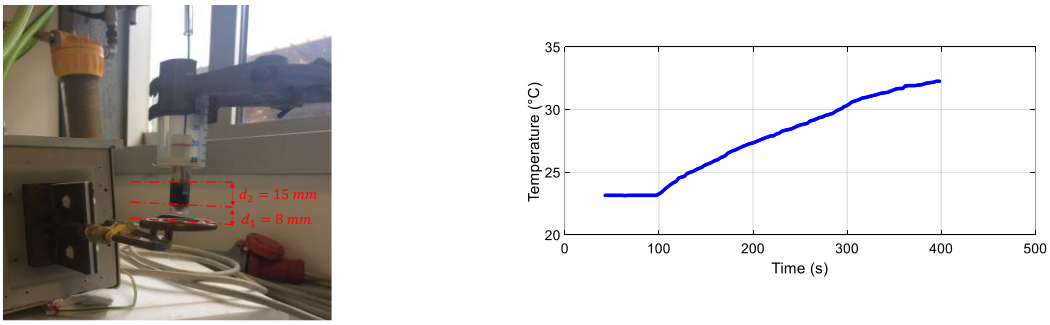

(a) (b)

Fig. 1.15 (a) Experimental set-up of the vial containing the high-viscosity magnetic fluid; the distance between the vial and the coil is 8 mm, while the fluid in the vial is 15 mm high. (b) Temperature of the vial measured through optical fiber thermometer during the exposition to the RF field.

1.4.5 Conclusions

In this work, we proposed a radiating system for highly focused hyperthermia with magnetic nanoparticles based on a novel RF coil. We started from the design of the coil, developed through a commercial electromagnetic simulation software implementing the Method of Moments. We performed numerical simulations of the coil in free space in order to verify the required specifications about the magnetic field distribution; in particular, the coil is able to focus a low frequency (340 kHz) field in a little superficial hot spot. After the designing process, we fabricated a prototype of the coil, satisfying the compatibility with our RF high-power signal generator. Finally, we conducted several experimental trials with a fluid containing magnetic nanoparticles of magnetite; we demonstrated the feasibility of performing highly focused and effective hyperthermic treatments with a very simple radiating instrumentation, also without a targeted distribution of the magnetic nanoparticles. The requirement of a focused treatment is a fundamental aspect in order to make possible a clinical implementation of MPH.

Our solution simplifies the technical proposals appeared in literature so far, which include both DC and RF coils; the proposed system comprehends only one RF coil, thus making hyperthermia instrumentation more affordable and flexible than the actual available

technology. Moreover, the reduced tissue area exposed to the RF electromagnetic field makes our approach safer with respect to undesired healthy regions damages.

In conclusion, our work can pave the way to a novel approach for hyperthermia with nanoparticles; effective, simple and safe treatments can be carried out with a single RF coil for several types of superficial tumors, such as melanoma, breast cancer and osteosarcoma. Further improvements can be directed in order to increase the penetration depth of the treatments, appropriately modifying the design of the coil.

2 CHAPTER 2: DESIGN OF DISTRIBUTED SPIRAL RESONATORS FOR THE DECOUPLING OF MRI RF COILS

2.1 Introduction

Today, Magnetic Resonance Imaging (MRI) is an established and diffused diagnostic methodology based on the nuclear magnetic resonance (NMR) of chemical elements [64]–[67]. It is capable of achieving millimetrical resolution for *in vivo* studies, along with an excellent contrast, especially for soft tissues. In addition, it is completely non-invasive and free from ionizing radiation, as opposed to computed tomography. The combination of these unique properties has made MRI a gold standard in medical imaging and research. In addition, it has become extremely popular and effective also in other applications, such as spectroscopy, where the well-known chemical shift phenomenon is exploited.

From a physical point of view, the image formation is made possible thanks to the interactions between a chemical nucleus and a proper excitation with external magnetic fields. Specifically, these interactions are due to an intrinsic property of the chemical element nucleus, i.e. the spin angular momentum s. Not all the chemical elements share this feature: having non-zero spin angular momentum is a quantum mechanical property retained by nuclei that have an odd number of protons and/or an odd number of neutrons. The spin s indicates the possible different energetic states for a nucleus (that are $2s+1$) and it is also responsible for the rotation of the nucleus around its axis; since the nucleus is also electrically charged, then a magnetic momentum μ arises, allowing the interaction with an external magnetic field.

In most of the medical cases, the interest is commonly directed to the signal coming from the proton nucleus; indeed, it presents a non-zero spin (equal to 1/2) and it represents the most abundant chemical species inside biological tissues, thus guaranteeing a quite strong signal and, consequently, excellent anatomical images. However, especially thanks to the adoption of high-field MRI scanners, other chemical elements, useful for diagnostic purposes but with a lower concentration with respect to hydrogen (such as sodium (s = 3/2), phosphorus (s = 1/2) and carbon 13 (s = 1/2)), have entered the clinical practice.

In the absence of an external magnetic field, the magnetic momentum μ of each nucleus possesses a random orientation. In this state, the net total magnetization (i.e., the summation of

all the magnetization vectors of each nucleus located in a volume) is zero. However, when an external static magnetic field B_0 is applied, individual magnetic moments tend to align with or against the external field. This interaction causes a precession of the nucleus magnetic momentum around the direction of B_0, at a frequency specific for a given chemical element, called the Larmor frequency ω_L:

$$\omega_L = \gamma B_0 \tag{2.1}$$

The parameter γ is called gyromagnetic ratio and it is unique for each chemical element (for the proton, it is equal to 42.58 MHz T^{-1}). Due to energetic considerations, there is a net excess of magnetic moments aligned with the B_0 field (parallel) with respect to the antiparallel direction. Thus, a non-zero total magnetization vector, resulting from all the magnetic moments of each nucleus precessing around B_0, emerges, in turn precessing around B_0 at the same frequency ω_L.

In order to generate a detectable signal from the total magnetization vector, it is necessary to perturbate the equilibrium state, achieved after the application of the external static B_0 field. In other words, the total magnetization vector has to be deflected from the direction parallel to B_0. Hence, a second magnetic field B_1, perpendicular to B_0, is employed as excitation pulse; the B_1 field is a radiofrequency (RF) magnetic field, oscillating at the desired Larmor frequency ω_L. As a result of the B_1 application, the magnetization vector is deflected from its equilibrium direction along B_0, proportionally to the RF pulse amplitude and time duration. The deflection angle is called flip angle (FA) α and it is measured at the end of the B_1 pulse:

$$\alpha = \int_0^T \gamma B_1(t)\, dt \tag{2.2}$$

where T is the total time duration of the RF pulse. Common flip angles in practical cases are 90° or 180° with respect to B_0 direction.

After the RF pulse, the magnetization vector, always precessing at ω_L, tends to recover again its equilibrium position aligned with B_0. During this phenomenon, the magnetization vector produces a detectable RF magnetic field, i.e. the Free Induction Decay (FID) signal, carrying the information about imaging. The properties of the FID signal strongly depend on

three main biological parameters, namely the proton density (PD), and the T_1 and T_2 relaxation times. These parameters are distinctive of a tissue and, moreover, differ in healthy and pathological tissues; thus, they can be used to perform diagnostic and anatomical images.

The FID initial amplitude (i.e., as soon as the RF B_1 pulse is ceased) is directly proportional to the proton density: the higher the proton density, the stronger the detected signal. For instance, tissues rich in water content, like liver or blood, have a higher proton density with respect to bone.

Instead, the two relaxation times are expression of the magnetization vector recovery from the deflected to the B_0-aligned position. In particular, if we consider a cartesian reference system and B_0 as directed along the *z* axis, in a generic instant after the RF excitation pulse, there will be a component of the magnetization vector along *z* axis and another one laying on the *xy* plane. For instance, immediately after a 90° flip angle, the entire magnetization vector will be in the *xy* plane and then, it will recover the position along the *z* axis within a certain time interval.

Thus, we call the characteristic time required for the magnetization vector to lose its *xy* plane component as *spin-spin* relaxation time (indicated with T_2):

$$M_{xy}(t) = M_{0xy} e^{-t/T_2} \tag{2.3}$$

It may be interesting noticing that the presence of magnetic field dishomogeneities causes a faster T_2 relaxation time; locally distributed paramagnetic materials can induce such dishomogeneities and, consequently, they can be used as contrast agents (as briefly discussed in chapter 1 about iron oxide nanoparticles).

On the other hand, the *spin-lattice* relaxation time (T_1) describes the gradual re-alignment of the magnetization vector along B_0 direction; since there cannot be any *xy* component when the magnetization vector has fully recovered its original direction along B_0, it follows that $T_1 \geq T_2$.

$$M_z(t) = M_0 \left(1 - e^{-t/T_1}\right) \tag{2.4}$$

The two relaxation phenomena can be incorporated in the famous Bloch's equations which describe the temporal variation of the magnetization vector.

$$\begin{cases} \frac{dM_x(t)}{dt} = \gamma\left(M_y(t)B_z(t) - M_z(t)B_y(t)\right) - \frac{M_x(t)}{T_2} \\ \frac{dM_y(t)}{dt} = \gamma\left(M_z(t)B_x(t) - M_x(t)B_z(t)\right) - \frac{M_y(t)}{T_2} \\ \frac{dM_z(t)}{dt} = \gamma\left(M_x(t)B_y(t) - M_y(t)B_x(t)\right) - \frac{M_z(t)-M_0}{T_1} \end{cases} \quad (2.5)$$

Since proton density, T_1 and T_2 are functions of tissues properties, several different RF pulses sequences have been developed to weight one parameter at the expense of the others (for instance, inversion recovery, spin-echo, gradient-echo), thus to obtain images stressing the desired features of a particular clinical exam.

Besides the physical principles at the basis of MRI, a lot of industrial research is also directed to improve and perfectionate the hardware components of scanners. Since in this chapter the focus is in the components responsible for FID signal excitation and reception, we can concentrate in particular on the magnet, the gradient coils and the RF coils.

The magnet is responsible for the generation of the static B_0 field; different magnet typologies have been developed since the MRI first appearance.

A permanent magnet is made of ferromagnetic materials; with respect to other typologies, the maintenance is low cost but it is very heavy and suitable only for the generation of quite low static field (up to 0.3 T). For these reasons, it finds applications in MRI open scanners, useful for imaging of limited portions of human body.

Instead, the resistive magnet is an electrocalamite, meaning that the B_0 field is induced by high-amplitude currents flowing in opportune coils. The main limits of this solution are the requirement of an efficient cooling system due to the high currents flowing in the structure and the operative costs (especially, energy consumption), which are greater than the ferromagnetic magnet.

However, a giant technological step was made with the introduction of superconductive magnets, nowadays the most diffused technology. Exploiting the superconductive effect, huge currents can flow in particular materials when the temperature is maintained close to the absolute zero (few Kelvin degrees). This allows the production of ultra-high and homogeneous static fields, thanks to which the MRI technique has reached a submillimetrical spatial resolution. However, the costs are sensibly higher in comparison with the previous examples,

especially for the extremely delicate management of the cooling liquid (elium or nitrogen) that must be kept close to the absolute zero temperature.

Since the MRI goal is the realization of an image, it is required to discriminate the signal coming from a specific region in the tissue (i.e., from each voxel), introducing a form of codification. The adopted stratagem consists in superimposing small amplitude static fields, which exhibit linear field gradients in the three spatial directions, to the homogenous B_0: the idea is to create in a given point of the space a unique resulting static field, i.e. a unique precession frequency according to eq. (2.1). Reading the response of this point, we are able to distinguish the location where the signal is coming from. Gradient coil technology has evolved considerably since the introduction of first-generation systems. Early systems had maximum gradient strengths of about 10 mT/m and rather slow switching times. Current generation systems can have maximum gradient strengths of 100 mT/m and much faster switching times (up to 150 mT/m/ms). These values allow the system to achieve a 0.7 mm slice thickness.

Finally, RF coils are needed to excite and deflect the magnetization vector (i.e., to create the B_1 field) and to capture the consequent FID signal. RF coils can be designed only to generate excitation pulses or to receive the signal, but, more and more frequently, complete transceiver systems are fabricated employing the same coils. According to the tissue portion to be studied, several designs have been presented: volume coils for large portions, surface coils for local imaging and array of coils for simultaneous acquisition (thus, increasing SNR, Field of View and reducing scan time).

Especially when arrangements of multiple coils are employed, problems arise because of the undesired mutual coupling, which is detrimental for the image quality. In particular, the purpose of the present chapter is to face this issue, with a specific attention towards 7 T MRI scanners: innovative technological solutions to decouple closely placed RF coils, exploiting additional miniaturized spiral resonators, will be discussed in the next paragraphs.

2.2 Mutual coupling issue in multiple coils arrangements

In Magnetic Resonance Imaging (MRI) the mutual decoupling between two or more RF coils is one of the most challenging design tasks, both for single frequency arrays and for

multiple tuned RF coils. These MRI RF coils configurations can be used to expand the acquired Field of View (FOV), to increase the Signal-to-Noise ratio (SNR), to reduce the total scan time, and also to allow the acquisition of information deriving from different nuclei (e.g. Double-Tuned configurations) [68]–[76]. In general, inside the MRI bore, the available space suitable for the RF coils can be very limited, and a high filling factor of the RF coils with the biological sample is strongly desirable; thus, the RF coil elements need to be placed very close to each other, resulting in a high mutual coupling that significantly detunes the resonant frequency [77]. This problem leads to SNR degradation and a lowered efficiency of the RF transmitting side. At the Larmor frequencies of 7 T MRI systems, the main contribution to mutual coupling can be still associated to the magnetic flux linkage between the RF coils, rather than to mutual capacitive coupling (significant for fields above 7 T [78]).

The problem of the mutual coupling in MRI applications has been extensively studied in the literature. The most common decoupling system for RF coils arrays is the surface overlapping technique [68]. Although this method is straightforward, it is not scalable when the number of RF coils increases, requiring additional means for decoupling. Moreover, it is not feasible for coplanar and concentric RF coils configurations, which are typically used for Double-Tuned (DT) surface RF coils.

In the case of DT RF coils, another well-established practice is the use of a lumped trap circuit inserted in the lower frequency RF coil loop [79]. This method can achieve good decoupling performances, but the Q-factor of the lower frequency RF coil worsens due to additional losses inside the lumped elements of the trap circuit [80], [81]. In addition, peaks of electric field next to the lumped elements (especially capacitors) can be produced, requiring the insertion of additional shielding mechanisms to avoid undesired hot spots in the sample tissues [82], [83]. Another interesting decoupling solution consists in an appropriate geometrical disposition of the DT coils [84] to minimize coupling, which is a very effective method when no particular constraints on the coils positioning are present.

A relatively recent decoupling method (Induced Current Elimination, ICE), based on an eigenvectors and eigenvalues approach, has been presented in [85], [86]. Thanks to this method, additional resonant elements (i.e. microstrip elements) interleaved between the RF coil loops can be placed, and the conditions necessary for decoupling analyzed. In particular,

the currents induced in these decoupling elements can reduce the flux linkage between the MRI coils. Other works presented in the literature for decoupling purposes exploit additional reactive and resonant elements, variously interleaved between the MRI array RF coils [87]–[92]. Also, the use of magnetic walls [93]–[95] successfully demonstrated a reduction of mutual coupling between adjacent RF coils tuned at the same frequency (^{1}H). The basic operative principle is similar to the ICE technique, but here a high number of miniaturized resonators are employed instead of a single one.

This work aims to present a general and systematic procedure useful to design distributed spiral resonators (SRs) used for the decoupling of RF coils finding MRI applications at 7 T [8]–[12]. Our design adopts small planar SRs, placed in between RF coil loops, capable to produce a large RF decoupling. We are able to determine the minimum number of SRs to be employed, minimizing unnecessary resistive losses and thus, simplifying and improving previous similar literature solutions. Since there are no physical connections between the decoupling SRs and the RF coil elements, we obtain a mechanically robust experimental set-up, facilitating the transceiver design. In particular, we present numerical studies and experimental verification of the developed analytical design procedure through fabricated prototypes of a coplanar and concentric DT configuration (^{1}H/^{23}Na), chosen as test case.

2.3 A Novel Extraction Method of Equivalent Circuit Parameters of Spiral Resonators

Since the decoupling scheme developed in this chapter is based on the use of spiral resonators as unit-cells for RF MRI filters, the first required step consists in an accurate characterization of the electromagnetic properties of such inclusions.

Spiral Resonators have been longly considered as one of the most popular unit-cell for metamaterials design. Metamaterials are nowadays a consolidated branch of electromagnetic research and they are aimed at providing a novel class of artificial engineered materials able to show anomalous properties, not present in natural materials. Metamaterials can provide negative values of complex dielectric permittivity and magnetic permeability [96]–[99]. These

properties are achieved over a narrow frequency bands and they are due to the resonant behavior of miniaturized resonators [100], [101]. Because of the small footprint of the elementary resonators compared to the wavelength, various homogenization approaches [102]–[105] have been proposed to interpret these particles or array of particles as bulk material with negative permittivity or permeability values. Various resonators shapes have been proposed in the literature to extremely stress the miniaturization of the particle with respect to the operating wavelength [106]–[108]. Among this broad class of materials, Spiral Resonators (SRs) have demonstrated their ability to provide a high level of miniaturization and they have been extensively used as metamaterial unit cells or as decoupling distributed filter in array applications [94], [95], [109]. Moreover, SRs have been recently employed also in the fast-growing field of the energy harvesting, because of their property to act as an inductive tank circuit able to store energy coming from the environmental electromagnetic pollution [110]–[112].

The key aspect in the design of a spiral resonator is to derive an accurate equivalent circuital representation of the miniaturized inclusion thus avoiding long and time-consuming electromagnetic simulations. A number of works in literature reports helpful analytical model of passive spiral resonators (SRs) [100], [113]–[115]. The SR is usually modelled as an RLC series resonator and the values of the L and C parameters are derived starting from classical electrostatic considerations [100]. Such models revealed themselves able to provide a correct estimation of the resonance frequency compared to simulations [100] and measurements [115]. The experimental verification of the resonance frequency is usually carried out by employing two monopoles closely located to the resonator [115]. However, a rigorous verification of the values of the estimated L and C parameters used to characterize the resonator is not available. In particular, a different behavior of the values of capacitance and inductance as a function of the number of spiral turns have been observed by using different models [100], [113], [116] even with a similar estimation of the resonance frequency. As it is well known, there exist infinite couples of L and C that provide a certain resonance frequency for an LC circuit; in this sense, a complete characterization is achieved only if the derived L and C values are verified against an accurate estimation obtained, for instance, from a full-wave simulation [117], [118]. The measurement of the resonators with one or two external

antennas permits only the estimation of the resonance frequency since the coupling between the interrogating antenna and the passive resonator is unknown.

As a consequence, a reliable procedure, based on full-wave simulations or measured data, which guarantees the accurate extraction of the RLC parameters without any ambiguity is certainly missing in the literature. Not only the resonance frequency has to be predicted by the RLC parameters, but also the behavior of the resonator around the resonance frequency.

In the proposed work, the R, L and C parameters of the circuit model are obtained by including the RLC series circuit within an accurate lumped model of the entire simulation set-up. Once that the simulation setup is accurately characterized (including the mutual coupling between the interrogating antenna and the spiral resonators), the RLC parameters remain the sole unknows and they can be precisely and unambiguously derived by using a fitting procedure. In this way, the actual RLC values as a function of the number of turns can also be obtained and interesting considerations about the electromagnetic behavior of the spiral resonators can be performed, including a proper estimation of the Q-factor. Our approach is completely general, and it allows analyzing any shape of resonators, unlike the fully-analytical works developed in the literature, in most cases suitable only for particular spiral resonators.

2.3.1 Procedure for the Estimation of RLC Parameters of the Spiral Resonator

As already discussed, the goal is to develop a novel reliable extraction procedure for the RLC parameters of a resonant magnetic inclusion as a spiral resonator.

The estimation of the R, L, C parameters of the spiral resonator is performed by using the simulation set-up depicted in Fig. 2.1(a). It consists of the probe loop and the spiral resonator (SR) under test. The probe loop is non-resonating and fed by coaxial cable. The SR is placed at the center of the probe loop. The simulation setup shown in Fig. 2.1(a) is schematized by the equivalent circuit proposed in Fig. 2.1(c) [65], [119].

The external probe loop is represented by the R_{loop} and L_{loop} due to its inductive nature. The SR is represented by the RLC series circuit on the right-hand part. The coupling coefficient M_{loopSR} takes into account the mutual coupling between the two circuits.

A block diagram of the proposed procedure is reported in Fig. 2.2.

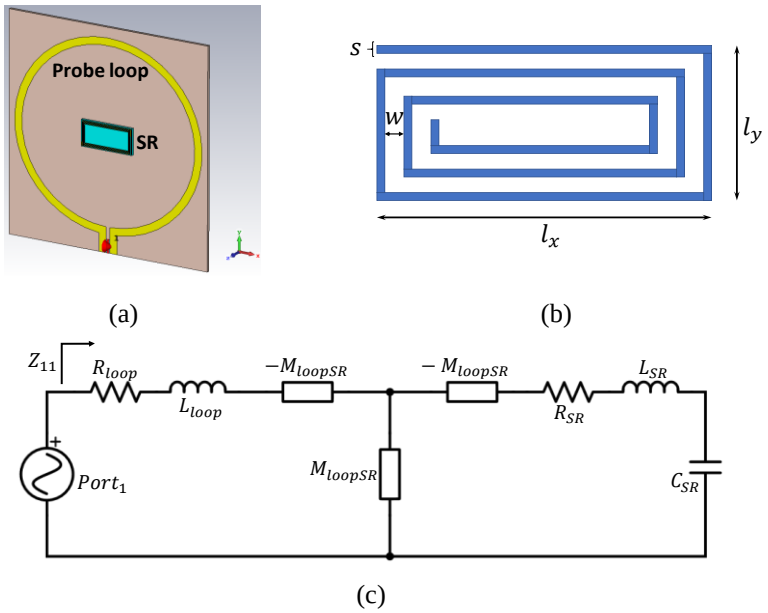

Fig. 2.1. (a) CAD model of the adopted simulation set-up (CST Studio Suite, Darmstadt). (b) Representation of a generic spiral resonator (drawing is not in scale). (c) Equivalent lumped circuit for inductively coupled spiral resonator and probe loop.

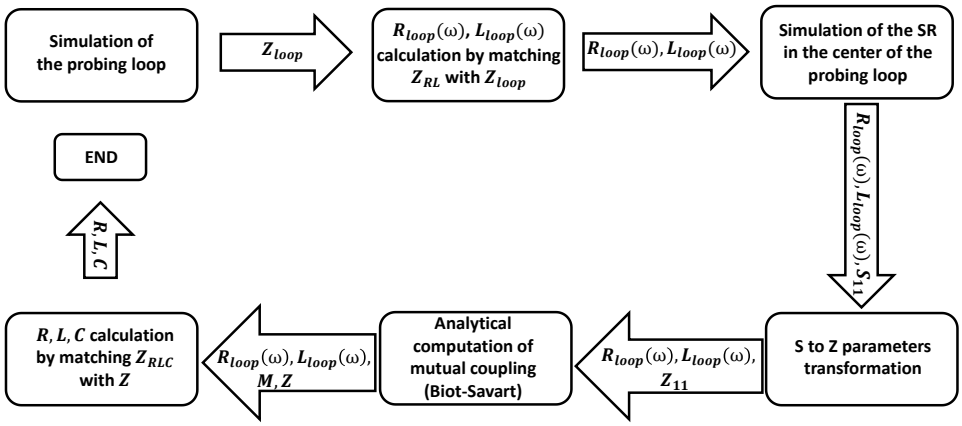

Fig. 2.2. Block diagram of the proposed retrieving method.

The characterization process of the loop resonator starts with a full-wave simulation (or measurement) of the S_{11} of the probe loop standalone. The simulations, in our case, has been performed through CST Studio Suite (CST Computer Simulation Technology AG, Darmstadt, Germany). Once calculated the S_{11} of the probe, the input impedance, Z_{11}, is straightforwardly computed. At this point the parameters R_{loop}, L_{loop} as a function of frequency are derived. This step is required in order to completely characterize the simulation set-up, leaving the SR's

RLC parameters as the unique unknowns. The SR under test is therefore placed centered with respect to the probe loop and the mutual impedance M_{loopSR} value must be determined.

The mutual impedance value M_{loopSR} quantifies the amplitude of the inductive coupling between the two elements. This parameter can be estimated through a magneto-static approach [120], once the geometrical parameters of the set-up are known. Indeed, under quasi-static hypothesis, it is possible to apply Biot-Savart formulation to estimate the mutual coupling between two generic coils. This assumption is substantiated by the small dimension of the set-up with respect to the wavelength and its geometrical properties. The typical dimension of the considered spiral resonators is around 1 cm whereas the wavelength at 300 MHz (in the middle of the chosen frequency span) is equal to 1 m in the vacuum. Considering a quasi-static assumption valid until the resonator is smaller than one tenth of the applied wavelength, we can set an upper bound for our hypothesis at around 3 GHz.

Thus, the magnetic field produced by a generic current path at a generic point can be expressed as:

$$\vec{B}(\vec{r}) = \frac{\mu_0}{4\pi} \int \frac{I\vec{dl} \times \vec{r'}}{\left|\vec{r'}\right|^3} \tag{2.6}$$

where μ_0 (H/m) is the magnetic permeability of the vacuum, I (A) is the current amplitude flowing in the path, $\vec{dl}$ (m) is an infinitesimal element of the current path and $\vec{r'}$ (m) is the distance between a generic point of the space and the infinitesimal element $\vec{dl}$.

The mutual coupling coefficient between a generic coil j and a coil i is defined as the magnetic flux (Φ_{ij}) through the coil j induced by the current flowing in the coil i:

$$M_{ij} = \frac{\Phi_{ij}}{I_i} \tag{2.7}$$

Afterwards, supposing a unit current in the coil i (I_i), the mutual coefficient M_{ij} is simply the flux of the magnetic field analytically calculated from eq. (2.6) through the surface of the coil j.

In this way, given the geometrical properties of the two elements constituting the system, we can numerically set a unit current flowing in one of the two coils and evaluate the

inductive mutual coupling on the remaining one. Obviously, it is also valid that $M_{ij} = M_{ji}$. Thus, a value of the mutual coefficient expressed in nH can be obtained.

At this point, the only unknown parameters in the model of Fig. 2.1(c) are the RLC parameters of the spiral resonator. In order to find the most suitable values of the RLC circuit, we implemented in a computer code the lumped circuit of Fig. 2.1(c); therefore, it was possible to evaluate the Z_{11} parameter according to the lumped elements values:

$$Z_{11}(\omega) = \left[\left(R_{SR} + j\omega L_{SR} + 1/j\omega C_{SR} - j\omega M_{loopSR}\right) \| \, j\omega M_{loopSR}\right] + \\ + R_{loop} + j\omega L_{loop} - j\omega M_{loopSR} \tag{2.8}$$

Since R_{loop}, L_{loop} and M_{loopSR} parameters are known, eq. (2.8) is a function of the SR's lumped electric parameters only.

At this point, we compare the Z_{11} obtained from full-wave simulations (i.e. $Z_{11_{CST}}$ in eq. (2.9)) with the Z_{11} expressed in eq. (2.8) (i.e. $Z_{11_{Fitting}}$). Among all the infinite combinations of RLC parameters for the spiral resonator producing a resonance at the frequency estimated by the full-wave software, there will be one that better fits the simulated Z_{11}; in particular, a mean root square cost function has been chosen:

$$\min\{err\} = \min\left\{\sqrt{\sum\nolimits_{\omega}\left\{\left[\mathrm{Im}(Z_{11_{CST}}) - \mathrm{Im}(Z_{11_{Fitting}})\right]^2 + \left[\mathrm{Re}(Z_{11_{CST}}) - \mathrm{Re}(Z_{11_{Fitting}})\right]^2\right\}}\right\} \tag{2.9}$$

As previously stated, the resonant frequency f_{res} of the spiral resonator can be easily detected from the full wave simulation. As the resonant properties of the spiral resonator are only dependent on its L and C values, we choose the best fitting LC couple satisfying the following relation:

$$f_{res} = \frac{1}{2\pi\sqrt{LC}} \tag{2.10}$$

On the other hand, the resistance term R influences the Q-factor of the spiral resonator and it is spanned in the fitting procedure independently from the L and C values.

In order to obtain physically meaningful initial seeds for the fitting procedure, we apply the method presented in [121]. By exploiting the model described in eq. (2.8), we carried out a de-embedding procedure on the simulated $Z_{11_{CST}}$ in order to get the RLC parameters of the spiral. From eq. (2.8), the de-embedded parameters can be calculated as:

$$(R_{SR} + j\omega L_{SR} + 1/j\omega C_{SR}) = \frac{-(j\omega M_{loopSR})^2}{Z_{11}(\omega) - Z_{loop}} \tag{2.11}$$

The real part of this function evaluated at the resonant frequency gives the initial seed for the resistance:

$$R_{SR_{seed}} = \Re\left\{\frac{-(j\omega_{res} M_{loopSR})^2}{Z_{11}(\omega_{res}) - Z_{loop}(\omega_{res})}\right\} \tag{2.12}$$

On the other hand, the half of the derivative of the imaginary component of eq. (2.11) (i.e., *LC* series), always evaluated at the resonant frequency, gives the initial seed for *L*.

$$\begin{aligned} L_{SR_{seed}} &= \frac{1}{2}\frac{\partial}{\partial\omega}\left\{\Im\{R_{SR} + j\omega L_{SR} + 1/j\omega C_{SR}\}\right\}\Big|_{\omega=\omega_{res}} = \\ &= \frac{1}{2}\frac{\partial}{\partial\omega}\left\{\Im\left\{\frac{-(j\omega M_{loopSR})^2}{Z_{11}(\omega) - Z_{loop}(\omega)}\right\}\right\}\Bigg|_{\omega=\omega_{res}} \end{aligned} \tag{2.13}$$

The initial seed for C simply follows from eq. (2.10).

In this way, we can obtain the combination of *RLC* parameters that better fits the full-wave simulation, thus providing an unambiguous characterization of the SR under test.

2.3.2 Numerical Results

We performed a series of tests of the proposed fitting procedure in order to characterize the behavior of different spiral resonators (SRs) as a function of the number of turns. In particular, we selected the meaningful cases summarized in Table 2.1. They consisted in two different shapes for spiral resonators (square and rectangular, respectively) and we computed the *R*, *L* and *C* with respect to the number of turns *N*.

The probe loop was non-resonant, and it was not loaded with any reactive loads. The loop was made of copper and it was etched on a 0.8 mm thick FR4 substrate (ε_r = 4.3, $tan\delta$ = 0.025). As a first step, we characterized the probe loop standalone in order to obtain its proper

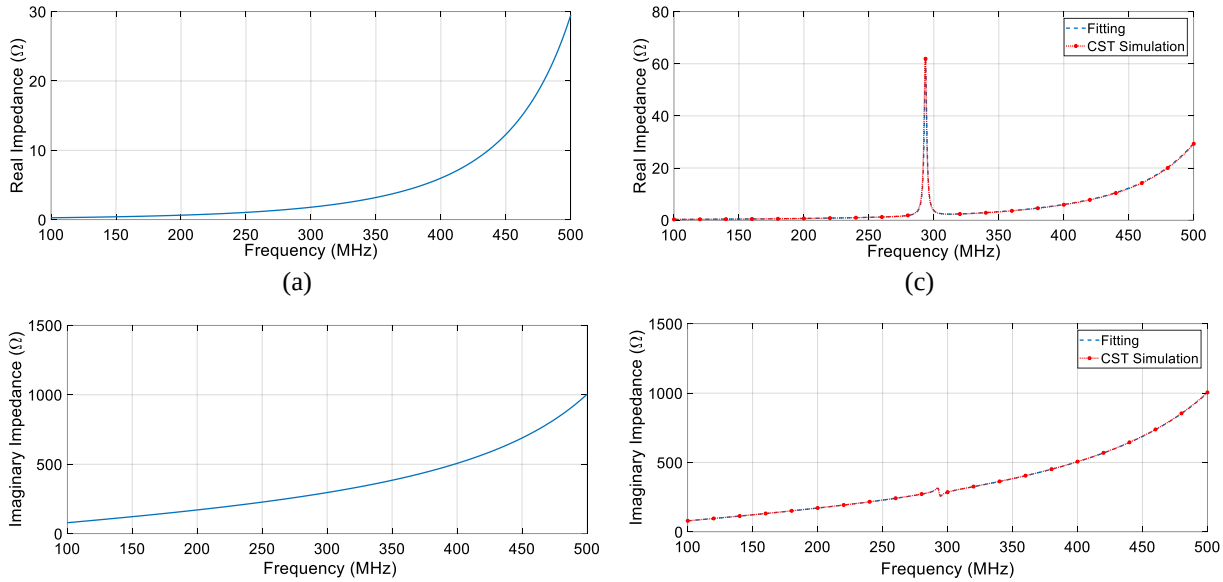

Fig. 2.3. Impedance of the loop (i.e. the larger magnetic probe) without the spiral resonator: (a) Real part, (b) Imaginary part. Impedance of the probing loop coupled with one of the spiral resonators (N=6, l_x=13.7 mm, l_y=6.7 mm) with the fitting obtained by using the lumped equivalent circuit in Fig. 2.1(c): (c) Real part, (d) Imaginary part. It can be noted that the resonant frequency of the spiral resonator is easily detectable from the full-wave simulation.

Table 2.1
Analized Spiral Resonators with the Fitting Procedure

Shape	*N*	$w = s$ (mm)	l_x (mm)	l_y (mm)
Rectangular	[3, 4, 5, 6, 7, 8, 9, 10, 11, 12, 13]	0.127	13.7	6.7
Square	[3, 5, 7, 9, 11, 13]	0.127	6.7	6.7

self-impedance (Fig. 2.1(a)). For the case of the larger rectangular spiral resonator, it consisted in a loop of 5 cm diameter, with a strip width of 2 mm. The frequency span was set between 50 and 500 MHz. On the other hand, we selected a smaller probe loop for the square resonator (2 cm diameter), in order to enhance the mutual coupling between the probe and the spiral (whose area is smaller with respect to the rectangular one), spanning the spectrum between 250 MHz and 1 GHz. The behavior of this probe loop was similar to the case of the larger probe but shifted in frequency. In order to clarify the effect of the spiral resonator placed in the middle of the probe loop, we reported in Fig. 2.3 both the impedance of the unloaded

probe (real and imaginary part) and its impedance loaded with a spiral resonator with the following parameters: N=6, l_x=13.7 mm, l_y=6.7 mm. A similar behavior is observed for other resonators with different dimensions. As expected, the real component of the impedance of the probe loop increases with the frequency, due to the more pronounced skin effect (Fig. 2.3(a)). In the same way, we can see that the imaginary component is totally inductive (Fig. 2.3(b)), as predictable, because we added no additional reactive load to the probe. Thus, we concluded that the probe loop is effectively representable as a R_{loop}, L_{loop} equivalent circuit.

In general, a spiral resonator can be defined as a N-turns planar spiral, presenting different shapes, strip width (s) and gap between strips (w) (Fig. 2.1(b)). For simplicity, we selected these two parameters as equal in our tests. The spiral resonators were made of copper and etched on a 0.8 mm thick Arlon substrate (ε_r = 3.58, $tan\delta$ = 0.0035). This substrate is small compared to the probe substrate, and it was placed, centered, on the top of the probe loop.

In Fig. 2.3 (c) and (d) we reported the real and imaginary components of the impedance of the probe loop inductively coupled with the rectangular spiral resonator (N=6 turns, lateral dimensions of l_x=13.7 mm and l_y=6.7 mm). As it is apparent, both the real and the imaginary components of the Z_{11} were well fitted by the proposed procedure, with an almost perfect overlap between the simulated and the fitted curves. This confirmed the validity of the employed circuit model for the probe-spiral resonator system.

As described in Section 2.3.1, once the geometrical properties of the system are known (probe loop and the particular spiral resonator under test), it is possible to apply Biot-Savart approximation in order to evaluate the mutual coupling. It must be noted, as shown in Fig. 2.4(a), that the estimated mutual coupling coefficients correctly increase with the number of turns of the spirals. Indeed, each turn added to the spiral resonator increases the area available for the linkage of the magnetic field produced by the fed probe loop.

At this point, the only undetermined unknowns remained the RLC parameters of the specific SR under test. By using a specifically designed Matlab algorithm, the RLC parameters were derived, according to eqs. (2.8) and (2.9), for each spiral configuration reported in Table 2.1. We exploited the initial RLC seeds derived according eqs. (2.12) and (2.13).

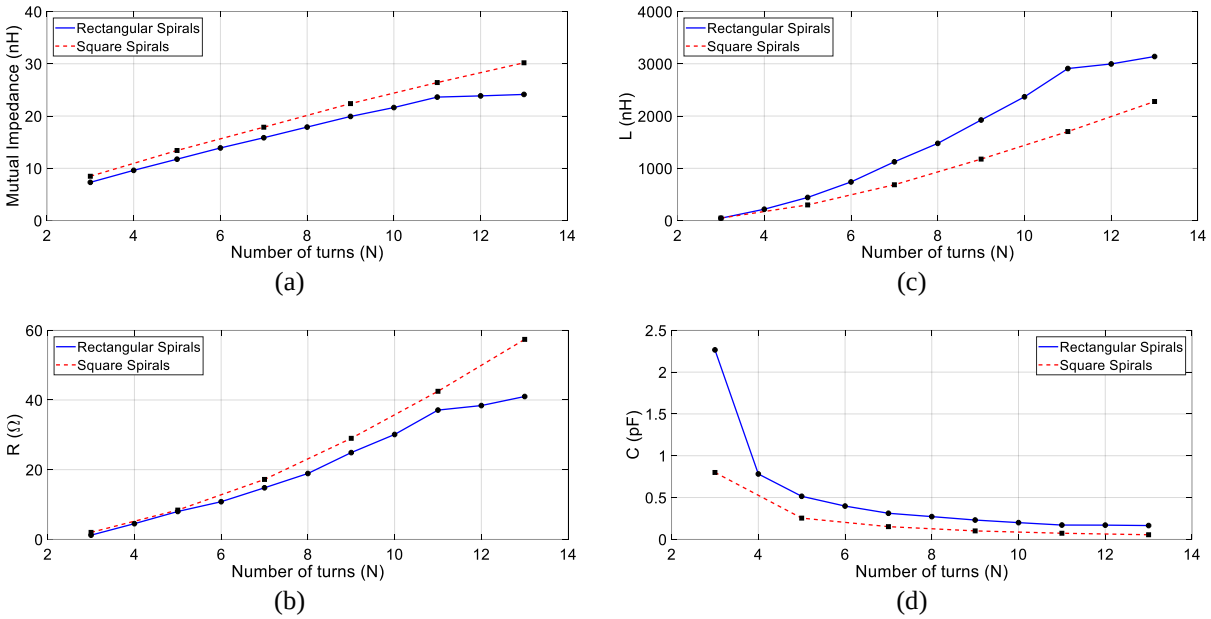

Fig. 2.4. (a) Mutual impedance between the considered rectangular spiral resonators and the larger probe loop (solid line); Mutual impedance between the considered square spiral resonators and the smaller probe loop (dashed line). (b)-(d) Impedance of the spiral resonators (rectangular and square) obtained from the fitting when the number of turns increases: (b) Resistance, (c) Inductance, (d) Capacitance.

As already stated, it is interesting at this point to evaluate the behavior of the *R*, *L* and *C* of the spiral resonator as a function of the number of turns when the external dimensions of the spiral are fixed. Fig. 2.4(b)-(d) shows the behavior of the RLC parameters for the previously fitted spirals (rectangular and square) when the number of turns spanned as described in Table 2.1.

Once computed the actual *RLC* parameters, it is also possible to derive the Q-factor of the spiral resonator, which is important for correctly describing the selectivity of the resonance. Q-factor can be typically described as [122]:

$$Q = \frac{\omega_{res} L}{R} = \frac{1}{R}\sqrt{\frac{L}{C}} \tag{2.14}$$

where ω_{res} is the resonant frequency whereas *R*, *L*, *C* are the extracted electrical lumped parameters of the considered spiral resonator. As shown in Fig. 2.5, the Q-factor for the rectangular SR increases as a function of the number of turns up to a particular value, when it starts to diminish. The same analysis was performed also for the square spiral resonator.

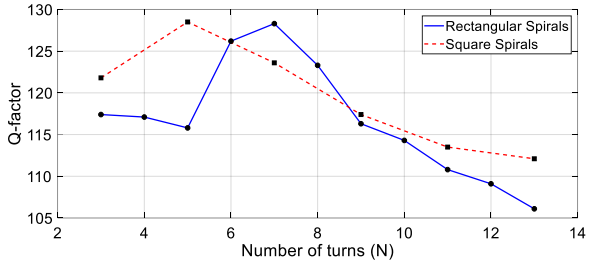

Fig. 2.5. Q-factor behavior of the spiral resonators (rectangular and square) with the increasing number of turns.

The results of the estimated lumped *RLC* parameters and the Q-factor are finally summarized in Table 2.2 and Table 2.3, along with the comparison with the initial seeds estimated from the de-embedded simulated impedance of each spiral resonators.

Table 2.2
Analyzed Rectangular Spiral Resonators With Our Fitting Procedure

N	*R* (Ω)	*L* (nH)	*C* (pF)	*Q-factor*	*R seed* (Ω)	*L seed* (nH)
3	1.2	45	2.266	117.4	1.2	45
4	4.5	217	0.782	117.1	4.5	217
5	8.0	442	0.515	115.8	7.9	443
6	10.8	739	0.398	126.2	10.6	744
7	14.8	1124	0.312	128.3	14.8	1129
8	18.9	1477	0.272	123.3	18.8	1491
9	24.9	1924	0.231	116.3	24.2	1928
10	30.1	2368	0.200	114.3	29.9	2392
11	37.1	2909	0.171	110.8	36.9	2929
12	38.4	2997	0.170	109.1	38.3	2994
13	41.0	3139	0.165	106.1	40.8	3132

Table 2.3
Analyzed Squared Spiral Resonators With Our Fitting Procedure

N	*R* (Ω)	*L* (nH)	*C* (pF)	*Q-factor*	*R seed* (Ω)	*L seed* (nH)
3	2.0	47	0.800	121.8	1.9	48
5	8.4	299	0.254	128.5	8.3	310
7	17.2	685	0.152	123.6	16.9	689
9	29.0	1176	0.101	117.4	28.6	1187
11	42.5	1703	0.073	113.5	42.3	1705
13	57.4	2278	0.055	112.1	56.9	2267

2.3.3 Physical Considerations on Extracted Parameters

The results described in Section 2.3.2 are well suited for a physical interpretation.

First of all, it can be seen from Fig. 2.4 that the resistance term increases almost linearly with the increase of the turns. This effect is expected because each turn added to the spiral resonator raises the total copper length and, thus, the losses in the spiral. In the same way, the inductance presents an approximately quadratic behavior with the number of turns which is meaningful for spiral-shaped object [123]–[126].

More importantly, the behavior of the inductance (as well as the resistance) of the spiral resonators show a saturation with the increase of the number of turns; this can be easily explained by the increasing filling factor of the spiral area (i.e. each added turn becomes smaller than the previous) that is more evident for the rectangular spiral rather than for the square shape. This result is opposite to that presented by [100], [115]; the fully analytical model therein developed presents an inductance that decreases with the increase of the number of turns. However, our fitting procedure demonstrated an opposite behavior, which is in accordance with the classical physical background of the phenomenon.

Moreover, the behavior of the retrieved capacitance is clearly decreasing with the number of turns. Such behavior is compatible with a distributed capacitance obtained by the summation of capacitors in series. Again, our result is opposite to what developed in the literature through only analytical formulation [100], [115].

Finally, Fig. 2.5 describes the Q-factor of the considered spiral resonator with the increase of the number of turns. As it can be observed, there is a specific value of the number of turns, which brings to the maximum of the Q-factor. This is due to the simultaneous behavior of the resistance and the inductance of the spiral resonator (see eq. (2.14)). When the number of turns is raising beyond a certain value, the total losses introduced in the spiral become predominant over the inductance increase. Such information is very important from a design point of view [127], [128], especially when the selectivity of the SR's resonance is a fundamental feature to obtain. It is finally worth to underline that our proposed procedure takes into account the presence of dielectrics by incorporating the effect on the losses and the distributed capacitance of its presence inside the extracted parameters.

2.3.4 Experimental Results

We performed also experimental tests on fabricated spiral resonators: three different rectangular spirals and one square spiral resonator. A summary of the four investigated structures is shown in Fig. 2.6(i). Their geometrical properties are reported in Table 2.4. The chosen dielectric substrate is a 0.8 mm thick Arlon substrate (ε_r = 3.58, $tan\delta$ = 0.0035).

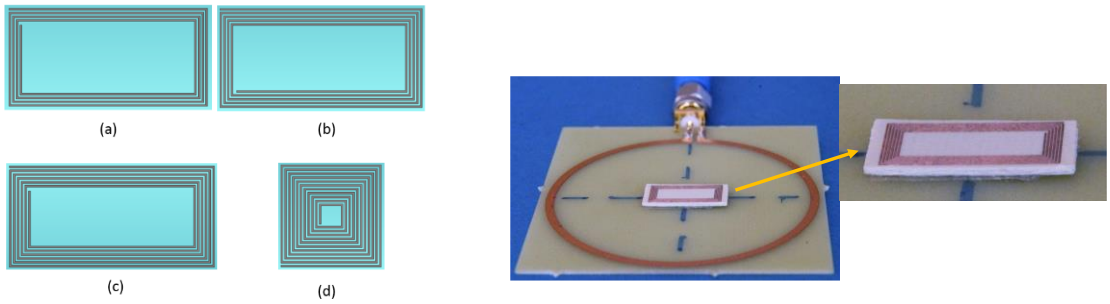

(i) (ii)

Fig. 2.6. (i) Spiral resonators numerical 3D CAD model: (a) Rectangular N=4; (b) Rectangular N=5; (c) Rectangular N=6; (d) Square N=11. (ii) Testing setup for the measurement of the resonance frequency and the impedance of the spiral resonator.

Table 2.4
Properties of the Spiral Resonators in Fig. 2.6(i); Simulated and Measured Resonance Frequencies Are Shown for Comparison

N	$w = s$ (mm)	l_x (mm)	l_y (mm)	f_{sim} (MHz)	f_{meas} (MHz)	*Relative error* (%)
4	0.127	13.7	6.7	386.8	378	2.3%
5	0.127	13.7	6.7	334	327	2.1%
6	0.127	13.7	6.7	293.6	289	1.6%
11	0.127	6.7	6.7	453	442	2.4%

In order to test the spiral resonators, we fabricated also a probe loop characterized by the same dimensions as in Section 2.3.2. The testing setup is shown in Fig. 2.6(ii). The spiral resonator was accommodated exactly in the center of the probe loop. The loop was connected to the Vector Network Analyzer (Keysight E5071C-ENA) through a RF cable with a 50-Ω SMA connector. The resonant frequencies of the four investigated spiral resonators have been obtained by identifying the local minimum in the S_{11} of the probe. Table 2.4 reports the measured resonant frequencies of all the four investigated spiral resonators. We observed a very good agreement between the full-wave numerical result of the resonant frequency (f_{sim})

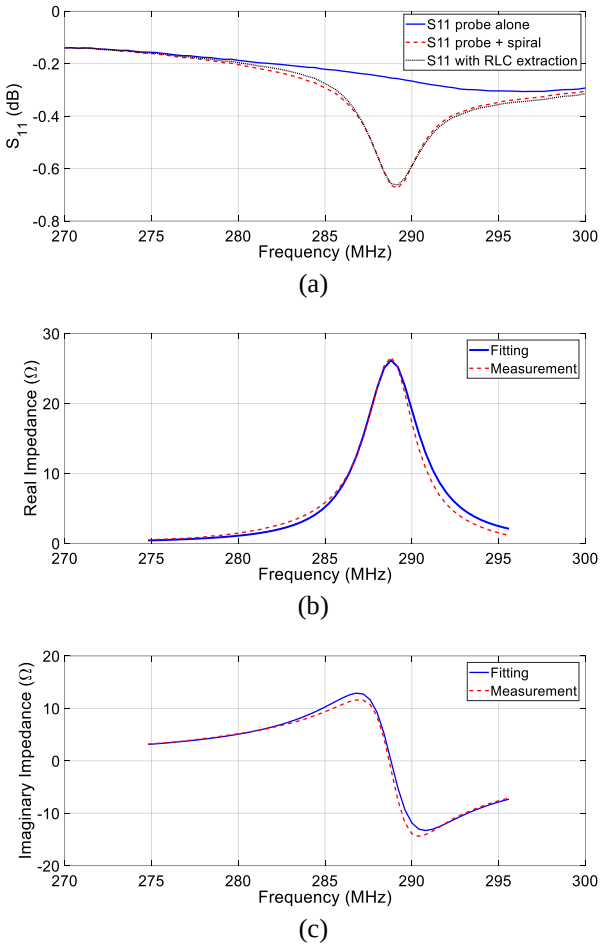

Fig. 2.7. (a) Comparison between measured S_{11} of the larger probing loop with and without the rectangular spiral resonator (N = 6, l_x = 13.7 mm, l_y = 6.7 mm) inside and S_{11} reconstructed from the RLC parameters estimations (fitting); (b) and (c): Real and imaginary de-embedded measured spiral impedance and relative fitting results.

and the measured frequency (f_{meas}) with the proposed method. The relative error between the measurements and numerical simulations was always less than 3% for the considered spiral resonators samples, demonstrating the effectiveness of our approach. Analogously as in previous sections, also the measured S_{11} could be used to quantify the *RLC* parameters of the spiral resonators in addition to the resonant frequency. We replicated the procedure followed for the full-wave simulations for the three rectangular spirals. The lumped parameters estimated through the fitting procedure (Table 2.5) show the same trend obtained with the simulations when the number of turns increases (i.e. R and L increasing and C decreasing).

In particular, Fig. 2.7 shows one of the reconstructed S_{11} parameter starting from the

Table 2.5
Obtained Lumped Parameters of Rectangular Spiral Resonators: Measurements (Simulations)

N	*R* (Ω)	*L* (nH)	*C* (pF)	*Q-factor*
4	7.3 (4.5)	142 (217)	1.251 (0.782)	46.2 (117.1)
5	15.9 (8.0)	404 (442)	0.587 (0.515)	52.2 (115.8)
6	21.6 (10.8)	910 (739)	0.334 (0.398)	76.5 (126.2)

experimentally extracted lumped *RLC* parameters (N=6, l_x=13.7 mm, l_y=6.7 mm). In addition, the figure reports also the de-embedded spiral impedance, fitted with our procedure.

Finally, it must be pointed out that we observed some variations of the *RLC* experimental values with respect to the full wave simulations; this can be addressed to the difficulties to realize a stable measurement environment (presence of losses and distortions). One direct effect of the fabrication of the prototype was the increase of the losses, due to soldering artifacts and connections. Moreover, the etching process can produce a pitting phenomenon, especially for extremely small width copper track as in this case, thus increasing the overall resistance of the path.

2.3.5 Conclusions

A novel accurate procedure for the extraction of the *RLC* parameters representing an isolated spiral resonator has been introduced. We employed an experimental set-up consisting of a probe loop mutually coupled to the spiral resonator under test, which has been schematized through a suitable equivalent circuit topology. We firstly characterized the electromagnetic behavior of the stand-alone probe loop; then, following a magneto-static approach, we evaluated the mutual coupling coefficient existing between the probe and the spiral resonator under test. Finally, after a numerical simulation of the complete system, we extracted the Z_{11} of the probe loop inductively coupled to the spiral resonator and we analytically matched the simulated impedance to the one of the lumped equivalent circuit, to retrieve *RLC* parameters of the spiral resonator. In this way, we obtained an accurate and unambiguous description of the electromagnetic properties of the spiral resonator. We also studied the variation of the *RLC* parameters and the Q-factor as a function of the shape (square or rectangular) and for different number of turns. We discussed the obtained results in terms of

their physical meaning and we showed that a different behavior with respect to some popular analytical models available in the literature has been observed. Finally, we performed measurements of some spiral resonators' shapes, by using a fabricated probe loop. The measured resonant frequencies of SRs are in good agreement with numerical simulation (relative error less than 3%). We also accomplished the *RLC* parameters extraction from the measurements, obtaining a good correspondence with respect to the full-wave simulations, showing the consistency of our approach.

It must be worth noting that the developed procedure is completely general and can be applied to any typology of resonator, allowing a deeper understand and a more effective design of their related applications.

2.4 Spiral Resonators for MRI RF coils decoupling: Distributed Magnetic Traps (DMTs)

As we have introduced, the decoupling method is based on the inclusion of a number of SRs, placed in close proximity of the tuned RF coils, acting as distributed magnetic traps (DMTs). One practical advantage in the adoption of the distributed SRs consists in the use of PCB technology that allows printing the SRs on the same dielectric substrate of the RF coils. This "in plane" decoupling method allows retaining the optimal geometric configuration for the RF coils without the need for additional design constraints.

With the herein introduced approach, we estimate the optimal number of unit cells required for the RF coils decoupling. This is achieved through the analytical evaluation of the mutual coupling, by using a magneto-static approximation, between: *(i)* the RF coils; and *(ii)* each RF coil and a single SR. Finally, the equivalent lumped element circuit describing the overall system is analyzed.

As a test-case for our procedure, we considered a Double-Tuned (DT) RF coil constituted by two concentric and coplanar square loops, tuned at 7 T and suitable for MRI; however, as it will be discussed in the following, the developed approach is general and it can be applied also to planar array tuned at the same frequency. As a practical working example, we considered the two RF coils tuned at the resonant frequency of ^{1}H (298 MHz) and ^{23}Na (79

MHz), respectively. The larger size ^{1}H RF coil allows the acquisition of anatomical imaging, whereas the smaller ^{23}Na RF coil provides information about physiological features, as for example in osteoarthritis or brain tumor detection [75], [79], [80], [100], [108], [115]. The mutual coupling, existing between the two resonant loops, produces a large increase of the resonant frequency of the ^{1}H channel, thus detuning the ^{1}H coil with a deleterious SNR loss. The proposed method is able to reduce or null the mutual coupling between the ^{1}H and ^{23}Na resonant loops. This was done by means of both numerical simulations and experimental measurements on the workbench.

The decoupling approach consists of the following steps:

A. Estimation of mutual coupling between the RF coils;

B. Determination of the number of SRs needed to compensate the coupling estimated at step A;

C. Determination of the SR geometry.

The three steps for optimizing the decoupling SRs are described in the following paragraphs.

2.4.1 Analytical Decoupling Approach

The first step of our procedure requires evaluating the mutual coupling value between the two RF coils. Under magneto-static hypothesis, we apply the Biot-Savart formulation to estimate the mutual coupling between two generic RF coils [8], [120] (as also described in Section 2.3.1). Indeed, as stated before, the main contribute to the mutual coupling at the MRI frequencies is the inductive one [78]. In this way, given the geometrical design of the two RF coils, we can numerically set a unit current flowing in one of them and evaluate the mutual inductive coupling with the other RF coil, taking into account that $M_{ij} = M_{ji}$. Importantly, we can apply this formalism to describe both the coupling between the two RF coils and also between each RF coil and a SR. So, as it will be illustrated later, we are able to fully calculate the components of the impedance matrix Z, characterizing the entire RF system.

Once estimated the mutual coupling values between the two RF coil loops (say M_{12}), it is necessary to design the decoupling SRs. As stated above, SRs can be employed to reduce or null the mutual coupling M_{12}. In particular, a suitable number N of SRs has to be introduced in

between the two RF coils. The network model represents one useful description of the RF system, consisting of the two RF coils and a single SR. The model is formulated using Kirchhoff's voltage law for each coil. In general, we assume that both RF MRI loops can be actively driven. Consequently, since the SR (say loop 3) is a passive element, we adopt voltage sources as driving functions applied to loop 1 (corresponding to the loop mostly affected by the resonant frequency increase) and to loop 2. Finally, the current in each coil is calculated as a function of self and mutual impedance between each element of the system. The lumped elements schematic of this system is shown in Fig. 2.8.

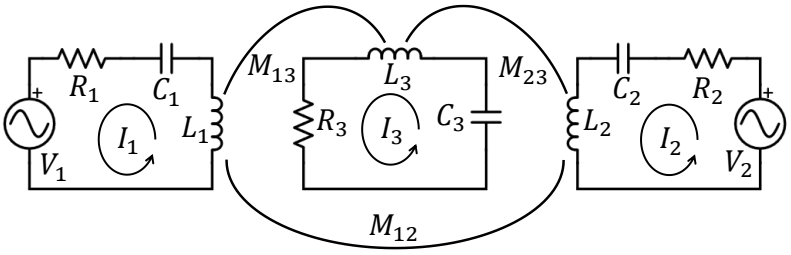

Fig. 2.8. Lumped elements representation of the system constituted by two flux-coupled RF coils (numbered 1 and 2, respectively) and at least a decoupling SR (numbered 3). The presence of the mutual coupling between the RF coils (M_{12}) and also between the RF coils and the SR (M_{13}, M_{23}) is highlighted.

In order to avoid unnecessary complications of the equivalent circuit model, we can hypothesize that the SRs are placed sufficiently far from each other and this, together with their reduced size, implies a negligible mutual coupling among them. Hence, if N identical SRs are placed so that each of them interacts equally with the same RF coil, it is possible to condense the N equations corresponding to each SR into a single condition. The equivalent circuit of Fig. 2.8 thus remains valid once we multiply the mutual terms M_{13}, M_{23} and the SR self-impedance ($R_3+j\omega L_3-j/(\omega C_3)$) by the factor N. This introduces some geometrical constraints on the SRs positioning, but it does not represent a strong limitation due to their small size.

We express the equations of the complete system in a matrix form, taking into account two RF coils and the N SRs. Here the SRs are considered passive elements, and this guarantees that the Z matrix is symmetric.

$$\begin{bmatrix} Z_{11} & Z_{12} & Z_{13} \\ Z_{21} & Z_{22} & Z_{23} \\ Z_{31} & Z_{32} & Z_{33} \end{bmatrix} \begin{bmatrix} I_1 \\ I_2 \\ I_3 \end{bmatrix} = \begin{bmatrix} V_1 \\ V_2 \\ 0 \end{bmatrix} \tag{2.15}$$

Clearly, this matrix system is a compact expression for the following three equations:

$$\begin{cases} (R_1 + j\omega L_1 - j/\omega C_1)I_1 + j\omega M_{12} I_2 + j\omega N M_{13} I_3 = V_1 \\ j\omega M_{21} I_1 + (R_2 + j\omega L_2 - j/\omega C_2)I_2 + j\omega N M_{23} I_3 = V_2 \\ j\omega N M_{31} I_1 + j\omega N M_{32} I_2 + N(R_3 + j\omega L_3 - j/\omega C_3)I_3 = 0 \end{cases} \tag{2.16}$$

where we model the RF coils and the SRs as series resonant *RLC* circuits with diagonal entries of the form $R+j\omega L-j/(\omega C)$.

Keeping in mind the goal of eliminating the mutual coupling between the RF coils at the resonant frequency of the (isolated) coil 1 (the ^{1}H loop, say ω_{01}), we observe from the first equation that this condition can be achieved if $j\omega M_{12}I_2+j\omega N M_{13}I_3=0$. In previous work [79] the mutual coupling was nulled by placing a lumped parallel L-C resonant circuit (trap) in series with loop 2, while loop 1 was kept unchanged. In the present paper the same effect is obtained through at least one distributed resonant circuit (SR) inductively coupled to both coils 1 and 2, making a DMT (the meaning of "magnetic trap" will be clarified in the following).

It is convenient to rearrange the system (2.15) in order to highlight the cross-talking between the two MRI coils (number 1 and 2, respectively). To this aim, the current I_3 in the SRs can be expressed as:

$$I_3 = \frac{-Z_{31}I_1 - Z_{32}I_2}{Z_{33}} \tag{2.17}$$

By replacing relation (2.17) into the first two equations of system (2.15), a system explicitly describing the mutual coupling between the two RF coils in the presence of the SRs is obtained:

$$\begin{bmatrix} Z_{11} - Z_{13}Z_{31}/Z_{33} & Z_{12} - Z_{13}Z_{32}/Z_{33} \\ Z_{21} - Z_{23}Z_{31}/Z_{33} & Z_{22} - Z_{23}Z_{32}/Z_{33} \end{bmatrix} \begin{bmatrix} I_1 \\ I_2 \end{bmatrix} = \begin{bmatrix} V_1 \\ V_2 \end{bmatrix} \tag{2.18}$$

The implementation of the decoupling method allows deriving the condition that the SRs must satisfy to decouple the RF coils. Indeed, the effective $Z_{12_{eff}}$ parameter must be set to zero:

$$Z_{12_{eff}} = Z_{12} - {Z_{13}Z_{32}}/{Z_{33}} = 0 \tag{2.19}$$

In the hypothesis of N SRs tuned at the resonant frequency f_{SR} and in the absence of mutual coupling between them, this equation, at the desired resonant frequency ω_{01} of coil 1, can be rewritten as:

$$j\omega_{01}M_{12} = \frac{j\omega_{01}NM_{13}j\omega_{01}NM_{32}}{N(R_3+j\omega_{01}X_3)} \tag{2.20}$$

where X_3 (equivalent inductance of the single SR self-impedance) is represented by:

$$X_3 = L_3 - \frac{1}{\omega_{01}^2 C_3} \tag{2.21}$$

In Appendix A, a physical interpretation of condition (2.20) is derived in terms of equivalent medium. Rearranging (2.20), considering that M_{32}=M_{23}, and distinguishing the real and the imaginary components of the right member of the equation, in order to fulfill the condition, we obtain:

$$\begin{cases} j\omega_{01}M_{12} = \frac{j\omega_{01}^3 NM_{13}M_{23}X_3}{R_3^2+\omega_{01}^2X_3^2} \\ 0 = \frac{-\omega_{01}^2 NM_{13}M_{23}R_3}{R_3^2+\omega_{01}^2X_3^2} \end{cases} \tag{2.22}$$

where the first equation of system (2.22) corresponds to null the imaginary component of the term $Z_{12_{eff}}$. It must be noted that in practical conditions the second equation of (2.22) cannot perfectly satisfied. This term arises because of the finite resistance of the SR. In order to keep this term low (i.e., negligible resistive losses), it is necessary that:

$$\omega_{01}^2 X_3^2 \gg R_3^2 \tag{2.23}$$

Under condition (2.23), the first equation in (2.22) can be satisfied when:

$$X_3 = \frac{NM_{13}M_{23}}{M_{12}} \tag{2.24}$$

By replacing (2.24) in (2.23), it is straightforward finding the minimum number *N* of SRs such that the real part of (2.22) is negligible:

$$N^2 \gg \left(\frac{M_{12}R_3}{\omega_{01}M_{13}M_{23}}\right)^2 \tag{2.25}$$

Once a proper number of SRs is chosen, from (2.24) it is possible to find out the value of the reactance that the SR must have at the desired working frequency ω_{01}. In this way, the imaginary component of the mutual coupling is compensated.

At this point, the real term of the mutual coupling must be evaluated; if it is not sufficiently low with the chosen *N*, then a greater number of SRs must be used in order to better verify condition (2.23). Indeed, the real term diminishes with an increasing number *N* of SRs:

$$\begin{aligned}\frac{-\omega^2 NM_{13}M_{23}R_3}{R_3^2+\omega^2X_3^2} \cong \frac{-\omega^2 NM_{13}M_{23}R_3}{\omega^2X_3^2} = \\ = \frac{-\omega^2 NM_{13}M_{23}R_3}{\omega^2(\frac{NM_{13}M_{23}}{M_{12}})^2} = \frac{-M_{12}^2R_3}{NM_{13}M_{23}}\end{aligned} \tag{2.26}$$

Obviously, the presence of the SRs has a significant effect also on the impedance of coil 1. Indeed, as shown in (2.18) the effective $Z_{11_{eff}}$ is written as:

$$Z_{11_{eff}} = Z_{11} - {Z_{13}Z_{31}}/{Z_{33}} \tag{2.27}$$

Substituting the respective physical quantities, it becomes:

$$\begin{aligned}Z_{11_{eff}} = (R_1 + \frac{\omega_{01}^2 NM_{13}M_{31}R_3}{R_3^2+\omega_{01}^2X_3^2}) + \\ +j(\omega_{01}L_1 - \frac{1}{\omega_{01}C_1} - \frac{\omega_{01}^3 NM_{13}M_{31}X_3}{R_3^2+\omega_{01}^2X_3^2})\end{aligned} \tag{2.28}$$

This means that the employed SRs contribute with additional terms to the real and imaginary components of the self-impedance of coil 1. Such contribute must be considered when the tuning and matching process of coil 1 is carried out. It must be noticed that the condition about the mutual coupling reduction, developed here with the described network

model, is also valid in the presence of feeding ports with their own impedances; as a matter of facts, the mutual coupling is not affected by the feeding ports properties.

Moreover, the model is general and can be applied for both dual tuned and planar array configurations. Indeed, only the mutual coupling between side-by-side array elements is commonly considered significant [85]. Therefore, the decoupling scheme is exactly the same of a dual tuned configuration, i.e. inserting opportunely spiral resonators to reduce mutual impedance between two adjacent MRI loops (Fig. 2.9).

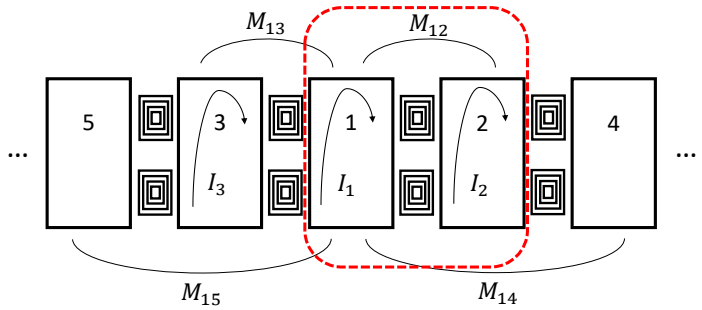

Fig. 2.9. Schematic drawing depicting a planar MRI array: if only the coupling between side-by-side elements is considered significant, the decoupling scheme is the same of a DT configuration.

Clearly, the presented decoupling method has a certain degree of approximation. However, we believe that the proposed analytical approach can be useful since it provides a meaningful estimation of the required number of SRs, starting only from magneto-static considerations. The alternative to this approach is a highly expensive computational simulations method, leading to an optimized solution without a physical understanding of the coupling reduction mechanism. On the contrary, in this case, the fine-tuning of the analytical solution can be aided through few and targeted full-wave simulations.

2.4.2 Spiral Resonator design

The SRs, consisting of *k*-turn planar spiral loop coils, are printed on the same dielectric substrate of the RF coils.

In order to satisfy the hypothesis stated before, and act as a DMT circuit for coil 2, the SRs must fulfill the condition expressed in (2.23)-(2.25); i.e. they should present, at the resonant frequency ω_{01} of coil 1, an appropriate reactive impedance, related to the mutual coupling coefficients and the number *N* of SRs. The geometrical design of the single SR must

be appropriate for the available space between the RF coils and also able to satisfy the decoupling criterion. Once the exploitable dimensions are determined, we can apply the following formulation in order to find the geometry and number of turns satisfying the above stated conditions.

A SR can be approximated as an LC circuit [100], [115]. The total distributed inductance and capacitance can be determined starting from its geometrical parameters. In particular, we can set the dimensions l_x and l_y, the number of turns k, the widths (w_x and w_y) of the conductor strip, the gap between each loop (s_x and s_y), the dielectric material (ε_r and $tan\delta$) and its thickness h. Without loss of generality, we can assume for simplicity that $w_x = w_y = w$ and $s_x = s_y = s$ (Fig. 2.10).

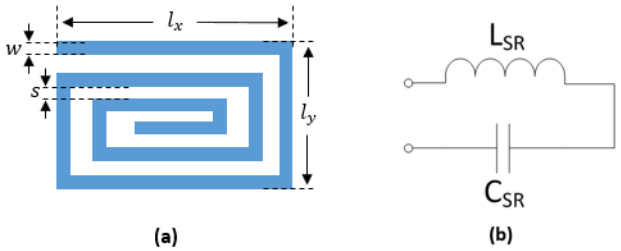

Fig. 2.10. Spiral resonator acting as distributed trap filter: (a) geometrical parameters (drawing not in scale); (b) magneto-static equivalent circuit (assuming no losses).

The L_{SR} and C_{SR} values determine the resonant frequency of the spiral:

$$f_{SR} = \frac{1}{2\pi\sqrt{L_{SR}C_{SR}}} \tag{2.29}$$

As we have reported in Section 2.3, the analytical formulas based on SR geometry provide a quite accurate estimated resonant frequency, thus they can be very helpful in the design of an SR close to the desired working point. Specifically, we exploited a different version of the method proposed in [100], [115], extending the formulation to rectangular spiral shapes. In particular, we modified the expression for the total strip length, with respect to the previous model presented in the literature, taking into account the two dimensions of a rectangular shape. The following expressions describe the conductor strip total length of the generic k^{th} turn of a rectangular spiral:

$$\begin{cases} l_k = 2l_x - 2l_y - (w+s), & if \quad k = 1 \\ l_k = 2[l_x - 2(k-1)(w+s)] + \\ +2\big[l_y - 2(k-1)(w+s)\big], & if \quad k > 1 \end{cases} \tag{2.30}$$

The distributed capacitance is due to each couple of branches in the spiral, that realizes a capacitor. Therefore, it can be estimated starting from the total gap length of the spiral:

$$\begin{cases} l_k^{gap} = 2\big[l_x + l_y - 4(w-s)\big], & if \quad k = 1 \\ l_k^{gap} = 2[l_x - 2k \cdot w - 2(k-1)s] + \\ +2\big[l_y - 2k \cdot w - 2(k-1)s\big], & if \quad k > 1 \end{cases} \tag{2.31}$$

As described in [29], [30], the presence of the dielectric substrate clearly affects the resonant frequency by multiplying the total capacitance value for the effective dielectric permittivity. We used a modified expression, given in [118], to estimate the effective ε_r:

$$\varepsilon_r^{eff} = \frac{\varepsilon_r+1}{2} + \left(\frac{\varepsilon_r+1}{2} - 1\right)e^{-\left(\frac{\alpha h}{(2w+l)}\right)} \tag{2.32}$$

With respect to the formulation reported in [100], [115], eq. (2.32) converges, for increasing thickness *h*, to the average permittivity value between air and substrate with a speed that can be modulated by the parameter α. This behavior is more realistic rather than a saturation value equal to the permittivity of the employed dielectric, since the substrate is present only on one side of the coil. Thanks to this formulation, we can design a SR with the desired resonant frequency, which also satisfies the geometrical constraints required by the RF coil loops configuration.

However, as it was illustrated in Section 2.3 ([8]), the lumped inductance and capacitance retrieved by using this analytical model based only on the resonator's geometrical properties are not accurate. To overcome this limit, once the designed spiral resonator is satisfying the geometrical constraints and working frequency, we characterize its effective RLC equivalent circuit by using the procedure presented in Section 2.3.1 ([8]). This step is fundamental to estimate accurately the reactive impedance of the resonator required for decoupling and, eventually, to refine its design.

At this point, we must fix the number of SRs to compensate the mutual coupling between the RF coils. We have to evaluate the mutual coupling between each RF coil and the designed SR, by using the magneto-static approximation. Afterwards, we follow the procedure given in the section 2.4.1; in particular, the required number *N* of SRs is given in eq. (2.25). In addition, the positioning of the *N* SRs must be carefully evaluated. It is necessary to place the SRs as far as possible from each other, to make negligible the mutual coupling between them but keeping the same distance from the main coils to have constant mutual induction values.

2.4.3 Double-tuned case study: numerical simulations

As previously introduced, we chose as test case the design of a 7 T DT RF coil made by two coplanar and concentric rectangular loops, with the inner RF loop tuned at the Larmor frequency of ^{23}Na (79 MHz), whereas the outer RF loop is tuned at the Larmor frequency of ^{1}H (298 MHz). Because of the coplanar and concentric geometry, a strong mutual coupling arises, causing a large upshift of the ^{1}H RF coil frequency.

The ^{1}H RF coil is a rectangular loop made by a 4 mm width copper strip (35 μm thick) with external sizes equal to 116 mm and 108 mm, respectively. The inner ^{23}Na loop measures 92 mm × 84 mm (copper width of 4 mm, with 35 μm thickness). The resulting gap size between the two RF coils is equal to 8 mm. Given this geometrical setup, we numerically implemented the analytical procedure for the mutual coupling estimation (Section 2.4.1): the estimated magneto-static mutual coupling coefficient between the two RF coils is equal to $M_{^{1}H^{23}Na}$=117 nH.

Through preliminary full-wave simulations, we noticed that, although each isolated RF coil was correctly tuned at its resonant frequency, the presence of the mutual coupling caused, as expected, a relevant upshift of the ^{1}H RF coil resonant frequency (about 25 MHz) and a negligible downshift of the ^{23}Na RF coil resonant frequency.

To null the mutual coupling, we used 4 SRs placed symmetrically in the gap between the two RF coils, exploiting the maximum width of 8 mm, and positioned at half-length of their branches. This geometry guarantees: *(i)* negligible coupling among SRs; and *(ii)* the mutual coupling invariance among each SR and the ^{1}H RF coil, as well with respect to the ^{23}Na RF

coil. Thus, the requisites in the analytical calculations presented in Section 2.4.1 can be fulfilled.

In particular, by exploiting the formulation reported in Section 2.4.2, we designed a k = 6 turns planar SR tuned, when isolated, at about 300 MHz, with size l_x = 13.7 mm and l_y = 6.7 mm, respectively. The conductor width w was set equal to 0.127 mm, with a 35 μm thickness. The estimated self-inductance value was 748 nH, whereas the self-capacitance resulted in 0.37 pF [8].

We then analytically estimated the mutual coupling between each RF coil and a single SR placed in the gap between them. Because of the chosen geometry, the mutual coupling coefficient of the SR resulted practically equivalent for both the RF coils, but with inverted sign: M_{1HSR} = 24 nH = -M_{23NaSR}. The sign inversion is due to the symmetric position of the SRs with respect to the RF coils and the flux induced by the currents (same sign) circulating in the RF coils is opposite. In addition, we analytically verified — through the magneto-static procedure — that, in the present conditions, the mutual coupling coefficient between each pair of SRs was actually negligible (equal to 76.8 pH).

Now, as described in Section 2.4.1, we must satisfy inequality (2.25), choosing the minimum number of SRs that guarantees the decoupling condition. The resistance value R_3 of the single SR was estimated in 10.8 Ω: selecting N=4, the condition in (2.25) was close to be satisfied (16≫1.16, one order of magnitude). Thus, N=4 was the minimum number of SRs able to guarantee condition (2.25), allowing a symmetrical positioning of the SRs around the two coils. This has the additional beneficial effect in terms of symmetry of the magnetic field distribution inside the FOV of the DT RF coil.

Under the retrieved mutual coupling coefficients, lumped parameters and number of employed SRs (summarized in Table 2.6), the ideal reactance of the single SR should satisfy (2.24) (i.e X_3 = -19.7 nH) at the frequency of interest (298 MHz).

In addition, it is worth to note that the 4 SRs produced a reflected impedance value for coil 1 that must be matched through an appropriate network in a practical scenario.

Afterwards, we performed full-wave simulation of the designed overall system (CST Microwave Studio, Darmstadt). Initially, the two standalone RF coils were tuned and matched at about 298 MHz and 79 MHz, respectively. Each RF coil consisted of a rectangular loop

etched on a 0.8 mm thick dielectric substrate (Arlon, ε_r = 3.45, $tan\delta$ = 0.0035) and interrupted by lumped elements (see Fig. 2.11).

The desired resonant frequencies of the standalone RF coils were obtained with a set of tuning capacitance values summarized in Table 2.7. Besides, the capacitive balanced matching networks allowed an efficient 50-Ohm matching and the corresponding values are reported in Table 2.7.

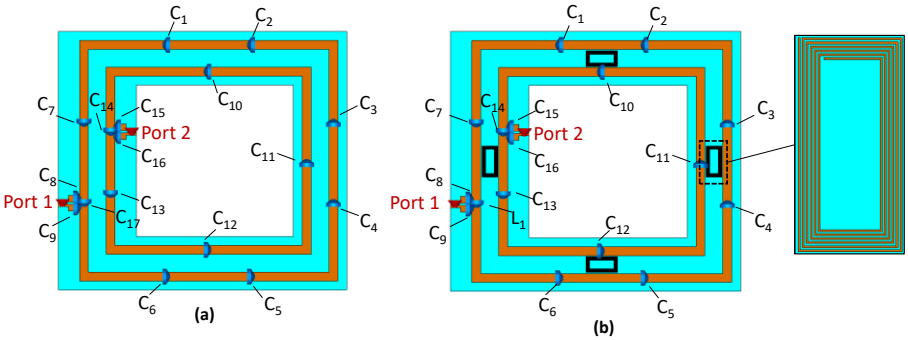

Fig. 2.11. Complete 3D numerical CAD of: (a) ^{1}H and ^{23}Na RF coils together without the SRs; and (b) ^{1}H and ^{23}Na RF coils together with the SRs in place. An inset of the used SR is inserted for clarity.

Table 2.6
Physical Parameter Describing our Test Case at 298 MHz

$M_{1_H 23_{Na}}$ (nH)	$M_{1_{HSR}}$ (nH)	$M_{23_{NASR}}$ (nH)	N	R_{SR} (Ω)	L_{SR} (nH)	C_{SR} (pF)
117	24	-24	4	10.8	748	0.37

Table 2.7
Matching and Tuning Capacitors of the Standalone DT RF Coil

Capacitors	*Function*	*Value*
C_1, C_2, C_3, C_4, C_5, C_6, C_7	^{1}H tuning	6.1 pF
C_{17}	^{1}H tuning	27 pF
C_8, C_9	^{1}H matching	60 pF
C_{10}, C_{11}, C_{12}, C_{13}	^{23}Na tuning	82 pF
C_{14}	^{23}Na tuning	20 pF
C_{15}, C_{16}	^{23}Na matching	20 pF

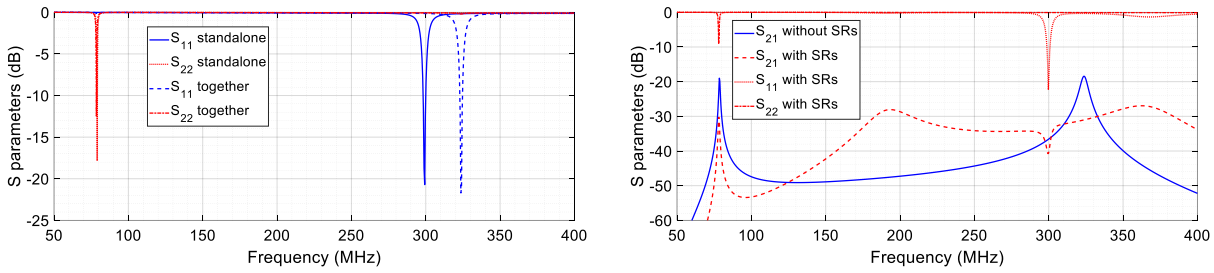

(a) (b)

Fig. 2.12. (a) Simulated *S* parameters (dB) of the standalone ^{1}H (S_{11}) and ^{23}Na (S_{22}) RF coils (solid lines) versus the values when the two RF coils are placed together (dashed line) without the use of SRs. (b) Simulated *S* parameters (dB) of the two RF coils: S_{12} without SRs (solid line); S_{12} with SRs (dashed line), S_{11} (dotted line, ^{1}H) and S_{22} (dash-dotted line, ^{23}Na) with SRs.

Figure 2.12(a) shows the reflection *S* parameters (S_{11} and S_{22}) of the standalone RF coils (solid lines) and the same coils placed together (dashed lines). When the RF coils are isolated, they present an excellent tuning and matching at the desired resonant frequencies. Then, the two RF coils were placed in a planar and concentric disposition to evaluate the degree of mutual coupling. Once arranged together, a noticeable upshift (about 25 MHz) of the ^{1}H resonant frequency is observed (Fig. 2.12(a), dashed line) due to a strong mutual coupling, while the ^{23}Na resonant frequency is not affected. With the purpose of correcting the ^{1}H frequency shift, 4 SRs were inserted in between the RF coils, according to the performed design. As theoretically predicted in Section 2.4.1, the insertion of the SRs caused a detuning and a mismatch of the ^{1}H loop.

Both effects were compensated by adjusting the lumped elements values (see Table 2.8). At the end of the procedure, the two RF coils and the SRs worked together as predicted at the desired frequencies, with a drastic decoupling effect visible in the S_{12} parameter, as shown in Fig. 2.12(b). It can be noticed that the S_{12} without the SRs shows a peak (-18 dB) at the upshifted ^{1}H resonant frequency of about 325 MHz, while, with the SRs, the restored resonant frequency for the ^{1}H loop is about 298 MHz, with a minimum S_{12} of -40 dB. Moreover, the results of Fig. 2.12(b) show that the S_{12} at the ^{23}Na frequency improves from about -20 to -30 dB. These numerical full-wave results confirmed the efficacy of the novel decoupling method herein described.

Table 2.8
Matching and Tuning Capacitors of the DT RF Coil After the Insertion of 4 SRs

Capacitors	*Function*	*Value*
C_1, C_2, C_3, C_4, C_5, C_6, C_7	^1H tuning	5.8 pF
L_1	^1H tuning	100 nH
C_8, C_9	^1H matching	8.8 pF
C_{10}, C_{11}, C_{12}, C_{13}	^{23}Na tuning	82 pF
C_{14}	^{23}Na tuning	82 pF
C_{15}, C_{16}	^{23}Na matching	20 pF

2.4.4 Distributed Magnetic Trap Power Handling

Although being an attractive solution for decoupling purposes, spiral resonators can raise concerns about their power handling effective capability during a real case RF MRI high-power input signal. In particular, the small spacing between a single spiral and the MRI coils and their tiny copper traces can be a potential source for electric arcing.

Thus, we performed full-wave simulations to obtain electric field distribution along the entire structure considering a high-power input signal at the coils' ports. Following [87], we set the input signal as a 300 Wpp continuous wave and we evaluated the electric field at a plane 20 μm above the dielectric substrate. In this way, considering a 35 μm thick copper trace, we obtained the field distribution also in between two adjacent spiral branches, which corresponds to the location with the smallest gap between conductors in the entire structure.

As expected, the highest values of the field were located in correspondence of the spiral resonators (Fig. 2.13 (a)); indeed, their small dimensions and nested structure have a concentration effect on the field. However, taking as a conservative reference the electric strength of the air (3 MV/m), we found that no risk of arcing is present in our design (Fig. 2.13 (b)). In addition, we evaluated also the field inside the dielectric slab (Fig. 2.13 (c)); considering that the dielectric has an electric strength much more pronounced than air, no problem was also present inside the slab.

Hence, we concluded that the structure can handle without concerns input powers of a typical MRI sequence, thus demonstrating the robustness of the proposed solution.

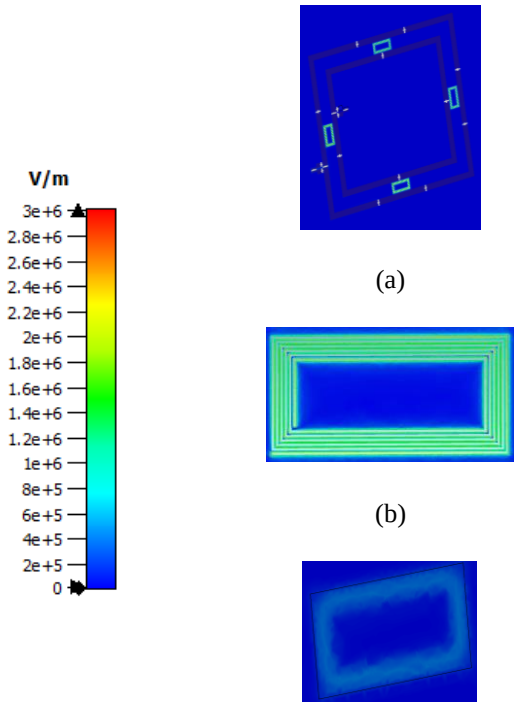

Fig. 2.13. (a) Electric field distribution in the complete MRI system at a plane 20 μm above the substrate: it can be seen that the peak values are in proximity of the spirals. (b) Particular of the field distribution on a spiral resonator, which corresponds to the highest field location. (c) Electric field inside the dielectric substrate. All the distributions show that the electric strength of the air is never overcome in the entire structure.

2.4.5 Sensitivity to errors evaluation

Another important point to be analyzed consists in the sensitivity evaluation of the proposed design procedure against potential variations in the required parameters. Specifically, spiral resonators' self-impedance and their mutual coupling coefficients with MRI coils can be affected by errors since they are estimated by using a magneto-static approach.

We first calculated the *S*-parameters from the analytical model proposed in Section 2.4.1 by using the analytically estimated parameters and comparing them with full-wave simulations performed in CST (Fig. 2.14). Although a static approximation cannot fully describe all the phenomena happening in the system, it is sufficiently accurate in the unloaded condition to achieve a robust filter design, very close to the full-wave results.

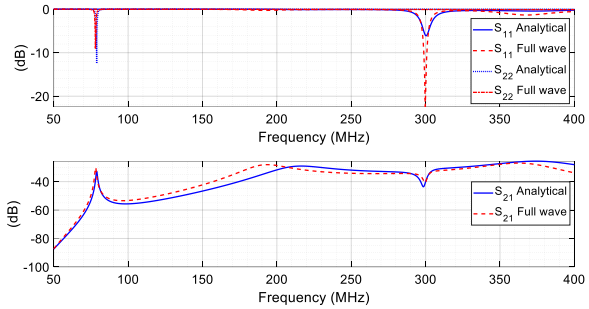

Fig. 2.14. Comparison between *S*-parameters obtained using the analytical model and full-wave simulations in presence of the spiral resonators: the magneto-static approximation used to achieve filter design proved robust.

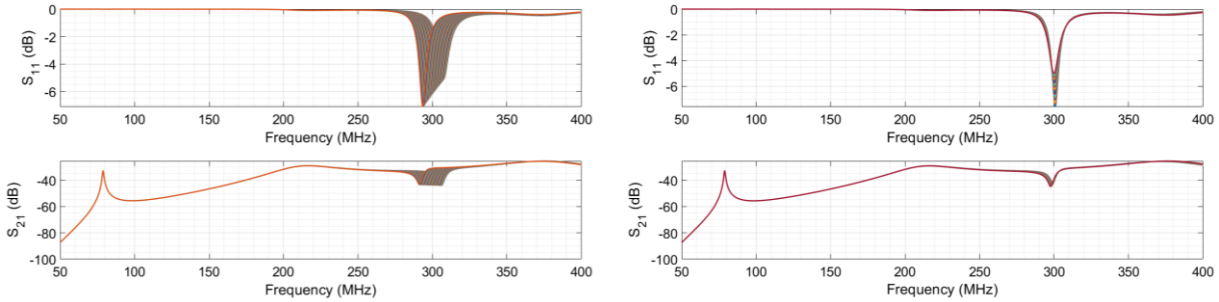

(a) (b)

Fig. 2.15. S_{11} and S_{21} sensitivity evaluation with respect to error sources. (a) ±2.5 % variability on SRs' self impedance; (b) ±10 % variability on mutual coupling coefficients between SRs and MRI coils. In both cases, our design procedure is robust and can be applied without concerns.

After that, since we could not use full-wave simulations to evaluate possible errors on mutual coupling coefficients and SRs self-impedance estimations (they are estimated using analytical static models), we exploited again the circuital model. We imposed an error on the analytical parameters we originally used to design the filter (i.e., the results in Fig. 2.14) and we evaluated variations in *S*-parameters. We performed two analysis: one changing the values of the mutual coupling coefficients between SRs and MRI loops, the other changing the SRs self-impedance (i.e., L and C) (Fig. 2.15). We did not report the study performed on the ^{23}Na loop (S_{22} parameter) because it was minimally affected by such variations, being significantly out of resonance around 300 MHz.

We independently imposed a ± 2.5 % of variability to the inductance and capacitance values of the resonators, and a ± 10 % on the mutual coupling coefficients between SRs and MRI

coils, in accordance to measurements uncertainties performed in [8]. As reported in Fig. 2.15, the design is overall robust against error sources; in particular, we obtained a ± 2.26 % frequency shift in the minimum of the S_{11} (^{1}H loop) when the spirals' self-impedance is changing and a ± 0.15 % shift with the error on the mutual coupling coefficients. On the other hand, the frequency shift in the minimum of the S_{21} is varying between ± 2.5 % with SRs self-impedance uncertainties and ± 0.27 % with mutual coefficients fluctuation.

Hence, we concluded that our design procedure is robust enough against the main sources of error and can be applied to real scenarios with confidence.

2.4.6 Experimental Verification

We fabricated prototypes of the concentric RF coils without and with the SRs. The RF coils were tuned, matched and equipped with 50-Ohm coaxial connectors, evaluating both the unloaded configuration and the RF system in presence of a biological load (Fig. 2.16). As a biological load, we chose a cylindrical bottle of saline solution (NaCl, 0.05 M), 18 cm height and with a 9 cm diameter. Its electric properties are similar to the human tissue at 300 MHz (ε_r = 76, σ =0.56 S/m).

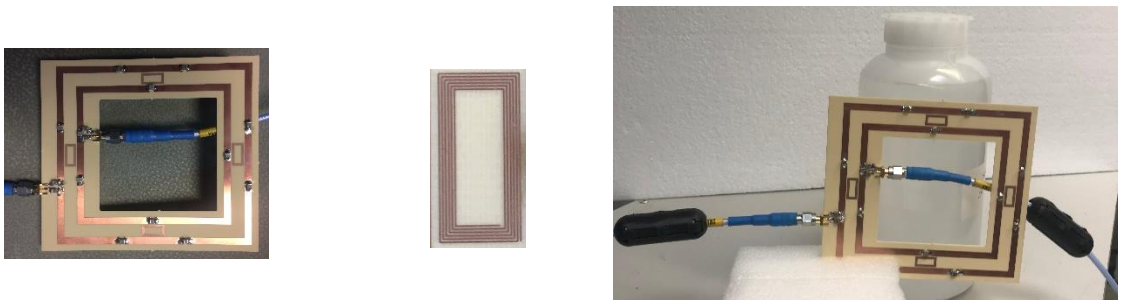

(a) (b) (c)

Fig. 2.16. ^{1}H and ^{23}Na RF coil prototypes in presence of the DMT filter: (a) unloaded system; (b) particular of a single spiral resonator; (c) complete system with a biological load (saline solution, 0.05 M).

We performed the measurements of the *S*-parameters at the Vector Network Analyzer (VNA) (E5071C ENA, Keysight). The measured *S*-parameters of the RF coils prototypes without and with SRs in the two loading conditions are shown in Fig. 2.17. As evident from the results, the presence of the SRs restores the correct resonant frequency for the ^{1}H RF coil

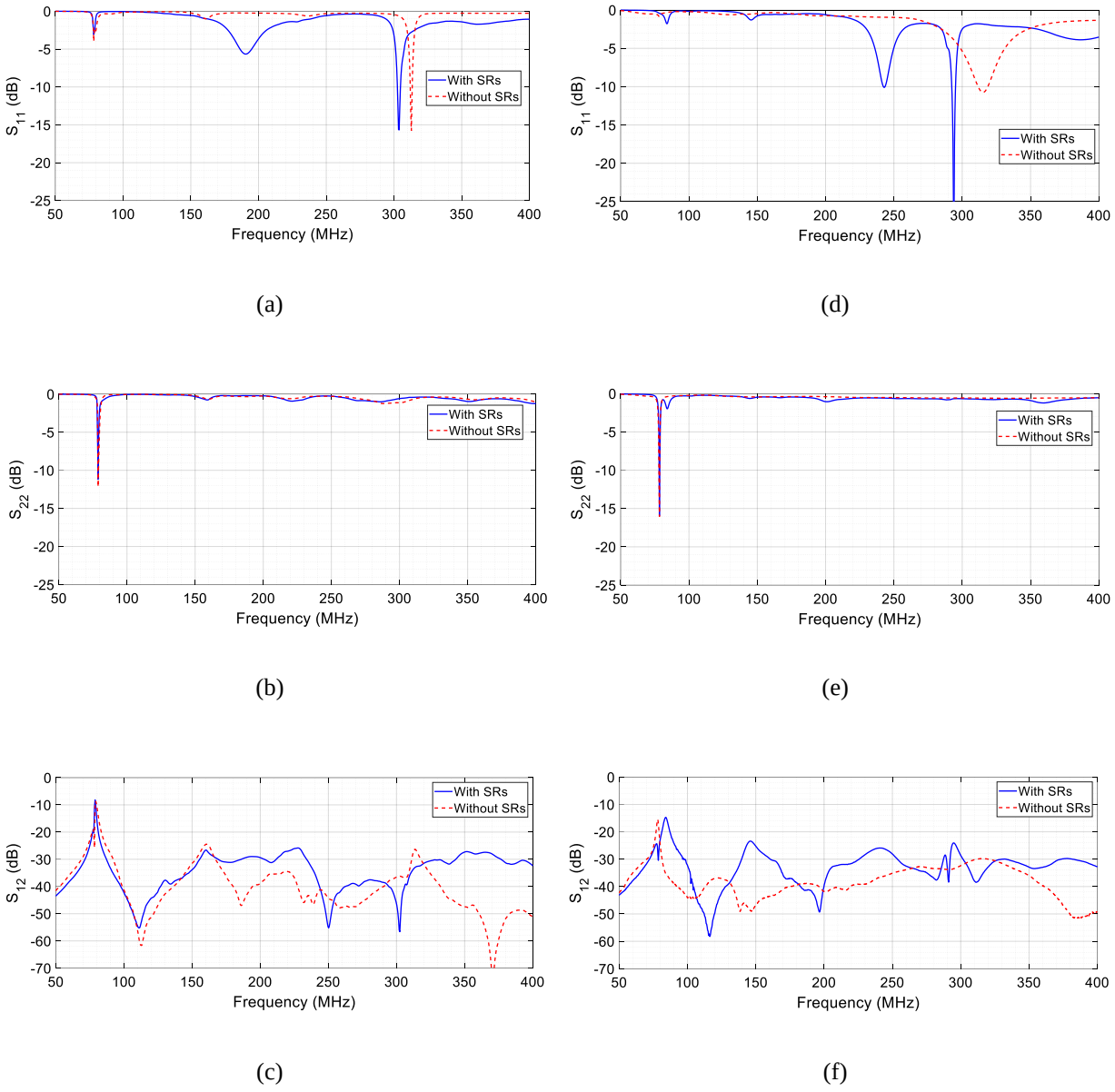

Fig. 2.17. Measured *S* parameters of the RF coil prototypes without (dashed line) and with (solid line) SRs. Left (right) column: without (with) biological load. (a), (d) S_{11} parameter (dB) measured from the ^{1}H channel; (b), (e) S_{22} parameter (dB) measured from the ^{23}Na channel; (c), (f) S_{12} parameter (dB).

and drastically reduces the mutual coupling with the ^{23}Na loop. It must be pointed out that the slight differences in the experimental resonant frequencies with respect to the numerical simulations are in agreement with previous works [129] and are compatible with the

tolerances of the lumped components and with imperfections of fabrication (e.g., etching, dielectric substrate variability, soldering procedure). The measurements variations were always within a 5% tolerance with respect to full-wave simulations, thus in good agreement with numerical design.

One possible concern about the SRs adoption is the negative effect on the efficiency of the RF coils due to additional resistive losses. In order to verify the impact of the SRs losses on the RF coils, we reported in Table 2.9 the measured Q-factors of the standalone ^{1}H and ^{23}Na RF coils, without and with the SRs in place, obtained from the S_{21} measurement with a standard probe ($Q=f_0$/Bandwidth (-3 dB)). We performed measurements in free space and with the biological phantom previously described. It can be seen that the measured Q-factors in unloaded condition showed a very small degradation for the ^{23}Na coil (4 %) and a moderate decrease for the ^{1}H coil (23 %). In the presence of the load, the ^{1}H Q-factor underwent to an 18 % decrease, while the ^{23}Na loop suffered for a 30 % reduction.

In general, the phantom presence is the cause for a significant decrease of the Q-factor, as it was expected. However, these experimental results suggest that the sensitivity of the ^{23}Na coil, the most critical for in vivo applications because of the low natural ^{23}Na concentration in the tissues, remains significantly high even in presence of both the distributed trap and biological phantom. The larger losses measured in the ^{1}H RF coil are mostly due to the need of inserting the (lossy) inductor in series with the ^{1}H loop, in order to reach a good degree of matching/tuning. However, given the natural abundance of the ^{1}H signal, this is not critical for the envisaged applications at 7 T. Alternative matching/tuning methods requiring only high-quality capacitors can be employed in future designs of the ^{1}H coil in the presence of the SRs to improve the Q.

Finally, it must be pointed out also that measurement errors can introduce some variability on these values.

Table 2.9
Measured Q-Factors of ^{1}H and ^{23}Na RF Coils Without and With Spiral Resonators

	Without SRs, no load	*With SRs, no load*	*Without SRs, load*	*With SRs, load*
^{1}H standalone RF coil	124	95	97	82
^{23}Na standalone RF coil	317	304	237	181

2.4.7 Conclusions

A novel analytical procedure for the design of distributed SRs, useful for the decoupling of MRI RF coils was introduced. We selected as test-case the design of a DT (^{1}H/^{23}Na) RF coil configuration suitable for 7 T MRI, consisting of two concentric and coplanar loops. We have shown that 4 SRs, printed on the same dielectric substrate of the RF coils, act as a distributed magnetic trap (DMT) circuit. The design of the whole decoupling system was performed through a fast and reliable fully analytical procedure, which is able to give a physical insight of the mutual coupling mechanism between the RF coils and SRs. Moreover, it is possible to choose the correct number, typology and position of the SRs, thus achieving a design close to the optimum. The refinement of the distributed SRs performance can be carried out through few targeted full-wave simulations. The feasibility of the proposed approach has been demonstrated by running full-wave simulations and experimental measurements on fabricated RF coil prototypes. Optimal decoupling (better than –40 dB) at the resonant frequency of the ^{1}H was achieved with 4 distributed SRs, placed symmetrically in between the ^{1}H and ^{23}Na RF coils. Even in the presence of the SRs and of a realistic phantom, the quality factors of the ^{23}Na and ^{1}H coils remain significantly high to be suitable for practical scenarios.

The technology of printing the SRs over the same dielectric substrate of the MRI coils results in a major advantage with respect to the traditional lumped elements trap circuit. Indeed, the flat design of the SRs allows a neat implementation without the need for extra space on top of the coplanar RF coils. Finally, although we selected as test-case the design of a DT RF coil configuration, the same analytical procedure can be also extended to RF coil arrays suitable for parallel imaging.

3 CHAPTER 3: RESONANT INDUCTIVE WIRELESS POWER TRANSFER FOR BIOMEDICAL APPLICATIONS

3.1 Introduction

Resonant inductive Wireless Power Transfer (WPT) currently represents a fast-growing branch of electromagnetic research. Although the origin of inductive wireless energy transmission between resonant driving loop and passive receiver dates back to Tesla [130], [131], the ever-increasing need for contactless charging systems has spearheaded significant research and contributions in this field in recent times. In fact, a number of different fields nowadays benefit from WPT systems, such as rechargeable devices, automotive applications and biomedical implants [132]–[141]. From a physical point of view, the technique exploits the well-known Faraday's induction law: the driver magnetic field produces a time-varying magnetic flux through the passive receiver coil area and, consequently, a voltage potential on the receiver's terminals is induced:

$$\oint_L \vec{e} \cdot \hat{\imath}_l dl = -\frac{\partial}{\partial t} \iint_S \vec{b} \cdot \hat{\imath}_n dS \tag{3.1}$$

The term on the left of eq. (3.1) is the electric field circuitation along the receiver coil (i.e., the voltage drop at its terminals), whereas the right term represents the time derivative of the flux concatenated in the receiver area produced by the driver magnetic field.

A resonant inductive WPT configuration consists, in its simplest version, of a single driver and receiver, both resonant at the same frequency (Fig. 3.1):

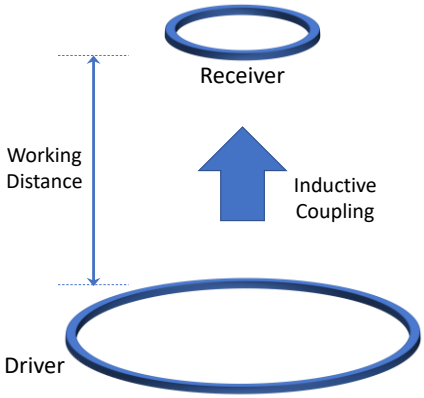

Fig. 3.1. Basic resonant inductive Wireless Power Transfer configuration: one fed driver inductively coupled with a passive receiver, both resonant at the same operative frequency.

The system constituted by the two mutually coupled resonant coils can be translated into the following equivalent circuital model [65], [119], in which the coupling term (Z_M) is highlighted (Fig. 3.2). In particular, the useful resistive load representing the device to be powered on is indicated as R_{load}.

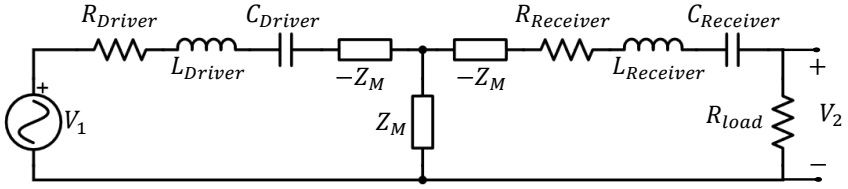

Fig. 3.2. Equivalent circuit of an inductive wireless power transfer system; the useful load at the receiver is in a series configuration.

At this point, it may be worth noticing that three main quantities have to be defined to fully characterize the performance of a WPT device: working distance, efficiency η and gain. Working distance can be described as the available space between the driver and receiver sides, as indicated in Fig. 3.1. Larger working distances mean extending the range of the energy transfer, thus increasing the number of potential applications in which the WPT device can be employed.

Instead, as reported in [142], gain and efficiency can be expressed in terms of input and output voltage amplitude and RMS (root mean square) power, respectively:

$$\begin{cases} \eta = \frac{P_{out}}{P_{in}} = \frac{R_{load}|I_{load}|^2}{|V_1||I_1|} \\ Gain = \frac{|V_{out}|}{|V_{in}|} = \frac{R_{load}|I_{load}|}{|V_1|} \end{cases} \tag{3.2}$$

Specifically, the gain is a parameter which is important to consider especially when the inductive link is used also for data transfer (i.e., telemetry). Indeed, WPT systems are frequently used for telemetry in combination with power delivery [143]–[148]. In this case, the amplitude and the -3 dB bandwidth of the gain must be carefully considered along with the energy transfer efficiency.

Starting from the simple configuration depicted in Fig. 3.1, many other solutions have been developed to continuously increase the performance of such systems. Indeed, despite the undoubtful attractiveness of being free from cables, one of the major concerns in resonant

inductive WPT is the quick decay of the near field components. The magnetic field decays from the active coil proportionally to the cube of the distance from the passive receiver coil (~$1/d^3$). For this reason, significant research found in the literature is directed towards exploring solutions to improve both efficiency and working distance in inductive wireless power transfer applications. 3 or 4-coil systems [142], [149]–[156], metamaterials and metasurfaces [157]–[160], paramagnetic response [161], Bessel beam launchers [162], bidimensional matrices of resonant transmitters and receivers [163]–[166] are popular examples amid the developed solutions.

In this Chapter the interest is directed to the development of WPT techological solutions with a particular reference to biomedical applications; thus, the proposed designs are suited in terms of size and operative frequencies for the most common biomedical implants [142]. Nevertheless, the achieved results and developed concepts can be straightforwardly applied also in other industrial fields. In biomedical scenarios, resonant inductive WPT systems typically operate at very low working frequencies (i.e. few MHz). By operating in the quasi-magnetostatic regime, non-magnetic human tissues have minimal impact on the field strength and pattern, leading to reliable and predictable power transfer through the body. Moreover, operating in this regime minimizes undesired thermal energy deposition in the tissue (i.e. ohmic heating characterized by the Specific Absorption Rate) [37], making the technique one of the most convenient ways to deliver power to an implant without using wire connections.

In the following, we present two distinct solutions trying to improve the WPT characterizing parameters, i.e. working distance, efficiency and gain. In particular, we describe the design of an ultra-thin low frequency metasurface which is able to increase the performance of the inductive link, although being extremely compact [13], [14]; in addition, we propose an analytical formulation to design arrays of non resonant loops for tunable WPT devices, meaning that it is possible to finely control gain and efficiency in order to reach their best tradeoff for a given application [15].

3.2 A Compact Magnetically Dispersive Surface for Low Frequency Wireless Power Transfer Applications

A particularly active area of research is devoted to the integration of metamaterials and metasurfaces to enhance the performance of WPT systems [157], [158], [160], [167]–[172]. These engineered materials consist in either a 3D (metamaterial) or 2D (metasurface) array of subwavelength unit-cells that produce beneficial bulk electromagnetic properties (permittivity, permeability, conductivity) not found in nature [96]–[99], [173]–[175]. For example, several works have shown that a negative permeability can enhance magnetic evanescent waves [157], [171], [176], [177], thus increasing WPT efficiency.

In some cases, metasurfaces have an advantage over 3D bulky metamaterials, since their reduced thickness makes integration in WPT systems easier [178]. Among metasurfaces for inductive WPT, printed planar resonators and wires in different arrangements are very popular: it has been demonstrated that spiral resonators, split rings, in a single or double layer configuration are able to improve the efficiency of the inductive link [167], [168], [172], [179]–[183]. However, one common problem associated with printed metamaterials relies in the relatively large ohmic losses [184]. Amid other important technical limitations, the working frequency is often too high for the usual WPT applications [160], [167], [169], [171], [179], [180], [183], [185]. In addition, the dimension of the unit cell is typically too large to offer a practical solution [167], [169], [170], [172], [183], [185], [186]. To the best of our knowledge, the most compact lateral size for a WPT metamaterial unit cell measures 1/10000 of the applied wavelength [158]. However, the design consists of a 3D unit cell with a depth dimension of 2 cm, making difficult the integration of the metamaterial in a WPT system, especially considering the compact size of novel electronic devices.

In order to overcome these limitations, we propose an ultra-thin magnetically dispersive surface (i.e. a metasurface), exploiting a compact connected double-spiral unit cell. In addition, we plan to maintain a low operational frequency (MHz), as typical for inductive WPT systems. Finally, we aim to minimize the electric field produced by the transmitter, while maintaining the equivalent high level of magnetic field at the receiver (and thus, the efficiency). Such a feature can be extremely useful in all applications in which the exposure in

terms of Specific Absorption Rate (SAR) is a major concern, for instance in biomedical implants and rechargeable devices.

The work is organized as follows: first, we describe the unit cell and the metasurface design and electromagnetic characterization; next, we present the WPT set-up, chosen as test case, and we describe the advantages in using a metasurface in comparison with a traditional 3 coil system in terms of lower electric field production; after that, we report the efficiency results from numerical simulations and the comparison with experimental measurements obtained over a fabricated prototype. Finally, conclusions follow.

3.2.1 Metasurface design

As briefly described in the previous section, metamaterials and metasurfaces are composed of arrays of unit cells whose main feature is to be extremely small with respect to the wavelength at the operating frequency. This property causes the entire array to act as a homogenous material for impinging electromagnetic waves [96] (i.e. homogenization criterion); the large wavelength is not able to resolve the small structure of the slab; thus, it is possible to consider the array as a continuous medium.

The advantage in using such structures lies in the fact that it is therefore possible to design materials with exotic and non-conventional electromagnetic properties, not usually found in nature. These properties include: negative dielectric permittivity, negative magnetic permeability, and negative refractive index. Furthermore, it is possible to design the metamaterial to show one or a combination of the stated exotic properties in all three spatial dimensions or only in some privileged directions (i.e. anisotropy) [96]–[99], [173]–[175].

The basic properties of metamaterials and metasurfaces rely on the unit cell design. In fact, the characteristic electromagnetic behavior is due to the resonant nature of the unit cell [8]. In order to develop a metamaterial for inductive WPT applications, a highly inductive resonant unit cell - capable of fully satisfying the homogenization criterion (i.e., compact dimensions) and of operating at a very low frequency (i.e., few MHz) - is generally needed. Further, the unit cell must have a sufficiently high Q-factor (low ohmic losses) to enhance the response of the artificial material.

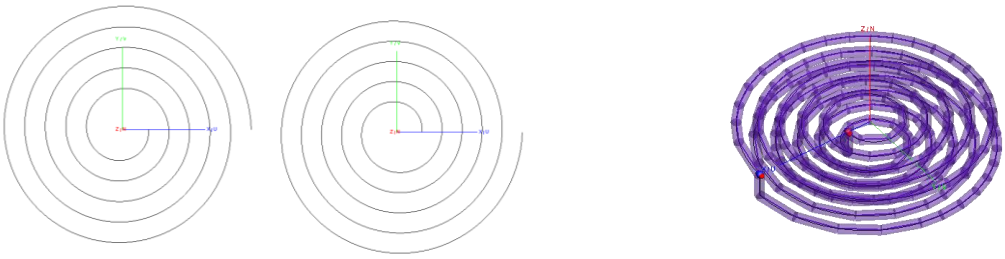

(a) (b)

Fig. 3.3. (a) Top views of the two separated spirals; the different orientation of the winding in the two cases (right and left handed, respectively) can be seen. (b) Picture of the complete unit cell: the two spirals form a single connected highly-inductive structure.

With these goals in mind, we propose a design consisting of two 5-turn spirals - one "left handed" and the other "right-handed" (Fig. 3.3(a)) - connected at both extremities [13]. In this way, a continuous structure is realized (Fig. 3.3(b)), through which the current flows in the same direction, thus enhancing the magnetic field.

The simulated unit cell (Feko Suite, Altair, Troy, MI, USA) was realized with a 26 AWG lossy copper wire. Each of the two spirals was 10 mm in diameter and was separated from the other by 1 mm. The designed unit cell has a total inductance of 397 nH and was made resonant at 5.16 MHz by adding a 2.4 nF capacitor. The capacitor was simulated adding a series resistance of 0.1 Ω, accounting for expected typical losses. The resulting Q-factor was 66.3, due to the moderate ohmic losses. The resonant frequency was chosen within the range typically employed for inductive WPT, especially for biomedical applications. Table 3.1 summarizes the unit-cell design parameters.

Table 3.1
Unit Cell Parameters

Parameter	*Value*
Outer diameter	10 mm
Inner diameter	2 mm
Copper Wire gauge	26 AWG
Inductance	397 nH
Added Capacitance	2.4 nF
Q-factor	66.3
Resonant frequency	5.16 MHz

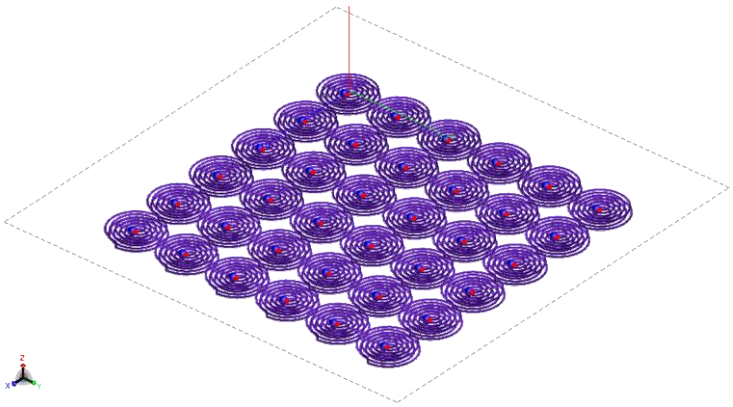

Fig. 3.4. Metamaterial CAD representation: 6 × 6 planar array of unit-cells.

From a theoretical point of view, an infinite array of unit cells should be realized in order to fully satisfy the ideal metasurface requirements. Clearly, such a slab is not physically realizable, and there are practical limitations to consider as well. First, the design must remain compact in order to employ the slab in practical applications; second, an increased number of unit cells results in increased ohmic losses. Thus, we realized a compact metasurface, choosing an array of 6 × 6 unit cells as a suitable compromise between magnetic field enhancement, compactness and low losses (Fig. 3.4). In particular, the array dimensions were chosen in the same order of the ones of the 3-coil system we aim to compare with. Obviously, other array sizes may be chosen for different applications to fit their designing specifications.

The extremely reduced thickness allows us to easily preserve the working distance between transmitter and receiver compared to the case without the slab, while significantly enhancing the WPT efficiency.

3.2.2 Electromagnetic characterization

In order to understand the physics of the interaction between the metasurface and the electromagnetic field and subsequently exploit that understanding to achieve high performance in WPT applications, a numerical electromagnetic characterization study of the proposed metasurface was performed. In the literature, the characterization of a 3D bulk metamaterial is a well-established topic: techniques exploiting reflection and transmission coefficients (or *S*-parameters as well) of a plane way impinging on a sample of the metamaterial have been commonly applied [188].

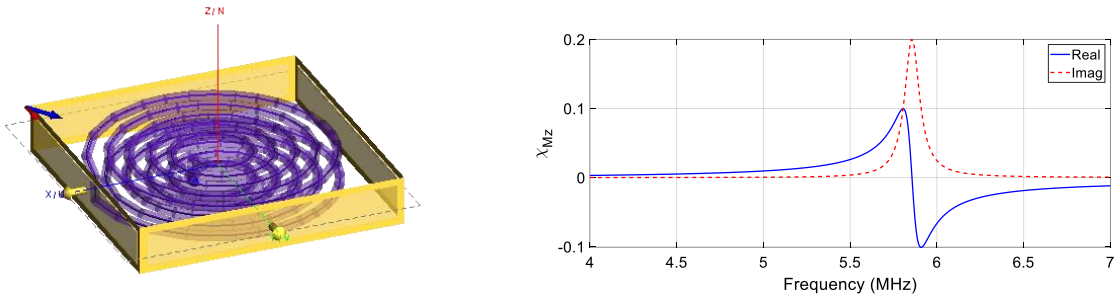

(a) (b)

Fig. 3.5. (a) Simulated metasurface with an impinging plane wave: reflection and transmission coefficients can be used to recover the surface susceptibilities [187]. (b) Computed magnetic surface susceptibility of the metasurface along its perpendicular axis (z-axis in (a)).

Owing to the fact that a metasurface cannot be correctly modeled as a slab of bulk material, it should be, in fact, more properly thought of as a planar array of scatterers of thickness in the extreme subwavelength region (i.e., a "single layer metamaterial"). Several works in literature have developed rigorous interpretations for a metasurface's electromagnetic behavior where the metasurface is interpreted as a thin impedance sheet [178], [184], [186], [187]. By exploiting boundary conditions for the electromagnetic field at the interfaces of the sheet, it is possible to define dielectric and magnetic surface susceptibilities, thus avoiding the extraction of fictitious bulk properties.

Hence, following the theory developed in [187], we characterized the properties of the slab in terms of surface susceptibilities. Specifically, we numerically simulated a planar array composed of the designed unit-cells by exploiting periodic boundary conditions; in this way, we considered an ideal infinite array, thus fulfilling the theoretical hypothesis for the extraction method. Then, we separately simulated TE and TM plane waves impinging on the slab at different angles, obtaining the reflection and transmission coefficients and, in turn, the surface susceptibilities, as described in [187] (Fig. 3.5(a)). As expected, given the geometrical properties of the unit cell, we found a significant surface susceptibility only for the magnetic field in the direction perpendicular to the slab.

Figure 3.5(b) suggests a useful physical and practical interpretation of the surface behavior. Specifically, we recognize a paramagnetic region before the resonance point, in which the real component of the magnetic susceptibility is positive. The consequence is that

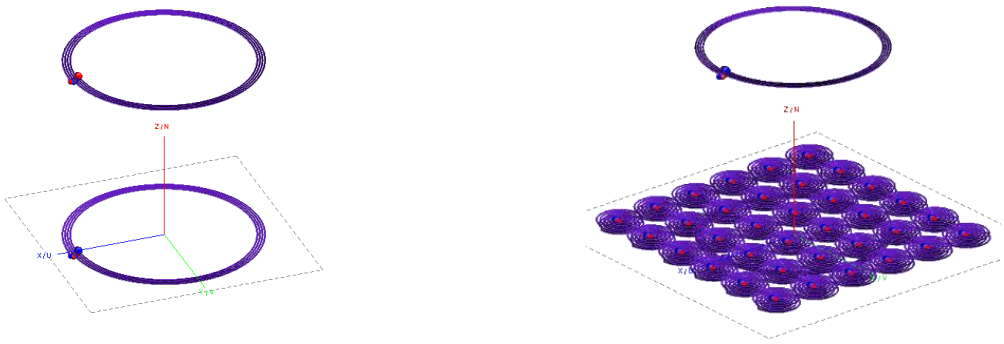

(a) (b)

Fig. 3.6. (a) CAD model of the adopted TX/RX system for inductive WPT experiment. (b) Isometric view of the complete system in presence of the metasurface. The designed slab is placed 1 mm above the transmitting coil.

the metasurface reacts to incident magnetic fields with a magnetization of the same direction, thus reinforcing the field itself. On the other hand, we can observe a diamagnetic region after the resonance, in which the metasurface magnetization is opposite to the impinging magnetic field. Finally, we have the resonance region where a sudden phase shift of the susceptibility is observed. Therefore, one of the optimal configurations for WPT applications is when the operation frequency corresponds to its magnetic resonance where we expect the maximum amplitude for currents, as it happens for traditional 3-coil systems. This explains the increase in efficiency due to the metasurface.

3.2.3 WPT Test Case

The proposed WPT test case consists in a fed driver coil mutually coupled with a passive receiver coil. The driver and the receiver coils were identical, 4-turn planar spirals with a 4 cm average diameter. Fig. 3.6(a) shows the 3D CAD model realized within the design environment of FEKO simulation software.

The spirals were designed with a 26 AWG lossy copper wire and were made resonant at 5.77 MHz. This corresponds to the resonant frequency of the metasurface shown in Fig. 3.5 (b), where WPT performance can be maximized. The driver was equipped with a 560-pF capacitor in series with a 5 Ω resistor that emulates the source resistance of a typical power amplifier for WPT applications [142]. The receiver was equipped with a 560-pF capacitor and a series resistive load of 43 Ω, representing the useful load at which the output power was

evaluated. The coil parameters are summarized in Table 3.2. Starting from this simple system, we then inserted the metasurface between the driver and the receiver, in order to enhance their mutual coupling (Fig. 3.6(b)), placing the slab as close as possible to the driver.

Table 3.2
Transmitter and Receiver Parameters

Parameter	*Transmitter*	*Receiver*
Outer diameter	42 mm	42 mm
Inner diameter	38 mm	38 mm
Copper Wire gauge	26 AWG	26 AWG
Inductance	1.36 µH	1.36 µH
Added Capacitance	560 pF	560 pF
Source impedance	5	N/A
Series Load	N/A	43 Ω

3.2.4 Comparison with a traditional 3-coil system

Here we compare the performance of our metasurface system with a traditional 3-coil system for WPT. In a 3-coil system, a single loop (i.e., transmitter), resonating at the same frequency as the driver and receiver, is placed in the same location as the metasurface. It is well-known that a 3-coil system can significantly improve the efficiency of the energy transfer between driver and receiver. Consequently, we explore how our metasurface behaves relative to a single coil resonator which shares the same external dimensions. However, as we demonstrate below, the proposed metasurface solution has some unique advantages beyond simple efficiency increase.

In order to realize the comparison, we used the same driver and receiver described in the previous section. Moreover, we designed a single resonant loop with a diameter equal to the characteristic dimension of the designed metasurface (i.e., 6 cm, see Fig. 3.7) to realize a typical 3-coil system.

A first comparison can be carried out by displaying the normalized H-field maps for the two configurations at a given distance from the transmitting side. For example, Fig. 3.8 shows the normalized H-field maps at a 16 mm distance from the transmitting side. As shown in the

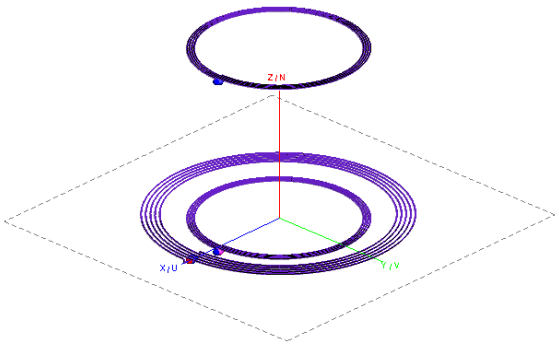

Fig. 3.7. CAD model of the 3-coil system used for comparison with the metasurface.

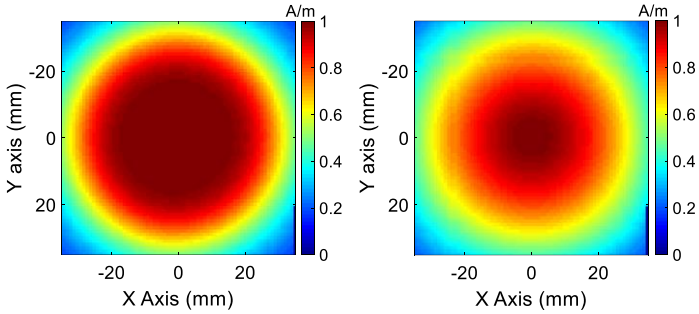

Fig. 3.8. Normalized H-field maps at 16 mm of distance from the transmitter: 3-coils system (left) and the metasurface (right). The focusing characteristics of the proposed metasurface are qualitatively noticeable.

figure, a metasurface with the same dimensions of the resonant element in the 3-coil system produces a more focused magnetic field. This is useful in biomedical devices because it reduces unwanted field exposure, and, in addition, enables a potential reduction of the implanted receiver dimension, since the field is concentrated in a smaller area.

Another major concern in the adoption of a particular WPT system arises from the electric field exposure. Indeed, whereas the biological tissue is non-magnetic (and, therefore, does not significantly affect the H-field), it is sensitive to energy deposition. Such exposure is typically measured in terms of Specific Absorption Rate (SAR, (W/g)) and international regulations (for instance, see [37]) define strict limits for SAR levels, both for clinical and commercial devices. In order to evaluate the E-field due to the proposed metasurface compared to the 3-coil system, we chose to compare the two cases when the magnetic field in the proximity of the receiver is equal. Equivalent H-field at the receiver means that the same current is being delivered to the load.

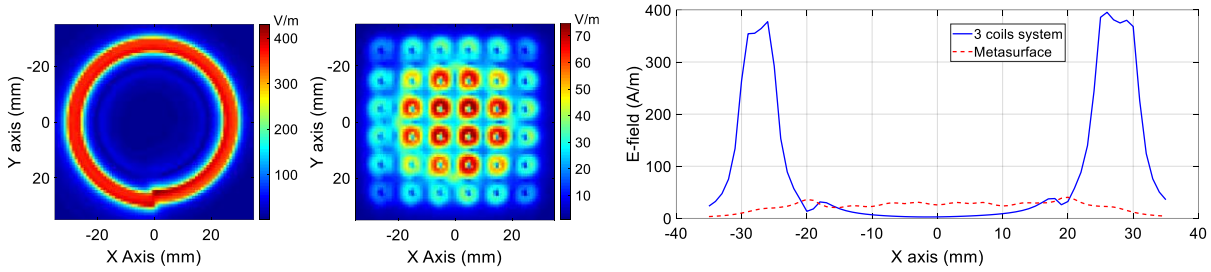

(a) (b)

Fig. 3.9. (a) E-field maps of the 3-coil system (left) and proposed metasurface (right). (b) E-field along X-axis (fixing Y coordinate) for both cases. E-field levels produced by the metasurface are drastically lower than the traditional 3-coil system.

Hence, the ratio E/H can be used as a metric in order to evaluate the relative safety of the two solutions.

As Fig. 3.9 shows, the metasurface configuration is able to produce a drastically lower E-field peak. This means that we can either have the same available current at the receiver load with lower exposure in terms of SAR; or, we can increase the amplitude of the magnetic field while maintaining the same exposure of a typical 3-coil system, thus increasing the amount of current flowing in the receiver.

We can conclude that the adoption of a metasurface can also offer the advantage of lower E-field peak, and therefore likely lower average SARs, with respect to traditional 3-coil systems.

3.2.5 Experimental efficiency results

Lastly, we experimentally evaluated the proposed metasurface in terms of efficiency enhancement for the WPT test-case previously described (Fig. 3.6). In general, the energy transferred by the driver generates a current in the receiver which flows into a useful resistive load (R_{load}) thanks to mutual coupling. In the hypothesis of a series load configuration, the equivalent circuit is shown in Fig. 3.2.

The circuital equivalence allows us to describe the system through a 2-port scheme:

$$\begin{cases} Z_{11_{eff}} I_1 + Z_{12_{eff}} I_2 = V_1 \\ Z_{21_{eff}} I_1 + Z_{22_{eff}} I_2 = V_2 \end{cases} \tag{3.3}$$

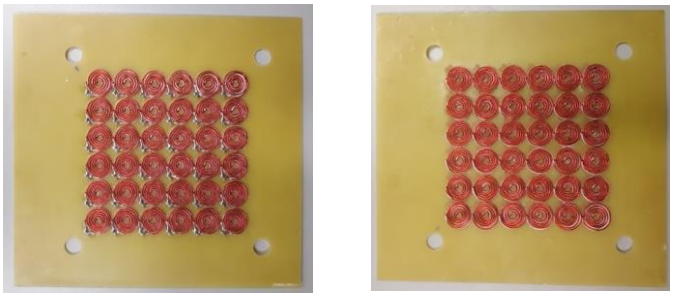

Fig. 3.10. Picture of the fabricated metamaterial slab; the single strand wires glued over the board maintains the ohmic losses low.

where the subscript 1 indicates the driving coil and the subscript 2 indicates the receiver. Regardless of the passive elements between driving and receiving coils (in our case, the metasurface, Fig. 3.6(b)), the previous model remains valid. Thus, it is possible to perform a 2-port measurement using a Vector Network Analyzer (VNA) in order to obtain the *Z* matrix of the system. The advantage of this approach is that it is possible to express the efficiency directly through the collected *Z*-parameters. Efficiency is typically described as the ratio between the output power dissipated in the useful load and the input power and can be related to *Z*-parameters as follows [142]:

$$\eta = \frac{|Z_{12_{eff}}|^2}{\Re\{Z_{11_{eff}}\}R_{load}} \tag{3.4}$$

We fabricated a prototype of the two simulated systems shown in Fig. 3.6 using AWG 26 single strand copper wires to realize both the metasurface and the spirals. This choice complicated the fabrication process compared to printed PCB technology but was necessary to minimize ohmic losses [128]. For all three components of the system (driver, receiver and metasurface), we utilized a 0.8 mm thick FR4 substrate over which we secured the copper wires (Fig. 3.10). We soldered surface-mount capacitors and resistors over the boards according to the numerical design parameters (Table 3.1 and 3.2), and we connected the transmitter and the receiver to a VNA (Keysight, E5080A ENA Vector Network Analyzer) using a 50-ohm micro SMA connector. Finally, each substrate slab was provided with 4 external holes, which allowed us to create a nylon support and positioning framework for the experimental setup.

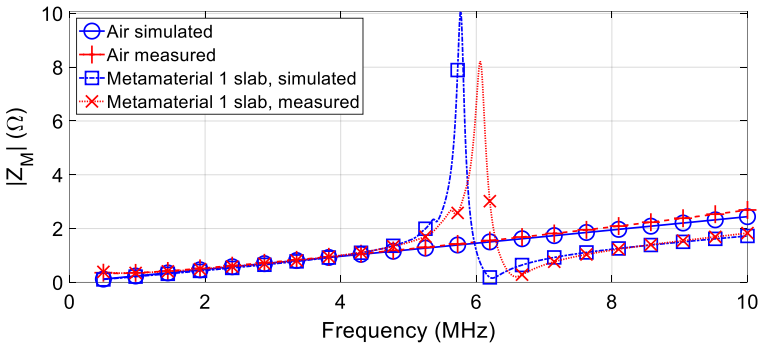

Fig. 3.11. Frequency behavior of the mutual impedance between transmitter and receiver coils; it can be seen the enhancement produced by the presence of the metasurface with respect to the "air" case.

From measurements, we confirmed that placing the metasurface as close as possible to the driving coil provides the maximum mutual coupling with the receiver (and, consequently, maximum efficiency). This choice also has the benefit of not significantly altering the working distance with respect to the simple 2-coil WPT system. Thus, we placed the metasurface slab 1 mm away from the driving coil and the receiving coil 40 mm away from the metasurface; then, we performed a preliminary study of the mutual coupling (i.e. Z_M) between driver and receiver over a certain frequency range. We also performed the same experiment in the absence of the metasurface for comparison purposes. In Fig. 3.11 we report the magnitude of Z_M obtained with the numerical simulations and measurements, for the two cases. It is important to note that the mutual coupling increase is entirely due to the presence of the metasurface; indeed, the magnitude of Z_M relative to the driver-receiver alone system is linear with frequency, as expected. The experimental results are in good agreement with the simulation, although we observe a slight shift in resonant frequency (5.77 MHz vs. 6.06 MHz). Such effect can be attributed to capacitor and manufacturing tolerances. The lower amplitude, on the other hand, is due to additional losses from the fabrication process (for instance, soldering).

We then compared the mutual coupling between the two cases, i.e. with and without metasurface, at the operational frequency. We increased step-by-step the working distance, taking care to maintain equal working distances in the two configurations (that is, taking into account the position and the thickness of the metasurface). As Fig. 3.12(a) shows, the metasurface always outperforms the mutual coupling values obtained using the simple driver-

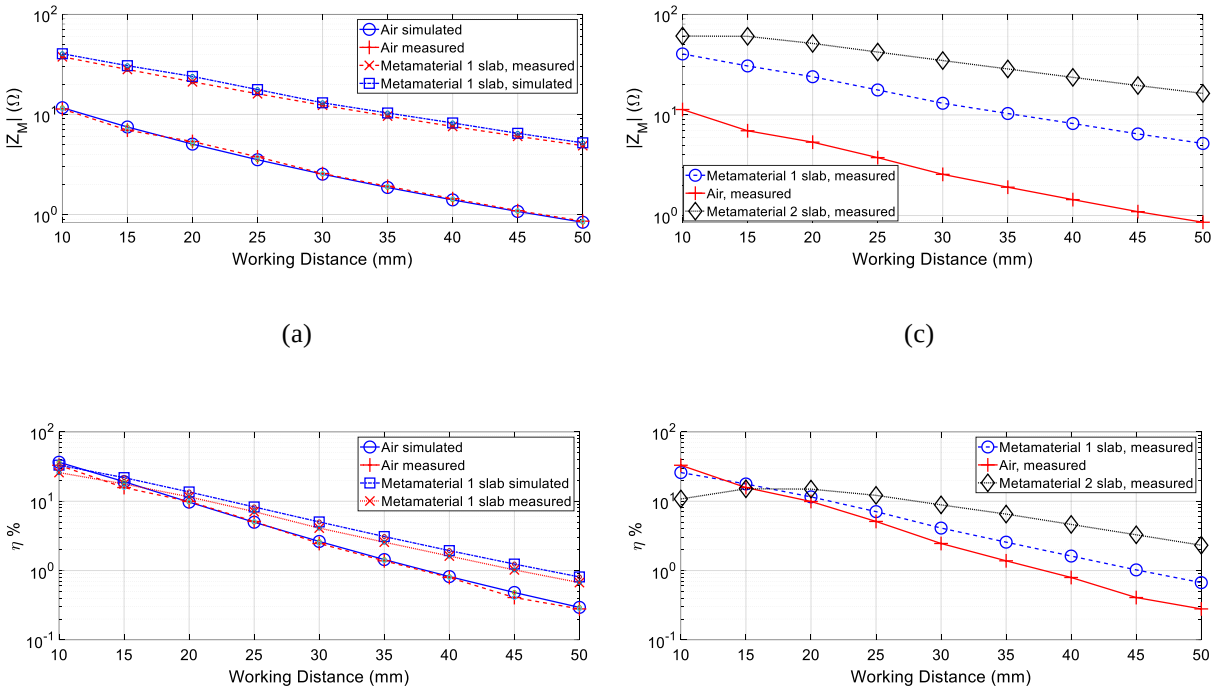

Fig. 3.12. Mutual coupling and efficiency comparison at increasing working distances for different configurations. (a) and (b) "Air" and single metamaterial slab (numerical simulations and measurements). (c) and (d) Comparison between three measured cases: "air", 1 metasurface at the transmitter, 2 metasurfaces (at the transmitter and at the receiver). It can be highlighted the performance increment due to the metasurface presence.

receiver system. Therefore, the metamaterial is effective in enhancing the magnetic field at the receiver, demonstrating the validity of the overall design.

Next, we compared the efficiency for the two cases for different working distances (again maintaining equal distance in the two configurations); Fig. 3.12(b) shows significant efficiency increase thanks to the metasurface. For instance, for a working distance of 25 mm, the efficiency increases from 5% to 7%, thus showing a 40% improvement.

The metasurface can also be used to increase the working distance. Fixing a target efficiency, we obtained a relevant increment for the working distance. In the absence of the metamaterial, the efficiency is 5% for a working distance of 25 mm; the same efficiency value

is achieved with the metamaterial slab for a working distance of 28 mm, thus producing a 12% enhancement.

However, for small working distances (less than 20 mm), the metasurface does not provide any advantage in terms of performance for the considered WPT system. Indeed, the presence of the metasurface also increases the reflected impedance at the transmitter and receiver ports. Thus, when both transmitter and receiver are close to the metasurface slab the overall efficiency of the system can decrease.

Considering the properties of the metasurface that we have highlighted in the electromagnetic characterization section, a natural extension of the adopted experimental set-up consisted in the use of an additional slab of metamaterial, placed close to the receiver. Thus, we realized a second slab identical to the previous metasurface, placing it 1 mm from the receiver. This configuration allows increasing the mutual coupling between the driver coil and the receiver coil and, consequently, the efficiency (Fig. 3.12(c) and 3.12(d)). The efficiency at a working distance of 25 mm is 12 %, resulting in a 140% improvement with respect to the air case. On the other hand, for a target efficiency of 5%, the working distance passes from 25 mm in air to 39 mm with the double slab (+ 56%).

3.2.6 Conclusions

In this work, we presented a novel design for a metasurface useful for efficiency improvement in low frequency inductive WPT applications. The extremely low thickness (1 mm) and compact lateral size (6 cm × 6 cm) are of significant benefit in many application areas, including rechargeable devices and biomedical implants. It was demonstrated that the metasurface, used at the magnetic resonance point, reinforces the current in the receiver and thus increasing the efficiency of the system. Moreover, it was proved that the metasurface produces lower electric field with respect to traditional 2/3-coil systems, thus representing the possibility of realizing safer WPT devices. Finally, we performed efficiency measurements over fabricated prototypes, showing that the metasurface, although extremely thin, is able to significantly increase the efficiency and working distance with respect to a 2-coil system.

Further development efforts can be undertaken to optimize the proposed design for a real-world scenario, for biomedical or industrial applications, taking special care to minimize

the ohmic losses and to improve the unit cell design. Overall, these promising results could open the way to new practical applications of metasurfaces in low frequency inductive WPT system, increasing the safety through the reduced E-field undesired exposure, and overcoming the main limit in the literature which rely on the excessive dimensions of the proposed unit-cells.

3.3 On the Design of Non-Resonant Coils Planar Arrays for Tunable Wireless Power Transfer Applications

Among the numerous and variegate WPT configurations appeared in literature, the 3-coil system is probably the most common, efficient and compact solution to enhance the performance of an inductive link. Instead of using only a driving loop inductively coupled with a receiver (both resonant at the same frequency), an additional intermediate resonant passive coil is introduced. This transmitting coil is strongly coupled with the driver coil (typically they are concentric and coplanar) and, in turn, it is also strongly coupled with the receiver. This configuration provides enhanced efficiency due to the high Q-factor of the transmitter, which, unlike the driver, is unaffected by the power amplifier source impedance [142], [166]. In this way, very small currents in the driver are sufficient to induce a considerable amount of current flowing in the transmitter.

Although 3-coil systems are excellent candidates for various WPT applications (biomedical, automotive, consumer), they suffer from an intrinsic limit: once the geometries of the various coils are established, the characteristic parameters of the inductive link (i.e. gain and efficiency) are uniquely determined. Therefore, there is no possibility for system tuning and no tradeoff can be accomplished between gain and efficiency, aspects that would be extremely useful in a variety of WPT applications. Indeed, such systems are frequently used for telemetry in combination with power delivery [143]–[148]. For these applications in particular, the potential to enhance gain at the expense of efficiency (or vice versa) will enable the design of highly optimized WPT devices.

To achieve this important feature, we propose a novel design procedure to realize WPT systems that generalizes the 3-coil system formulation and replaces the single resonant transmitting coil with a planar array consisting of an arbitrary number of non-resonating concentric loops. By loading each element of the array with a specific reactance value, it is possible to independently control the current amplitude flowing in each loop. Thus, we can exercise precise control over gain and efficiency, obtaining the best compromise for a given application. Moreover, through this design procedure, focused magnetic field distributions are also achievable, potentially allowing for reduced receiver dimensions.

In the following, we introduce first the theory behind the proposed design procedure; then, we describe the different array configurations chosen as test-cases for comparison with a specific 3-coil system; after that, the results from numerical simulations and from experimental measurements obtained with fabricated prototypes are shown. Finally, conclusions are derived.

3.3.1 Design procedure: theoretical formulation

Consider a generic system (shown in Fig. 3.13) consisting of a fed driver coil (element 1), N concentric loops that are coplanar with the driver (elements 2, 3,…, N+1), and a receiver (element N+2). Driver and receiver are resonant at the same frequency (the working frequency, ω_0). In a first approximation, with the purpose of simplifying mathematical expressions, we neglect ohmic losses for the N concentric loops. Assume that the currents flowing in each element of the concentric array (i.e., I_2, I_3,…, I_{N+1}) are in the following form:

$$I_i = c_i I, \qquad with \;\; i = 2,3,\dots,N+1 \tag{3.5}$$

where c_i is the generic i-th complex current coefficient. When the coefficients c_i have the same phase, all currents flowing in the array elements also share the same phase, each producing a magnetic field reinforcing with the others. This is the optimal condition for inductive wireless power transfer, leading to a strong magnetic field at the receiver, as Faraday's law suggests. However, by opportunely modulating amplitude and phase of these coefficients, creating arbitrary field distributions is also possible.

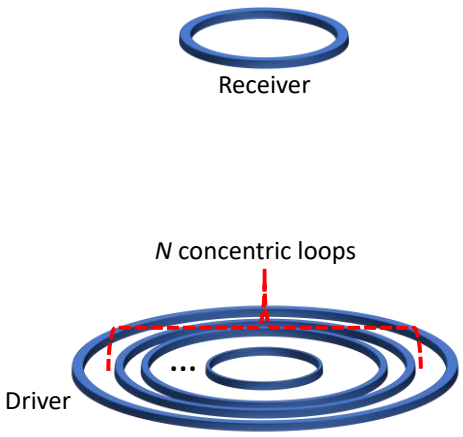

Fig. 3.13. Generic configuration forming the basis of the developed procedure.

At this point, considering that only the driver is actively fed, we can describe the entire structure in terms of its equivalent network model:

$$\begin{pmatrix} Z_{11} & Z_{12} & \dots & Z_{1(N+1)} & Z_{1(N+2)} \\ Z_{21} & Z_{22} & \dots & Z_{2(N+1)} & Z_{2(N+2)} \\ \vdots & \vdots & \vdots & \vdots & \vdots \\ Z_{(N+1)1} & Z_{(N+1)2} & \dots & Z_{(N+1)(N+1)} & Z_{(N+1)(N+2)} \\ Z_{(N+2)1} & Z_{(N+2)2} & \dots & Z_{(N+2)(N+1)} & Z_{(N+2)(N+2)} \end{pmatrix} \begin{pmatrix} I_1 \\ c_2 I \\ \vdots \\ c_{(N+1)} I \\ I_{(N+2)} \end{pmatrix} = \\ = \begin{pmatrix} V_1 \\ 0 \\ \vdots \\ 0 \\ 0 \end{pmatrix} \tag{3.6}$$

Next, we impose the following conditions at ω_0:

$$\begin{cases} (c_2 Z_{22} + c_3 Z_{23} + \dots + c_{(N+1)} Z_{2(N+1)}) I = 0 \\ (c_2 Z_{32} + c_3 Z_{33} + \dots + c_{(N+1)} Z_{3(N+1)}) I = 0 \\ \vdots \\ (c_2 Z_{(N+1)2} + c_3 Z_{(N+1)3} + \dots + c_{(N+1)} Z_{(N+1)(N+1)}) I = 0 \end{cases} \tag{3.7}$$

In the stated lossless hypothesis, it is possible to find the reactance of each of the concentric loops necessary to satisfy the conditions in (3.7):

$$Z_{ii} = \frac{-\sum_{j=2, j\neq i}^{N+1} c_j Z_{ij}}{c_i}, \qquad with \;\; i = 2,3,\dots,N+1 \tag{3.8}$$

As it can be seen from (3.8), the concentric loops are non-resonant at ω_0; they present, instead, a residual reactance given by the sum of the mutual impedances shared with the other loops and weighted by their respective current coefficients c_j.

Considering (3.7), we can sum the N equations of system (3.6) from row 2 to row (N+1), rearranging them into a new equivalent system of 3 equations:

$$\begin{pmatrix} Z_{11} & Z_{1x} & Z_{1(N+2)} \\ Z_{x1} & Z_{xx} & Z_{x(N+2)} \\ Z_{(N+2)1} & Z_{(N+2)x} & Z_{(N+2)(N+2)} \end{pmatrix} \begin{pmatrix} I_1 \\ I \\ I_{(N+2)} \end{pmatrix} = \begin{pmatrix} V_1 \\ 0 \\ 0 \end{pmatrix} \tag{3.9}$$

where we define the equivalent coupling coefficients between the driver and the array (Z_{1x}) and between the array and the receiver ($Z_{(N+2)x}$) and the equivalent self-impedance of the array (Z_{xx}, imposed in (3.7) as equal to zero at ω_0):

$$\begin{cases} Z_{xx} = \sum_{i=2}^{N+1} \sum_{j=2}^{N+1} c_j Z_{ij} \\ Z_{1x} = \sum_{j=2}^{N+1} c_j Z_{1j} \\ Z_{(N+2)x} = \sum_{j=2}^{N+1} c_j Z_{(N+2)j} \end{cases} \tag{3.10}$$

Note that (3.9) is the same system of equations that describes a generic 3-coil system, in which the transmitter is assumed lossless and resonant at ω_0 (transmitter is resonant with both driver and receiver). At this point, in our case, the transmitting coil has been replaced by the array of non-resonant concentric loops.

As typical for a generic 3-coil system, we can also hypothesize that [14]:

$$\begin{cases} Z_{1x} I \gg Z_{1(N+2)} I_{(N+2)} \\ Z_{(N+2)x} I \gg Z_{(N+2)1} I_1 \end{cases} \tag{3.11}$$

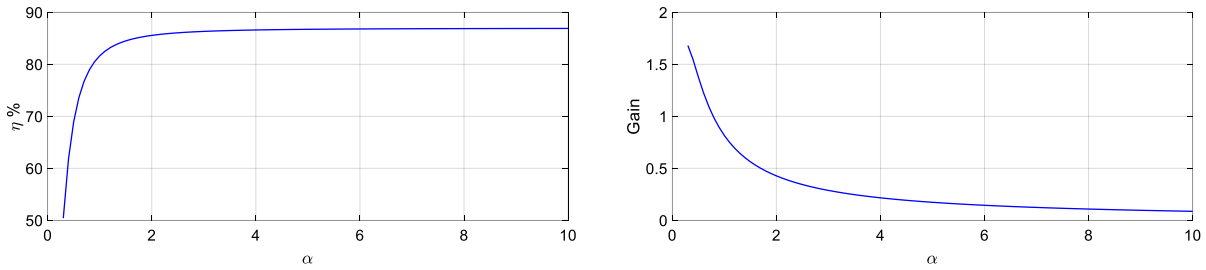

(a)

Fig. 3.14. Efficiency and Gain according to eq. (3.13) ((a) and (b), respectively); a compromise between the two parameters can be achieved by varying α.

i.e., the driver-receiver coupling can be neglected with respect to the driver-array and array-receiver couplings.

Also, as reported in the Introduction, gain and efficiency can be expressed in terms of input and output voltage amplitude and RMS (root mean square) power, respectively. Under hypothesis (3.11), solving system (3.9) leads to the following expressions for gain and efficiency:

$$\begin{cases} \eta = \left| \dfrac{R_{(N+2)}}{Z_{11}/\alpha^2 + Z_{(N+2)(N+2)}} \right| \\ Gain = \left| \dfrac{R_{(N+2)}\alpha}{Z_{11} + Z_{(N+2)(N+2)}\alpha^2} \right| \end{cases} \tag{3.12}$$

where the parameter α is defined as:

$$\alpha = \frac{Z_{1x}}{Z_{(N+2)x}} = \frac{\sum_{j=2}^{N+1} c_j Z_{1j}}{\sum_{j=2}^{N+1} c_j Z_{(N+2)j}} \tag{3.13}$$

Thus, by opportunely modifying the parameter α, we can reach the desired tradeoff between gain and efficiency. This can be carried out by independently weighting the currents flowing in each element of the array, through the coefficients c_j. To demonstrate this, Fig. 3.14 shows the qualitative trends of the gain and the efficiency versus α for a realistic combination of impedance values. Here we note that, in practical cases, α will almost certainly be greater than 1, since the elements of the array are coplanar with the driver and therefore present

significantly higher mutual coupling with the driver than the receiver (which is generally placed coaxially at a further distance).

In addition, by considering in more detail two implications of the typical geometric arrangement of driver, array, and receiver, we can establish a design framework for the dominant interactions that influence the value of α. First, the mutual coupling coefficients between each element of the array and the receiver do not present strong variations, due to the large distance between each "array element-receiver" pair. Indeed, the inductive coupling between two coils decreases with the cube of their distance. Thus, even if some inner array elements have a smaller area available for magnetic flux coupling, their respective coupling coefficients with the receiver will be only slightly lower in comparison with those of the outer elements. Second, the inner and outer array elements present mutual coefficients with the driver that can vary widely due to the shorter distances. Therefore, choosing higher current coefficients for the inner elements of the array leads to a lower α, because the parameter Z_{1x} increases slower than $Z_{(N+2)x}$, as eq. (3.13) shows. Conversely, α will increase with increased currents flowing in the outer elements.

Furthermore, since the parameter α can be defined for a traditional 3-coil system as the simple ratio of the mutual impedance between driver and transmitter and the mutual impedance between receiver and transmitter, the performance equivalency between a 3-coil system and an array configuration can be assessed by equating the parameter α in the two cases. The limit of a 3-coil system consists in the inability to tune gain and efficiency once the geometries are designed; therefore, the parameters of the inductive link are uniquely determined (i.e., no degrees of freedom are available to modify α). In this sense, the proposed array of concentric and coplanar non-resonating coils is a generalization of a traditional 3-coil system.

For completeness, we also report the efficiency and the gain when the ohmic losses in the array are not negligible:

$$\begin{cases} \eta = \left| \dfrac{R_{(N+2)}}{\left({Z_{11}\beta}/{\alpha^2} + Z_{(N+2)(N+2)} \right)\beta} \right| \\ Gain = \left| \dfrac{R_{(N+2)}\alpha}{Z_{11}\beta + Z_{(N+2)(N+2)}\alpha^2} \right| \end{cases} \tag{3.14}$$

where we define the loss factor β as:

$$\beta = 1 - \frac{Z_{(N+2)(N+2)}R_x}{Z^2_{(N+2)x}} \tag{3.15}$$

and R_x is equal to:

$$R_x = \sum_{i=2}^{N+1} c_i R_{ii}, \qquad with \;\; i = 2,3,\ldots,N+1 \tag{3.16}$$

with R_{ii} as the resistance of each element in the array.

In some practical conditions, the source voltage is fixed [142] (for instance, by power amplifier specifications). In such cases, to ensure maximum power transfer between the driver and the receiver, we must match the impedance seen by the driver itself. At resonance, the reflected impedance at the driver can be generically expressed as:

$$Z_{ref} = \frac{V_1}{I_1} = Z_{11}(1+\gamma) \tag{3.17}$$

To maximize the power transfer, γ should be equal to 1 (load impedance equal to source impedance). Once this requirement is satisfied, we achieve the best efficiency possible for the maximum power transfer condition. By using this formulation, the reflected impedance for the array case is described by:

$$Z_{ref} = Z_{11}\left(1 + \frac{Z_{(N+2)(N+2)}\alpha^2}{Z_{11}}\right) \tag{3.18}$$

From (3.18), we can assess that, by modulating the parameter α, it is possible to achieve the matching condition. Indeed, as proved in (3.13), we have at our disposal a consistent number of degrees of freedom to reach such goal as a result of the possible choices for the current coefficients c_i.

Finally, although the analytically-derived expressions for gain and efficiency rely on approximations, they are nonetheless extremely useful to provide physical insights and to aid in the design of an optimized WPT device.

3.3.2 Array configurations and 3-coil system: test-cases

With the purpose of experimentally verifying the theoretical model described in Section 3.3.1, we designed and fabricated a 3-coil system to be used as our reference standard and two different arrays of concentric non-resonant loops to be tested. The first array was initially implemented with the reactive loads necessary to demonstrate the equivalence with a 3-coil system, as theoretically predicted. Then, the reactive loads of the concentric loops were altered on that same array to demonstrate tuning of gain and efficiency (i.e. that the same array geometry can confer flexibility to the WPT performance). Finally, a second array was developed to show that an appropriate design can produce efficiency and gain levels comparable to a 3-coil system while achieving a more focused magnetic field distribution. Such a feature could be extremely useful for biomedical implants, potentially leading to a reduction of the implanted receiver size and to a lower electromagnetic (EM) field induced in tissue. All the proposed systems shared the same overall geometrical dimensions and constraints with the reference 3-coil system. The designs of the various experimental layouts required for the verification of the developed theory were performed using FEKO, a method of moments solver package (Feko Suite, Altair, Troy, MI, USA).

As a first step, we designed the 3-coil system which would serve as the reference standard to compare with all of the proposed arrays' performance. Inspired by [142], we implemented a 3-coil system consisting of an external 2-turn planar spiral driver, a coplanar and concentric 10-turn planar spiral transmitting coil, and a coaxial 8-turn planar spiral receiver (Fig. 3.15).

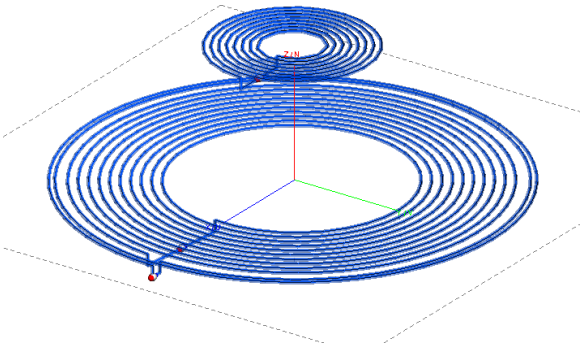

Fig. 3.15. 3D CAD model of the 3-coils system used as a reference standard for comparison against the various array configurations.

The driver had an external diameter of 40 mm, while the internal diameter of the transmitter was 18 mm. The receiving loop had an external diameter of 15 mm and an internal diameter of 5 mm; it was separated from the transmitting plane (i.e., along *z*-axis) by 15 mm. All coils were made with a 28 AWG single strand lossy copper wire and are resonant at the same frequency of 5.14 MHz through appropriate capacitive loads. The resonant frequency was chosen in the typical range for the most common WPT applications. A 200 Ω resistive load, at which the efficiency is evaluated, was placed in parallel with the receiver. In addition, we added a 5 Ω resistor in series with the driver in order to emulate the source impedance of a typical power amplifier [142]. The design features of the system are summarized in Table 3.3. Finally, we numerically estimated the α parameter, resulting in a value of 5.0.

Table 3.3
3-coil System Parameters

Parameter	*Driver*	*Transmitter*	*Receiver*
Outer diameter	40 mm	38 mm	15 mm
Inner diameter	38 mm	18 mm	5 mm
Number of Turns	2	10	8
Copper Wire gauge	28 AWG	28 AWG	28 AWG
Added Capacitance	2.25 nF	253 pF	1.5 nF
Source impedance	5 Ω	N/A	N/A
Resistive load	N/A	N/A	200 Ω
Resonant frequency	5.14 MHz	5.14 MHz	5.14 MHz

We then carried out the design of the array configurations, whose specifications are summarized below.

1) Experiment 1: the first experiment addressed the potential to design an array of non-resonating concentric loops equivalent to the standard 3-coil system. Thus, to ensure a fair comparison, the same driver and the receiver coils were used in both systems, only replacing the transmitter with an array of 3 concentric non-resonant loops, coplanar with the driver (Fig. 3.16). In addition, we maintained not only the external but also the internal diameter between the 3-coil system's transmitter and the array. In Table 3.4, we report the geometrical properties and the reactive loads of the array elements, determined by the procedure in Section 3.3.1. We selected the geometries of the array elements with the purpose of matching the α parameter of

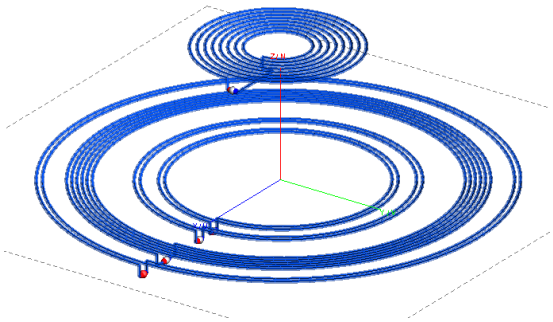

Fig. 3.16. Experiment 1: 3D CAD model of the array of concentric loops designed to be equivalent to the adopted 3-coil system.

the 3-coil system, while adopting current coefficients (c_1, c_2, c_3) all equal to 1 (same current amplitude expected in each element of the array). Using FEKO, we estimated the α parameter as 4.94, extremely close to that of the adopted 3-coil system.

Table 3.4
3-coil System Equivalent Array Parameters: Experiment 1 (Experiment 2)

Element #	*Outer Diam. (mm)*	*Inner Diam. (mm)*	*C(nF)*	*AWG*	*N_t turns*
1	35	30	0.336 (0.227)	28	6
2	24	22	1.7 (2.39)	28	2
3	20	18	2.28 (3.43)	28	2

2) Experiment 2: in this experiment, we set out to demonstrate that the above equivalent array to the 3-coil system could be easily modified to tune gain and efficiency. This can be achieved in a straightforward manner by selecting a different set of loads (and, consequently, currents) in each element of the array. In this way, we aimed to demonstrate the flexibility of the array configuration with respect to the 3-coil system.

With the purpose of enhancing the gain at the expense of the efficiency, a lower α parameter is required with respect to Experiment 1 (as Fig. 3.14 (a) and (b) show). Following the criterion described in Section 3.3.1, we chose the current coefficients (c_1, c_2, c_3) as (1, 4, 5), obtaining α equal to 3.54 (previously, 4.94), as desired, while retaining all of the geometrical properties of the array in Experiment 1.

3) Experiment 3: the last experiment was conceived with the aim of proving that an array configuration can represent a viable solution to create a focused magnetic field distribution, while preserving high levels of efficiency and gain with respect to a 3-coil system with identical dimensions. We can achieve such result by opportunely designing the array (Fig. 3.17); thus, we maintained the same receiver of the previous experiments, but we modified slightly the driver (always conserving the external dimensions of the original 3-coil system depicted in Fig. 3.15). We added a turn to the driver with the purpose to enhance the coupling with the array elements that were designed, differently from the other two examples, with smaller diameters. This was necessary to obtain a focused magnetic field distribution. As in the previous cases, the driver was equipped with a 5 Ω resistor, considering the source impedance of a power amplifier. Driver and receiver were again made resonant at 5.14 MHz, and the array was constituted by 3 concentric and coplanar non-resonant loops. By choosing the current coefficients (c_1, c_2, c_3) as (1, 1, 1), the estimated α parameter was 4.3. Therefore, as Fig. 3.14 (a) and (b) suggest, the performance in terms of gain and efficiency are expected to be a compromise between the two previous cases, i.e. preservation of both efficiency and gain levels. Table 3.5 reports the geometrical properties of this design and the adopted reactive loads.

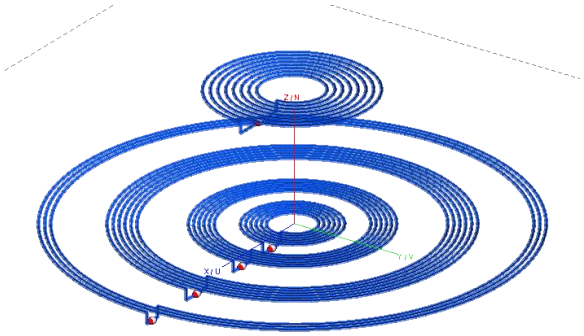

Fig. 3.17. 3D CAD model of the array of concentric loops designed to realize a focused magnetic field distribution.

Table 3.5
Focusing Array Parameters: Experiment 3

Element #	*Outer Diameter (mm)*	*Inner Diameter (mm)*	*C(nF)*	*AWG*	N_t
Driver	40	37	1.05	28	3
1	30.4	24.6	0.442	28	6
2	17.2	12.2	0.751	28	6
3	8.8	3.8	2.34	28	6

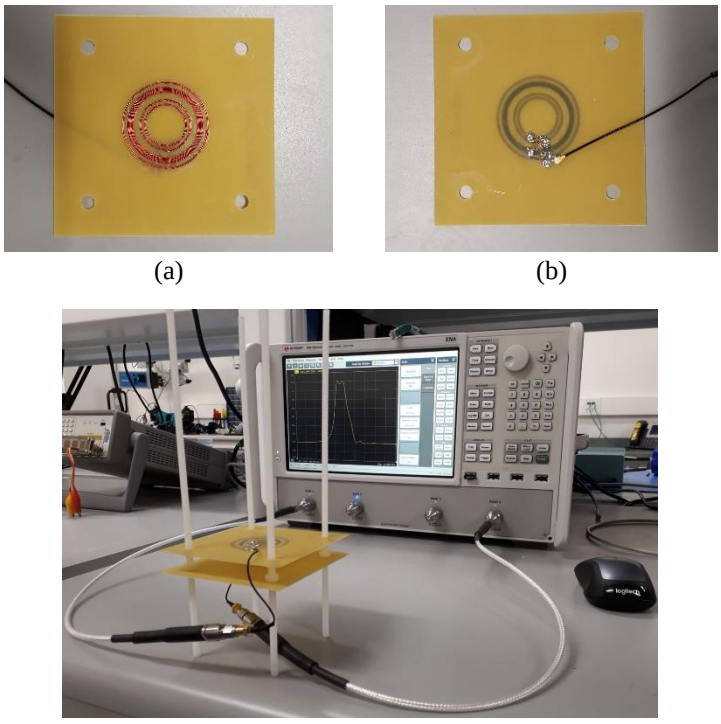

(a) (b)

(c)

Fig. 3.18. Array prototype relative to Experiment 1. (a) Upper view: the various coils were realized by gluing 28 AWG wire onto FR4 boards; (b) Bottom view: surface-mounted components soldered onto the board. (c) Fabricated system: the plastic frame guarantees a solid support, vertically tunable thanks to threaded nylon nuts.

Finally, after the numerical designs, we fabricated prototypes for each experimental configuration. We chose 0.8 mm thick FR4 slabs (ε_r = 4.3, $tan\delta$ = 0.025) as supporting substrates, and we glued a 28 AWG single strand copper wire over each board. While this solution complicates the fabrication process in comparison with printed coils, it has the advantage of low ohmic losses [128]. Then, on the other side of the board, we soldered surface-mounted components as specified by the numerical design procedure. We equipped each driving coil with a 50-Ω micro-SMA connector to enable measurements with a vector

network analyzer (Keysight E5080A). Fig. 3.18 shows one of the fabricated configurations as an example. Finally, we realized 4 external holes in each FR4 slab to mount the boards in a nylon support for performing controlled experiments, where, as Fig. 3.18(c) shows, we can precisely tune the position of both boards through threaded nuts.

3.3.3 Experimental Results

We performed efficiency and gain measurements (as described in [142], [158]) over the 3 different experimental configurations, both numerically and experimentally, comparing the results with the 3-coil system.

1) Experiment 1: this configuration explored the capability of an array of non-resonating concentric loops to perform equally as a 3-coil system sharing the same geometrical dimensions. As Fig. 3.19(a)-(b) shows, both the efficiency and the gain are in excellent agreement between the two cases, as predicted, demonstrating the validity of the developed theory.

2) Experiment 2: in this configuration, we exploit the same array of Experiment 1 with different reactive loads to increase the gain at some expense to the efficiency. In Fig. 3.19(c)-(d), we report the results of simulations and measurements performed on fabricated prototypes, showing that we obtained an efficiency about 10% lower with respect to the 3-coil system, but the maximum of the gain increased from 1.32 to 1.66, a 26% improvement. This result confirms the flexibility of our proposed method: the desired compromise between gain and efficiency can be achieved, tailoring the WPT device to the requirements of a specific application.

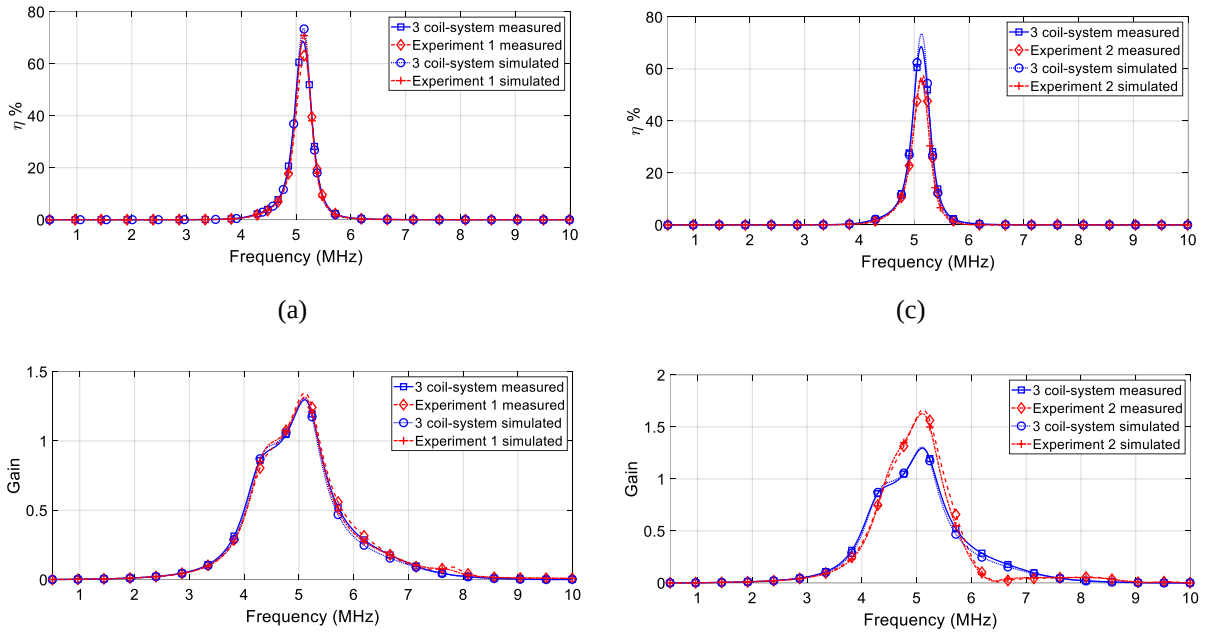

Fig. 3.19. Efficiency comparisons (measured and simulated) between 3-coil system and array (upper row). Gain comparisons (measured and simulated) between 3-coil system and array (bottow row). (a)-(b) (Experiment 1) The performance equivalency between the array and the 3-coil system can be highlighted. (c)-(d) (Experiment 2) The higher gain obtained with the same array of Experiment 1 (at the expense of the efficiency) can be pointed out.

3) Experiment 3: here we verify the potential to achieve a focused magnetic field distribution, while maintaining efficiency and gain. First, we performed numerical simulations of the magnetic field distributions for the array and the 3-coil system. We chose a plane 7 mm away from the transmitting side and we compared the two field maps (Fig. 3.20 (a)). It is evident that the array configuration produces a significantly more focused magnetic field compared to the 3-coil system, while, as shown in Figure 3.20 (b)-(c), maintaining high levels of efficiency and gain. Since the field is concentrated in a smaller area, this offers the potential for reduced receiver size. Moreover, this leads to a lower EM exposure of biological tissue. Such achievements are especially useful in biomedical implants, where reducing the size of the implanted receiver and the EM exposure can bring important advantages in terms of patient safety and comfort.

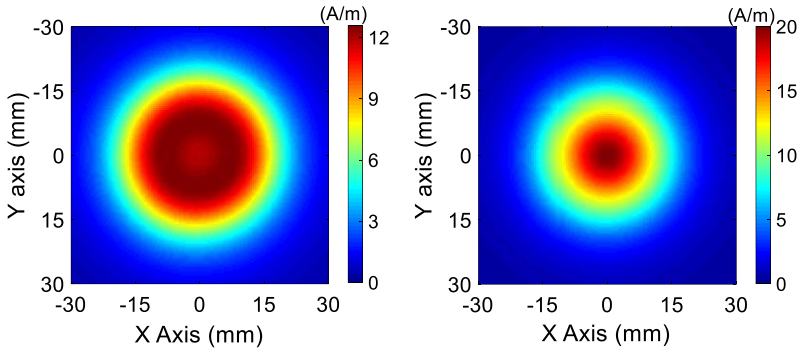

(a)

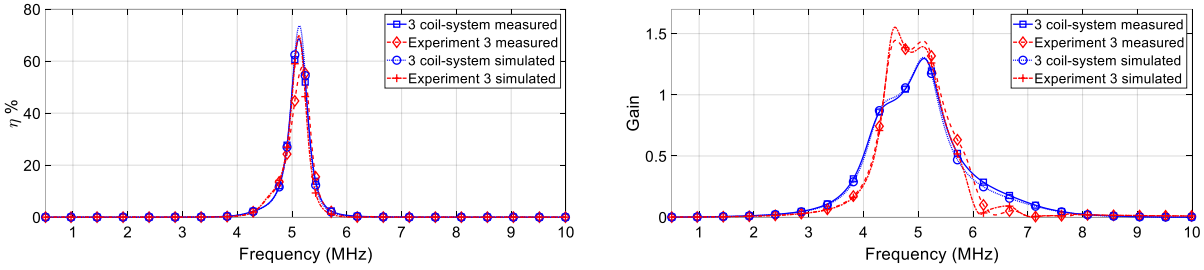

(b) (c)

Fig. 3.20. (Experiment 3) (a) Magnetic field maps in the plane 7 mm away from the transmitting side: 3-coil system (left); array (right): it is worth highlighting the focusing properties of the array configuration. Efficiency (b) and Gain (c) comparison between 3-coil system and array (measured and simulated): it can be noticed that the array is able to maintain excellent levels of efficiency and gain despite the magnetic field focusing property.

Finally, some overall observations can be made from all three cases. As Table 3.6 reports, the normalized currents in each element of the different arrays chosen during the design procedure (as described in Section 3.3.2) matched the simulation results. However, between numerical simulations and prototypes, a slightly efficiency reduction was generally observed, likely due to fabrication defects and additional soldering and connection losses.

Table 3.6
Normalized current amplitudes in the different array elements for the adopted configurations: numerically simulated (design requisites)

	Element #1	*Element #2*	*Element #3*
Experiment 1	1 (1)	0.996 (1)	0.998 (1)
Experiment 2	1 (1)	3.925 (4)	4.891 (5)
Experiment 3	1 (1)	0.996 (1)	0.989 (1)

3.3.4 Conclusions

In this work we presented a novel design and design procedure for a planar array of non-resonant coils, useful for flexible wireless power transfer applications. By employing this procedure, an optimal tradeoff between the characteristic parameters of an inductive link (gain and efficiency) can be achieved, finely controlling the current amplitude flowing in each element of the array through an appropriate reactive load. To verify the developed theoretical model, we designed, simulated, fabricated and experimentally tested three different array configurations to compare with a reference 3-coil system, achieving excellent agreement with the simulations. These results demonstrate that the designed array can perform equally to a 3-coil system sharing the same dimension, while also offering the possibility to balance between gain and efficiency for a given WPT application. Finally, arrays producing a highly focused magnetic field distribution can be realized, while retaining high levels of gain and efficiency.

Such properties can be extremely useful in many WPT applications. Indeed, the fine tuning between gain and efficiency can lead to highly optimized devices; for instance, with a low voltage power supply, choosing the best compromise between a high gain and a reasonable efficiency level is crucial. On the other hand, focused magnetic field distributions able to maintain high levels of both gain and efficiency are strongly promising for smaller implanted biomedical devices.

The results herein presented are general and can be specialized to different applications of WPT: further developments will be directed to apply the developed theory to practical cases and to improve the design process to achieve the best compromise possible for a given structure. For instance, by opportunely shaping the magnetic field distribution, the misalignment robustness could also be efficiently faced.

4 CONCLUSIONS

In this thesis, different radiofrequency magnetic field applications for biomedical purposes have been introduced.

We first proposed a general analytical approach to determine the electromagnetic properties of colloidal magnetic fluids with nanoparticles, useful in Magnetic Particle Hyperthermia. The electromagnetic characterization is fundamental to predict the behavior of the nanoparticles at different radiation settings and to find out the best heating condition. The developed analytical method exploits simple measurements of the nanoparticles heat release when exposed to an RF magnetic field; this approach can be a rapid and alternative procedure compared to the direct magnetic permeability measurement.

After that, we presented a low frequency focusing RF radiating system for MPH superficial treatments; we demonstrated that it is possible to realize RF coils able to sharply focus the RF magnetic field despite the huge wavelength of the radiation used in MPH (around hundreds of kHz). This result simplifies the instrumentation and reduces the RF exposure of healthy tissues compared with the actual technology which consists in a combination of DC and RF fields in order to confine the heat release from nanoparticles.

Afterwards, the mutual coupling issue in RF MRI coils has been faced, exploiting spiral resonators as decoupling elements. In order to exercise a full control over SRs interactions with MRI coils, we firstly developed an accurate method to extract the equivalent lumped RLC circuit describing the single resonator. The obtained results were in stark contrast with the most popular analytical model presented in the literature, especially regarding the inductance behavior versus the number of turns of the resonators. The proposed method restores the physical behavior for the inductance of a spiral, which increases with the number of turns.

Then, we developed a reliable analytical framework to individuate the optimum geometry, number and position of SRs to decouple MRI coils. We tested the method on a Double Tuned configuration (^{1}H - ^{23}Na), obtaining excellent results both in simulations and with fabricated prototypes. The possibility to print directly the resonators on the same dielectric substrate of the MRI coils results in the absence of physical connections, thus providing a mechanically

robust experimental set-up, and improving the transceiver design with respect to other traditional decoupling techniques.

Finally, we proposed two distinct solutions to increase performance in resonant inductive Wireless Power Transfer. The first proposal consisted in an ultra-thin low frequency dispersive surface (i.e., a metasurface); to the best of our knowledge, this surface is the most compact among the various similar solutions proposed in the literature, considering the low operative frequency (5.76 MHz). Neverthless, we proved both with numerical simulations and fabricated prototype that the metasurface is able to significantly increase the efficiency or, equivalently, the working distance of a generic inductive link.

In addition, a design procedure for concentric array of non-resonant loops for tunable WPT was described. This solution can be considered as an extension of the common 3-coil system, enabling the fine tuning between gain and efficiency. This property can be extremely useful in all the WPT applications requiring a compromise between the two properties, especially when also telemetry is performed together with energy transfer. Moreover, arrays can be designed to create focused magnetic field distributions retaining, at the same time, excellent efficiency and gain levels.

REFERENCES

[1] C. Byrne, "A Brief History of Electromagnetism," *Lowell Univ. Mass.*, 2015.

[2] P. Malmivuo, J. Malmivuo, and R. Plonsey, *Bioelectromagnetism: principles and applications of bioelectric and biomagnetic fields*. Oxford University Press, USA, 1995.

[3] V. Manoilov and G. Kittel, *Electricity and man: medical application and hazards*. 1978.

[4] C. Gabriel, S. Gabriel, and y E. Corthout, "The dielectric properties of biological tissues: I. Literature survey," *Phys. Med. Biol.*, vol. 41, no. 11, p. 2231, 1996.

[5] D. Brizi *et al.*, "A Novel Approach for Determining the Electromagnetic Properties of a Colloidal Fluid With Magnetic Nanoparticles for Hyperthermia Applications," *IEEE J. Electromagn. RF Microw. Med. Biol.*, vol. 2, no. 1, pp. 70–77, Mar. 2018.

[6] D. Brizi, A. Monorchio, and N. Fontana, "A novel coil for highly focused magnetic hyperthermia with nanoparticles," in *2017 IEEE International Symposium on Antennas and Propagation & USNC/URSI National Radio Science Meeting*, San Diego, CA, 2017, pp. 1223-1224, doi: 10.1109/APUSNCURSINRSM.2017.8072654.

[7] D. Brizi *et al.*, "A Radiating System for Low Frequency Highly Focused Hyperthermia with Magnetic Nanoparticles," *IEEE J. Electromagn. RF Microw. Med. Biol.*, doi: 10.1109/JERM.2019.2945833.

[8] D. Brizi, N. Fontana, F. Costa, and A. Monorchio, "Accurate Extraction of Equivalent Circuit Parameters of Spiral Resonators for the Design of Metamaterials," *IEEE Trans. Microw. Theory Tech.*, vol. 67, no. 2, pp. 626–633, Feb. 2019.

[9] N. Fontana *et al.*, "Decoupling of dual-tuned MRI coils by using distributed magnetic traps," *12th Eur. Conf. Antennas Propag. EuCAP 2018*, London, 2018, pp. 1-5, doi: 10.1049/cp.2018.0498 2018.

[10] D. Brizi, N. Fontana, F. Costa, G. Tiberi, and A. Monorchio, "On the Optimization of Distributed Magnetic Traps in MRI Coils Decoupling," in *2018 IEEE International Symposium on Antennas and Propagation & USNC/URSI National Radio Science Meeting*, Boston, MA, 2018, pp. 893-894, doi: 10.1109/APUSNCURSINRSM.2018.8608439.

[11] N. Fontana, D. Brizi, F. Costa, G. Tiberi, and A. Monorchio, "On the Decoupling Robustness of Distributed Magnetic Traps in Biological Loaded Dual Tuned MR coils," in *2019 IEEE International Symposium on Antennas and Propagation & USNC/URSI National Radio Science Meeting*, Atlanta, GA, USA, 2019, pp. 759-760, doi: 10.1109/APUSNCURSINRSM.2019.8889180.

[12] D. Brizi *et al.*, "Design of Distributed Spiral Resonators for the Decoupling of MRI Double-Tuned RF Coils," *IEEE Trans. Biomed. Eng.*, doi: 10.1109/TBME.2020.2971843 .

[13] D. Brizi, A. Monorchio, and G. Lazzi, "An Ultra-thin Low-frequency Metamaterial for Wireless Power Transfer Applications," in *2018 IEEE International Symposium on Antennas and Propagation & USNC/URSI National Radio Science Meeting*, Boston, MA, 2018, pp. 2555-2556.

[14] D. Brizi, J. Stang, A. Monorchio, and G. Lazzi, "A Compact Magnetically Dispersive Surface for Low Frequency Wireless Power Transfer Applications," *IEEE Trans. Antennas Propag.*, vol. 68, no. 3, pp. 1887-1895, March 2020, doi: 10.1109/TAP.2020.2967320.

[15] D. Brizi, J. Stang, A. Monorchio, and G. Lazzi, "On the Design of Non-Resonant Coils Planar Arrays for Tunable Wireless Power Transfer Applications," *IEEE Trans. Microw. Theory Tech.*, doi: 10.1109/TMTT.2020.2983145.

[16] G. Bellizzi and O. M. Bucci, "Magnetic Nanoparticle Hyperthermia," in *Emerging Electromagnetic Technologies for Brain Diseases Diagnostics, Monitoring and Therapy*, L. Crocco, I. Karanasiou, M. L. James, and R. C. Conceição, Eds. Cham: Springer International Publishing, 2018, pp. 129–191.

[17] A. P. Khandhar, R. M. Ferguson, and K. M. Krishnan, "Monodispersed magnetite nanoparticles optimized for magnetic fluid hyperthermia: Implications in biological systems," *J. Appl. Phys.*, vol. 109, no. 7, p. 07B310, 2011.

[18] S. Dutz and R. Hergt, "Magnetic particle hyperthermia—a promising tumour therapy?," *Nanotechnology*, vol. 25, no. 45, p. 452001, Nov. 2014.

[19] K. M. Krishnan, "Biomedical Nanomagnetics: A Spin Through Possibilities in Imaging, Diagnostics, and Therapy," *IEEE Trans. Magn.*, vol. 46, no. 7, pp. 2523–2558, Jul. 2010.

[20] V. M. Kulkarni, D. Bodas, D. Dhoble, V. Ghormade, and K. Paknikar, “Radio-frequency triggered heating and drug release using doxorubicin-loaded LSMO nanoparticles for bimodal treatment of breast cancer,” *Colloids Surf. B Biointerfaces*, vol. 145, pp. 878–890, Sep. 2016.

[21] J. Fock, M. Parmvi, M. Strömberg, P. Svedlindh, M. Donolato, and M. F. Hansen, “Comparison of optomagnetic and AC susceptibility readouts in a magnetic nanoparticle agglutination assay for detection of C-reactive protein,” *Biosens. Bioelectron.*, vol. 88, pp. 94–100, Feb. 2017.

[22] Seongtae Bae, Sang Won Lee, A. Hirukawa, Y. Takemura, Youn Haeng Jo, and Sang Geun Lee, “AC Magnetic-Field-Induced Heating and Physical Properties of Ferrite Nanoparticles for a Hyperthermia Agent in Medicine,” *IEEE Trans. Nanotechnol.*, vol. 8, no. 1, pp. 86–94, Jan. 2009.

[23] A. Matsumine *et al.*, “A novel hyperthermia treatment for bone metastases using magnetic materials,” *Int. J. Clin. Oncol.*, vol. 16, no. 2, pp. 101–108, Apr. 2011.

[24] K. Maier-Hauff *et al.*, “Intracranial Thermotherapy using Magnetic Nanoparticles Combined with External Beam Radiotherapy: Results of a Feasibility Study on Patients with Glioblastoma Multiforme,” *J. Neurooncol.*, vol. 81, no. 1, pp. 53–60, Jan. 2007.

[25] P. Wust *et al.*, “Magnetic nanoparticles for interstitial thermotherapy – feasibility, tolerance and achieved temperatures,” *Int. J. Hyperthermia*, vol. 22, no. 8, pp. 673–685, Jan. 2006.

[26] M. Johannsen *et al.*, “Thermotherapy of Prostate Cancer Using Magnetic Nanoparticles: Feasibility, Imaging, and Three-Dimensional Temperature Distribution,” *Eur. Urol.*, vol. 52, no. 6, pp. 1653–1662, Dec. 2007.

[27] S. L. Ho, S. Niu, and W. N. Fu, “Design and Analysis of Novel Focused Hyperthermia Devices,” *IEEE Trans. Magn.*, vol. 48, no. 11, pp. 3254–3257, Nov. 2012.

[28] P. C. Fannin, L. Cohen-Tannoudji, E. Bertrand, A. T. Giannitsis, C. Mac Oireachtaigh, and J. Bibette, “Investigation of the complex susceptibility of magnetic beads containing maghemite nanoparticles,” *J. Magn. Magn. Mater.*, vol. 303, no. 1, pp. 147–152, Aug. 2006.

[29] O. E. Ayala-Valenzuela, J. A. Matutes-Aquino, R. Betancourt-Galindo, and O. Rodriguez-Fernandez, “Complex magnetic susceptibility measurement of a magnetic fluid magnetite based,” *Int. J. Mater. Prod. Technol.*, vol. 27, no. 1–2, pp. 110–115, 2006.

[30] I. Hrianca and I. Malaescu, “The rf magnetic permeability of statically magnetized ferrofluids,” *J. Magn. Magn. Mater.*, vol. 150, no. 1, pp. 131–136, 1995.

[31] R. E. Rosensweig, “Heating magnetic fluid with alternating magnetic field,” *J. Magn. Magn. Mater.*, vol. 252, pp. 370–374, 2002.

[32] R. Di Corato *et al.*, “Magnetic hyperthermia efficiency in the cellular environment for different nanoparticle designs,” *Biomaterials*, vol. 35, no. 24, pp. 6400–6411, Aug. 2014.

[33] P. Reimer and B. Tombach, “Hepatic MRI with SPIO: detection and characterization of focal liver lesions,” *Eur. Radiol.*, vol. 8, no. 7, pp. 1198–1204, 1998.

[34] D. Yoo, J.-H. Lee, T.-H. Shin, and J. Cheon, “Theranostic Magnetic Nanoparticles,” *Acc. Chem. Res.*, vol. 44, no. 10, pp. 863–874, Oct. 2011.

[35] A. J. Cole, V. C. Yang, and A. E. David, “Cancer theranostics: the rise of targeted magnetic nanoparticles,” *Trends Biotechnol.*, vol. 29, no. 7, pp. 323–332, Jul. 2011.

[36] R. Hergt, S. Dutz, and M. Zeisberger, “Validity limits of the Néel relaxation model of magnetic nanoparticles for hyperthermia,” *Nanotechnology*, vol. 21, no. 1, p. 15706, Jan. 2010.

[37] A. Ahlbom *et al.*, “Guidelines for limiting exposure to time-varying electric, magnetic, and electromagnetic fields (up to 300 GHz),” *Health Phys.*, vol. 74, no. 4, pp. 494–521, 1998.

[38] R. M. Ferguson, A. P. Khandhar, C. Jonasson, J. Blomgren, C. Johansson, and Krishnan, “Size-Dependent Relaxation Properties of Monodisperse Magnetite Nanoparticles Measured Over Seven Decades of Frequency by AC Susceptometry,” *IEEE Trans. Magn.*, vol. 49, no. 7, pp. 3441–3444, Jul. 2013.

[39] W. F. Brown Jr, “Thermal fluctuations of a single-domain particle,” *Phys. Rev.*, vol. 130, no. 5, p. 1677, 1963.

[40] O. M. Bucci, G. Bellizzi, and G. G. Bellizzi, “Microwave Broadband Characterization of a Diluted Water-Based Ferrofluid in Presence of a Polarizing Magnetic Field,” *IEEE Trans. Magn.*, pp. 1–1, 2016.

[41] P. C. Fannin, S. W. Charles, and T. Relihan, “On the broadband measurement of the permittivity and magnetic susceptibility of ferrofluids,” *J. Magn. Magn. Mater.*, vol. 167, no. 3, pp. 274–280, 1997.

[42] O. Ayala-Valenzuela *et al.*, “Magnetite-cobalt ferrite nanoparticles for kerosene-based magnetic fluids,” *J. Magn. Magn. Mater.*, vol. 294, no. 2, pp. e37–e41, Jul. 2005.

[43] F. Ahrentorp *et al.*, “Sensitive high frequency AC susceptometry in magnetic nanoparticle applications,” in *AIP Conference Proceedings*, 2010, vol. 1311, pp. 213–223.

[44] E. Garaio, J. M. Collantes, F. Plazaola, J. A. Garcia, and I. Castellanos-Rubio, “A multifrequency eletromagnetic applicator with an integrated AC magnetometer for magnetic hyperthermia experiments,” *Meas. Sci. Technol.*, vol. 25, no. 11, p. 115702, Nov. 2014.

[45] E. Garaio *et al.*, “A wide-frequency range AC magnetometer to measure the specific absorption rate in nanoparticles for magnetic hyperthermia,” *J. Magn. Magn. Mater.*, vol. 368, pp. 432–437, Nov. 2014.

[46] V. Connord, B. Mehdaoui, R. P. Tan, J. Carrey, and M. Respaud, “An air-cooled Litz wire coil for measuring the high frequency hysteresis loops of magnetic samples—A useful setup for magnetic hyperthermia applications,” *Rev. Sci. Instrum.*, vol. 85, no. 9, p. 93904, 2014.

[47] K. Iizuka, “An agar-agar chamber for study of electromagnetic waves in an inhomogeneous medium,” *IEEE Trans. Antennas Propag.*, vol. 19, no. 3, pp. 365–377, 1971.

[48] V. Patsula, M. Moskvin, S. Dutz, and D. Horák, “Size-dependent magnetic properties of iron oxide nanoparticles,” *J. Phys. Chem. Solids*, vol. 88, pp. 24–30, Jan. 2016.

[49] R. Hergt *et al.*, “Enhancement of AC-losses of magnetic nanoparticles for heating applications,” *J. Magn. Magn. Mater.*, vol. 280, no. 2–3, pp. 358–368, Sep. 2004.

[50] D. Serantes *et al.*, “Influence of dipolar interactions on hyperthermia properties of ferromagnetic particles,” *J. Appl. Phys.*, vol. 108, no. 7, p. 73918, 2010.

[51] Suriyanto, E. Y. K. Ng, and S. D. Kumar, “Physical mechanism and modeling of heat generation and transfer in magnetic fluid hyperthermia through Néelian and Brownian relaxation: a review,” *Biomed. Eng. OnLine*, vol. 16, no. 1, Dec. 2017.

[52] A. Fanti, M. B. Lodi, and G. Mazzarella, “Enhancement of Cell Migration Rate Toward a Superparamagnetic Scaffold Using LF Magnetic Fields,” *IEEE Trans. Magn.*, vol. 52, no. 10, pp. 1–8, Oct. 2016.

[53] F. J. German, G. K. Gothard, and L. S. Riggs, “Modelling of materials with electric and magnetic losses with the symmetrical condensed TLM method,” *Electron. Lett.*, vol. 26, no. 16, pp. 1307–1308, 1990.

[54] J. P. Reilly, “Peripheral nerve stimulation by induced electric currents: exposure to time-varying magnetic fields,” *Med. Biol. Eng. Comput.*, vol. 27, no. 2, p. 101, 1989.

[55] U. Gneveckow *et al.*, “Description and characterization of the novel hyperthermia- and thermoablation-system MFH®300F for clinical magnetic fluid hyperthermia,” *Med. Phys.*, vol. 31, no. 6, pp. 1444–1451, May 2004.

[56] T. O. Tasci, I. Vargel, A. Arat, E. Guzel, P. Korkusuz, and E. Atalar, “Focused RF hyperthermia using magnetic fluids: Focused RF hyperthermia using magnetic fluids,” *Med. Phys.*, vol. 36, no. 5, pp. 1906–1912, Apr. 2009.

[57] B. Gleich and J. Weizenecker, “Tomographic imaging using the nonlinear response of magnetic particles,” *Nature*, vol. 435, no. 7046, pp. 1214–1217, Jun. 2005.

[58] B. Mehdaoui *et al.*, “Influence of a transverse static magnetic field on the magnetic hyperthermia properties and high-frequency hysteresis loops of ferromagnetic FeCo nanoparticles,” *Appl. Phys. Lett.*, vol. 100, no. 5, p. 52403, 2012.

[59] Z. W. Tay *et al.*, “Magnetic Particle Imaging-Guided Heating *in Vivo* Using Gradient Fields for Arbitrary Localization of Magnetic Hyperthermia Therapy,” *ACS Nano*, vol. 12, no. 4, pp. 3699–3713, Apr. 2018.

[60] E. Myrovali, N. Maniotis, A. Makridis, K. Simeonidis, T. Samaras, and M. Angelakeris, “Regional Focus effect on Magnetic Particle Hyperthermia efficiency,” in *2018 EMF-Med 1st World Conference on Biomedical Applications of Electromagnetic Fields (EMF-Med)*, 2018, pp. 1–2.

[61] G. Bellizzi, O. M. Bucci, and G. Chirico, “Numerical assessment of a criterion for the optimal choice of the operative conditions in magnetic nanoparticle hyperthermia on a realistic model of the human head,” *Int. J. Hyperthermia*, vol. 32, no. 6, pp. 688–703, Aug. 2016.

[62] P. R. Stauffer, P. K. Sneed, H. Hashemi, and T. L. Phillips, “Practical induction heating coil designs for clinical hyperthermia with ferromagnetic implants,” *IEEE Trans. Biomed. Eng.*, vol. 41, no. 1, pp. 17–28, 1994.

[63] S. Zinn and S. L. Semiatin, “Coil design and fabrication: basic design and modifications,” *Heat Treat.*, vol. 12, no. 3, pp. 32–36, 1988.

[64] I. Connell, “Design of Radio-Frequency Arrays for Ultra-High Field MRI,” *Electron. Thesis Diss. Repos.*, Jan. 2017.

[65] J. Mispelter, M. Lupu, and A. Briguet, *NMR Probeheads for Biophysical and Biomedical Experiments: Theoretical Principles & Practical Guidelines*. Imperial College Press, 2006.

[66] E. M. Haacke, R. W. Brown, M. R. Thompson, and R. Venkatesan, *Magnetic resonance imaging: physical principles and sequence design*, vol. 82. Wiley-Liss New York:, 1999.

[67] J. T. Vaughan and J. R. Griffiths, *RF coils for MRI*. John Wiley & Sons, 2012.

[68] P. B. Roemer, W. A. Edelstein, C. E. Hayes, S. P. Souza, and O. M. Mueller, “The NMR phased array,” *Magn. Reson. Med.*, vol. 16, no. 2, pp. 192–225, 1990.

[69] D. K. Sodickson and W. J. Manning, “Simultaneous acquisition of spatial harmonics (SMASH): fast imaging with radiofrequency coil arrays,” *Magn. Reson. Med.*, vol. 38, no. 4, pp. 591–603, 1997.

[70] K. P. Pruessmann, M. Weiger, M. B. Scheidegger, and P. Boesiger, “SENSE: sensitivity encoding for fast MRI,” *Magn. Reson. Med.*, vol. 42, no. 5, pp. 952–962, 1999.

[71] M. Weiger, K. P. Pruessmann, and P. Boesiger, “Cardiac real-time imaging using SENSE,” *Magn. Reson. Med. Off. J. Int. Soc. Magn. Reson. Med.*, vol. 43, no. 2, pp. 177–184, 2000.

[72] J. A. de Zwart, P. J. Ledden, P. Kellman, P. van Gelderen, and J. H. Duyn, “Design of a SENSE-optimized high-sensitivity MRI receive coil for brain imaging,” *Magn. Reson. Med.*, vol. 47, no. 6, pp. 1218–1227, Jun. 2002.

[73] J. A. de Zwart, P. J. Ledden, P. van Gelderen, J. Bodurka, R. Chu, and J. H. Duyn, “Signal-to-noise ratio and parallel imaging performance of a 16-channel receive-only brain coil array at 3.0 Tesla,” *Magn. Reson. Med.*, vol. 51, no. 1, pp. 22–26, Jan. 2004.

[74] B. Keil and L. L. Wald, “Massively parallel MRI detector arrays,” *J. Magn. Reson.*, vol. 229, pp. 75–89, Apr. 2013.

[75] C. H. Moon, J.-H. Kim, T. Zhao, and K. T. Bae, “Quantitative ^{23}Na MRI of human knee cartilage using dual-tuned ^{1}H/^{23}Na transceiver array radiofrequency coil at 7 tesla: 7T ^{23}Na MRI of Knee Cartilage,” *J. Magn. Reson. Imaging*, vol. 38, no. 5, pp. 1063–1072, Nov. 2013.

[76] A. Abuelhaija, S. Orzada, and K. Solbach, “Parasitic element based decoupling of 7 tesla MRI coil array,” in *2015 Loughborough Antennas & Propagation Conference (LAPC)*, 2015, pp. 1–5.

[77] G. Adriany *et al.*, “A 32-channel lattice transmission line array for parallel transmit and receive MRI at 7 tesla,” *Magn. Reson. Med.*, vol. 63, no. 6, pp. 1478–1485, Jun. 2010.

[78] A. M. Maunder, M. Daneshmand, P. Mousavi, B. G. Fallone, and N. De Zanche, “Stray Capacitance Between Magnetic Resonance Imaging Coil Elements: Models and Application to Array Decoupling,” *IEEE Trans. Microw. Theory Tech.*, vol. 61, no. 12, pp. 4667–4677, Dec. 2013.

[79] M. Alecci, S. Romanzetti, J. Kaffanke, A. Celik, H. P. Wegener, and N. J. Shah, “Practical design of a 4 Tesla double-tuned RF surface coil for interleaved 1H and 23Na MRI of rat brain,” *J. Magn. Reson.*, vol. 181, no. 2, pp. 203–211, Aug. 2006.

[80] M. Meyerspeer, E. S. Roig, R. Gruetter, and A. W. Magill, “An improved trap design for decoupling multinuclear RF coils,” *Magnetic Resonance in Medicine*, 01-Aug-2014. .

[81] J. V. Rispoli, I. E. Dimitrov, S. Cheshkov, C. Malloy, S. M. Wright, and M. P. McDougall, “Trap design and construction for high-power multinuclear magnetic resonance experiments,” *Concepts Magn. Reson. Part B Magn. Reson. Eng.*, vol. 46B, no. 4, pp. 162–168, Oct. 2016.

[82] U. Zanovello, M. Borsero, D. Giordano, L. Zilberti, F. Maggiorelli, and G. Tiberi, “Experimental Setup to Compare Measurements and Numerical Simulations in Magnetic Resonance Imaging RF Dosimetry,” *IEEE Trans. Instrum. Meas.*, vol. 66, no. 6, pp. 1208–1216, Jun. 2017.

[83] B. Park, T. Neuberger, A. G. Webb, D. C. Bigler, and C. M. Collins, “Faraday shields within a solenoidal coil to reduce sample heating: Numerical comparison of designs and experimental verification,” *J. Magn. Reson.*, vol. 202, no. 1, pp. 72–77, Jan. 2010.

[84] G. Adriany and R. Gruetter, “A half-volume coil for efficient proton decoupling in humans at 4 tesla,” *J. Magn. Reson.*, vol. 125, pp. 178–184, 1997.

[85] Y. Li, Z. Xie, Y. Pang, D. Vigneron, and X. Zhang, “ICE decoupling technique for RF coil array designs,” *Med. Phys.*, vol. 38, no. 7, pp. 4086–4093, 2011.

[86] X. Yan, X. Zhang, L. Wei, and R. Xue, “Magnetic wall decoupling method for monopole coil array in ultrahigh field MRI: a feasibility test,” *Quant. Imaging Med. Surg.*, vol. 4, no. 2, pp. 79–86, Apr. 2014.

[87] E. Georget *et al.*, “Stacked magnetic resonators for MRI RF coils decoupling,” *J. Magn. Reson.*, vol. 275, pp. 11–18, Feb. 2017.

[88] N. I. Avdievich, J. W. Pan, and H. P. Hetherington, “Resonant inductive decoupling (RID) for transceiver arrays to compensate for both reactive and resistive components of the mutual impedance,” *NMR Biomed.*, vol. 26, no. 11, pp. 1547–1554, Nov. 2013.

[89] B. Wu, P. Qu, C. Wang, J. Yuan, and G. X. Shen, “Interconnecting L/C components for decoupling and its application to low-field open MRI array,” *Concepts Magn. Reson. Part B Magn. Reson. Eng.*, vol. 31B, no. 2, pp. 116–126, Apr. 2007.

[90] C. von Morze *et al.*, “An eight-channel, nonoverlapping phased array coil with capacitive decoupling for parallel MRI at 3 T,” *Concepts Magn. Reson. Part B Magn. Reson. Eng.*, vol. 31B, no. 1, pp. 37–43, Feb. 2007.

[91] X. Zhang and A. Webb, “Design of a capacitively decoupled transmit/receive NMR phased array for high field microscopy at 14.1T,” *J. Magn. Reson.*, vol. 170, no. 1, pp. 149–155, Sep. 2004.

[92] K. M. Gilbert, A. T. Curtis, J. S. Gati, L. M. Klassen, and R. S. Menon, “A radiofrequency coil to facilitate B 1+ shimming and parallel imaging acceleration in three dimensions at 7 T,” *NMR Biomed.*, vol. 24, no. 7, pp. 815–823, Aug. 2011.

[93] I. R. O. Connell and R. S. Menon, “General Coupling Matrix Synthesis for Decoupling MRI RF Arrays,” *IEEE Trans. Med. Imaging*, vol. 35, no. 10, pp. 2229–2242, Oct. 2016.

[94] I. R. O. Connell, K. M. Gilbert, M. A. Abou-Khousa, and R. S. Menon, “MRI RF Array Decoupling Method With Magnetic Wall Distributed Filters,” *IEEE Trans. Med. Imaging*, vol. 34, no. 4, pp. 825–835, Apr. 2015.

[95] I. R. O. Connell, K. M. Gilbert, M. A. Abou-Khousa, and R. S. Menon, “Design of a Parallel Transmit Head Coil at 7T With Magnetic Wall Distributed Filters,” *IEEE Trans. Med. Imaging*, vol. 34, no. 4, pp. 836–845, Apr. 2015.

[96] J. B. Pendry, A. J. Holden, D. J. Robbins, and W. J. Stewart, “Magnetism from conductors and enhanced nonlinear phenomena,” *IEEE Trans. Microw. Theory Tech.*, vol. 47, no. 11, pp. 2075–2084, 1999.

[97] A. Sihvola, “Metamaterials in electromagnetics,” *Metamaterials*, vol. 1, no. 1, pp. 2–11, Mar. 2007.

[98] S. A. Tretyakov, “Complex-media electromagnetics and metamaterials,” *J. Opt.*, vol. 19, no. 8, p. 84006, Aug. 2017.

[99] D. R. Smith, J. B. Pendry, and M. C. Wiltshire, “Metamaterials and negative refractive index,” *Science*, vol. 305, no. 5685, pp. 788–792, 2004.

[100] F. Bilotti, A. Toscano, L. Vegni, K. Aydin, K. B. Alici, and E. Ozbay, “Equivalent-Circuit Models for the Design of Metamaterials Based on Artificial Magnetic Inclusions,” *IEEE Trans. Microw. Theory Tech.*, vol. 55, no. 12, pp. 2865–2873, Dec. 2007.

[101] W. Withayachumnankul, C. Fumeaux, and D. Abbott, “Compact electric-LC resonators for metamaterials,” *Opt. Express*, vol. 18, no. 25, pp. 25912–25921, 2010.

[102] C. R. Simovski, “Bloch material parameters of magneto-dielectric metamaterials and the concept of Bloch lattices,” *Metamaterials*, vol. 1, no. 2, pp. 62–80, Dec. 2007.

[103] A. Alù, “First-principles homogenization theory for periodic metamaterials,” *Phys. Rev. B*, vol. 84, no. 7, Aug. 2011.

[104] D. R. Smith and J. B. Pendry, “Homogenization of metamaterials by field averaging (invited paper),” *JOSA B*, vol. 23, no. 3, pp. 391–403, Mar. 2006.

[105] M. G. Silveirinha, “Metamaterial homogenization approach with application to the characterization of microstructured composites with negative parameters,” *Phys. Rev. B*, vol. 75, no. 11, Mar. 2007.

[106] R. Marqués, F. Martin, and M. Sorolla, *Metamaterials with negative parameters: theory, design, and microwave applications*, vol. 183. John Wiley & Sons, 2011.

[107] K. Aydin, I. Bulu, K. Guven, M. Kafesaki, C. M. Soukoulis, and E. Ozbay, “Investigation of magnetic resonances for different split-ring resonator parameters and designs,” *New J. Phys.*, vol. 7, pp. 168–168, Aug. 2005.

[108] K. B. Alici, F. Bilotti, L. Vegni, and E. Ozbay, “Optimization and tunability of deep subwavelength resonators for metamaterial applications: complete enhanced transmission through a subwavelength aperture,” *Opt. Express*, vol. 17, no. 8, pp. 5933–5943, 2009.

[109] N. Fontana, F. Costa, G. Tiberi, L. Nigro, and A. Monorchio, “Distributed trap FSS filter for dual tuned RF MRI coil decoupling at 7.0 T,” in *2017 International Conference on Electromagnetics in Advanced Applications (ICEAA)*, 2017, pp. 1229–1231.

[110] U. S. Pranav, S. Sudheesh, P. Stanly, S. Sankar, R. Devika, and A. Pradeep, “Metamaterial Based Energy Harvester,” *Procedia Comput. Sci.*, vol. 93, pp. 74–80, 2016.

[111] T. S. Almoneef and O. M. Ramahi, “Metamaterial electromagnetic energy harvester with near unity efficiency,” *Appl. Phys. Lett.*, vol. 106, no. 15, p. 153902, Apr. 2015.

[112] C. Fowler and J. Zhou, “A metamaterial-inspired approach to RF energy harvesting,” *ArXiv Prepr. ArXiv170507718*, 2017.

[113] J. D. Baena, R. Marqués, F. Medina, and J. Martel, “Artificial magnetic metamaterial design by using spiral resonators,” *Phys. Rev. B*, vol. 69, no. 1, Jan. 2004.

[114] F. Falcone *et al.*, “Stop-band and band-pass characteristics in coplanar waveguides coupled to spiral resonators,” *Microw. Opt. Technol. Lett.*, vol. 42, no. 5, pp. 386–388, Sep. 2004.

[115] F. Bilotti, A. Toscano, and L. Vegni, “Design of Spiral and Multiple Split-Ring Resonators for the Realization of Miniaturized Metamaterial Samples,” *IEEE Trans. Antennas Propag.*, vol. 55, no. 8, pp. 2258–2267, Aug. 2007.

[116] H. Mosallaei and K. Sarabandi, “Magneto-Dielectrics in Electromagnetics: Concept and Applications,” *IEEE Trans. Antennas Propag.*, vol. 52, no. 6, pp. 1558–1567, Jun. 2004.

[117] F. Costa, A. Monorchio, and G. Manara, “Efficient analysis of frequency-selective surfaces by a simple equivalent-circuit model,” *IEEE Antennas Propag. Mag.*, vol. 54, no. 4, pp. 35–48, 2012.

[118] F. Costa, A. Monorchio, and G. Manara, “An overview of equivalent circuit modeling techniques of frequency selective surfaces and metasurfaces,” *Appl Comput Electromagn Soc J*, vol. 29, no. 12, pp. 960–976, 2014.

[119] B. Wu, X. Zhang, P. Qu, and G. X. Shen, “Design of an inductively decoupled microstrip array at 9.4T,” *J. Magn. Reson.*, vol. 182, no. 1, pp. 126–132, Sep. 2006.

[120] Y. Cheng and Y. Shu, “A New Analytical Calculation of the Mutual Inductance of the Coaxial Spiral Rectangular Coils,” *IEEE Trans. Magn.*, vol. 50, no. 4, pp. 1–6, Apr. 2014.

[121] G. Dambrine, A. Cappy, F. Heliodore, and E. Playez, “A new method for determining the FET small-signal equivalent circuit,” *IEEE Trans. Microw. Theory Tech.*, vol. 36, no. 7, pp. 1151–1159, 1988.

[122] R. E. Collin, “Field Theory of Guided Waves 2nd edn (Piscataway, NJ: IEEE),” 1990.

[123] D. Schieber, “On the inductance of printed spiral coils,” *Electr. Eng. Arch. Elektrotechnik*, vol. 68, no. 3, pp. 155–159, 1985.

[124] H. A. Wheeler, “Simple inductance formulas for radio coils,” *Proc. Inst. Radio Eng.*, vol. 16, no. 10, pp. 1398–1400, 1928.

[125] S. S. Mohan, M. del Mar Hershenson, S. P. Boyd, and T. H. Lee, “Simple accurate expressions for planar spiral inductances,” *IEEE J. Solid-State Circuits*, vol. 34, no. 10, pp. 1419–1424, 1999.

[126] F. W. Grover, *Inductance calculations: working formulas and tables*. Courier Corporation, 2004.

[127] G. Giovannetti, N. Fontana, A. Monorchio, M. Tosetti, and G. Tiberi, “Estimation of losses in strip and circular wire conductors of radiofrequency planar surface coil by using the finite element method,” *Concepts Magn. Reson. Part B Magn. Reson. Eng.*, vol. 47B, no. 3, p. e21358, Jul. 2017.

[128] G. Giovannetti, G. Tiberi, M. Tosetti, A. Monorchio, and N. Fontana, “Radiofrequency planar surface coil for magnetic resonance: When the use of a circular wire gives a noticeable advantage with respect to a flat strip conductor?,” *Measurement*, vol. 129, pp. 518–522, Dec. 2018.

[129] R. Stara *et al.*, “Validation of numerical approaches for electromagnetic characterization of magnetic resonance radiofrequency coils,” *Prog. Electromagn. Res.*, vol. 29, pp. 121–136, 2013.

[130] W. C. Brown, “The history of wireless power transmission,” *Sol. Energy*, vol. 56, no. 1, pp. 3–21, 1996.

[131] A. S. Marincic, “Nikola tesla and the wireless transmission of energy,” *IEEE Trans. Power Appar. Syst.*, no. 10, pp. 4064–4068, 1982.

[132] A. P. Sample, D. A. Meyer, and J. R. Smith, “Analysis, Experimental Results, and Range Adaptation of Magnetically Coupled Resonators for Wireless Power Transfer,” *IEEE Trans. Ind. Electron.*, vol. 58, no. 2, pp. 544–554, Feb. 2011.

[133] B. Choi, J. Nho, H. Cha, T. Ahn, and S. Choi, “Design and Implementation of Low-Profile Contactless Battery Charger Using Planar Printed Circuit Board Windings as Energy Transfer Device,” *IEEE Trans. Ind. Electron.*, vol. 51, no. 1, pp. 140–147, Feb. 2004.

[134] Guoxing Wang, Wentai Liu, M. Sivaprakasam, and G. A. Kendir, “Design and analysis of an adaptive transcutaneous power telemetry for biomedical implants,” *IEEE Trans. Circuits Syst. Regul. Pap.*, vol. 52, no. 10, pp. 2109–2117, Oct. 2005.

[135] A. K. RamRakhyani, S. Mirabbasi, and M. Chiao, “Design and Optimization of Resonance-Based Efficient Wireless Power Delivery Systems for Biomedical Implants,” *IEEE Trans. Biomed. Circuits Syst.*, vol. 5, no. 1, pp. 48–63, Feb. 2011.

[136] A. K. RamRakhyani and G. Lazzi, “Multi-coil approach to reduce electromagnetic energy absorption for wirelessly powered implants,” *Healthc. Technol. Lett.*, vol. 1, no. 1, pp. 21–25, Jan. 2014.

[137] C.-S. Wang, O. H. Stielau, and G. A. Covic, “Design considerations for a contactless electric vehicle battery charger,” *IEEE Trans. Ind. Electron.*, vol. 52, no. 5, pp. 1308–1314, 2005.

[138] N. M. Neihart and R. R. Harrison, “Micropower Circuits for Bidirectional Wireless Telemetry in Neural Recording Applications,” *IEEE Trans. Biomed. Eng.*, vol. 52, no. 11, pp. 1950–1959, Nov. 2005.

[139] J. Huh, S. W. Lee, W. Y. Lee, G. H. Cho, and C. T. Rim, “Narrow-Width Inductive Power Transfer System for Online Electrical Vehicles,” *IEEE Trans. Power Electron.*, vol. 26, no. 12, pp. 3666–3679, Dec. 2011.

[140] M. Song, P. Belov, and P. Kapitanova, “Wireless power transfer inspired by the modern trends in electromagnetics,” *Appl. Phys. Rev.*, vol. 4, no. 2, p. 21102, 2017.

[141] J. Shin *et al.*, “Design and Implementation of Shaped Magnetic-Resonance-Based Wireless Power Transfer System for Roadway-Powered Moving Electric Vehicles,” *IEEE Trans. Ind. Electron.*, vol. 61, no. 3, pp. 1179–1192, Mar. 2014.

[142] A. K. RamRakhyani and G. Lazzi, “On the Design of Efficient Multi-Coil Telemetry System for Biomedical Implants,” *IEEE Trans. Biomed. Circuits Syst.*, vol. 7, no. 1, pp. 11–23, Feb. 2013.

[143] M. Catrysse, B. Hermans, and R. Puers, “An inductive power system with integrated bi-directional data-transmission,” *Sens. Actuators Phys.*, vol. 115, no. 2–3, pp. 221–229, Sep. 2004.

[144] M. Ghovanloo and K. Najafi, “A Wireless Implantable Multichannel Microstimulating System-on-a-Chip With Modular Architecture,” *IEEE Trans. Neural Syst. Rehabil. Eng.*, vol. 15, no. 3, pp. 449–457, Sep. 2007.

[145] G. Wang, W. Liu, M. Sivaprakasam, M. Zhou, J. D. Weiland, and M. S. Humayun, "A dual band wireless power and data telemetry for retinal prosthesis," in *Engineering in Medicine and Biology Society, 2006. EMBS'06. 28th Annual International Conference of the IEEE*, 2006, pp. 4392–4395.

[146] M. R. Haider, S. K. Islam, S. Mostafa, M. Zhang, and T. Oh, "Low-Power Low-Voltage Current Readout Circuit for Inductively Powered Implant System," *IEEE Trans. Biomed. Circuits Syst.*, vol. 4, no. 4, pp. 205–213, Aug. 2010.

[147] J.-Y. Lee and B.-M. Han, "A Bidirectional Wireless Power Transfer EV Charger Using Self-Resonant PWM," *IEEE Trans. Power Electron.*, vol. 30, no. 4, pp. 1784–1787, Apr. 2015.

[148] A. Qusba, A. K. RamRakhyani, J.-H. So, G. J. Hayes, M. D. Dickey, and G. Lazzi, "On the Design of Microfluidic Implant Coil for Flexible Telemetry System," *IEEE Sens. J.*, vol. 14, no. 4, pp. 1074–1080, Apr. 2014.

[149] A. Kurs, A. Karalis, R. Moffatt, J. D. Joannopoulos, P. Fisher, and M. Soljačić, "Wireless power transfer via strongly coupled magnetic resonances," *science*, vol. 317, no. 5834, pp. 83–86, 2007.

[150] B. L. Cannon, J. F. Hoburg, D. D. Stancil, and S. C. Goldstein, "Magnetic Resonant Coupling As a Potential Means for Wireless Power Transfer to Multiple Small Receivers," *IEEE Trans. Power Electron.*, vol. 24, no. 7, pp. 1819–1825, Jul. 2009.

[151] T. P. Duong and J.-W. Lee, "Experimental Results of High-Efficiency Resonant Coupling Wireless Power Transfer Using a Variable Coupling Method," *IEEE Microw. Wirel. Compon. Lett.*, vol. 21, no. 8, pp. 442–444, Aug. 2011.

[152] M. Kiani, Uei-Ming Jow, and M. Ghovanloo, "Design and Optimization of a 3-Coil Inductive Link for Efficient Wireless Power Transmission," *IEEE Trans. Biomed. Circuits Syst.*, vol. 5, no. 6, pp. 579–591, Dec. 2011.

[153] F. Liu, Y. Yang, D. Jiang, X. Ruan, and X. Chen, "Modeling and Optimization of Magnetically Coupled Resonant Wireless Power Transfer System With Varying Spatial Scales," *IEEE Trans. Power Electron.*, vol. 32, no. 4, pp. 3240–3250, Apr. 2017.

[154] A. K. RamRakhyani and G. Lazzi, "Multicoil Telemetry System for Compensation of Coil Misalignment Effects in Implantable Systems," *IEEE Antennas Wirel. Propag. Lett.*, vol. 11, pp. 1675–1678, 2012.

[155] A. K. RamRakhyani and G. Lazzi, "Interference-free wireless power transfer system for biomedical implants using multi-coil approach," *Electron. Lett.*, vol. 50, no. 12, pp. 853–855, May 2014.

[156] M. Machnoor, E. S. G. Rodriguez, P. Kosta, J. Stang, and G. Lazzi, "Analysis and Design of a 3-Coil Wireless Power Transmission System for Biomedical Applications," *IEEE Trans. Antennas Propag.*, pp. 1–1, 2018.

[157] Y. Urzhumov and D. R. Smith, "Metamaterial-enhanced coupling between magnetic dipoles for efficient wireless power transfer," *Phys. Rev. B*, vol. 83, no. 20, May 2011.

[158] E. S. Gamez Rodriguez, A. K. RamRakhyani, D. Schurig, and G. Lazzi, "Compact Low-Frequency Metamaterial Design for Wireless Power Transfer Efficiency Enhancement," *IEEE Trans. Microw. Theory Tech.*, vol. 64, no. 5, pp. 1644–1654, May 2016.

[159] L. Li, H. Liu, H. Zhang, and W. Xue, "Efficient Wireless Power Transfer System Integrating With Metasurface for Biological Applications," *IEEE Trans. Ind. Electron.*, vol. 65, no. 4, pp. 3230–3239, Apr. 2018.

[160] A. Rajagopalan, A. K. RamRakhyani, D. Schurig, and G. Lazzi, "Improving Power Transfer Efficiency of a Short-Range Telemetry System Using Compact Metamaterials," *IEEE Trans. Microw. Theory Tech.*, vol. 62, no. 4, pp. 947–955, Apr. 2014.

[161] D. Ahn, M. Kiani, and M. Ghovanloo, "Enhanced Wireless Power Transmission Using Strong Paramagnetic Response," *IEEE Trans. Magn.*, vol. 50, no. 3, pp. 96–103, Mar. 2014.

[162] E. S. Gamez Rodriguez, M. Machnoor, and G. Lazzi, "On the Generation of Nondiffracting Beams in Extremely Subwavelength Applications," *IEEE Trans. Antennas Propag.*, vol. 65, no. 10, pp. 5228–5237, Oct. 2017.

[163] U.-M. Jow and M. Ghovanloo, "Geometrical Design of a Scalable Overlapping Planar Spiral Coil Array to Generate a Homogeneous Magnetic Field," *IEEE Trans. Magn.*, vol. 49, no. 6, pp. 2933–2945, Jun. 2013.

[164] K. Hatanaka *et al.*, "Power transmission of a desk with a cord-free power supply," *IEEE Trans. Magn.*, vol. 38, no. 5, pp. 3329–3331, Sep. 2002.

[165] D. Ahn and S. Hong, "Effect of Coupling Between Multiple Transmitters or Multiple Receivers on Wireless Power Transfer," *IEEE Trans. Ind. Electron.*, vol. 60, no. 7, pp. 2602–2613, Jul. 2013.

[166] M. Kiani and M. Ghovanloo, "The Circuit Theory Behind Coupled-Mode Magnetic Resonance-Based Wireless Power Transmission," *IEEE Trans. Circuits Syst. Regul. Pap.*, vol. 59, no. 9, pp. 2065–2074, Sep. 2012.

[167] W.-C. Chen, C. M. Bingham, K. M. Mak, N. W. Caira, and W. J. Padilla, "Extremely subwavelength planar magnetic metamaterials," *Phys. Rev. B*, vol. 85, no. 20, May 2012.

[168] B. Wang, K. H. Teo, T. Nishino, W. Yerazunis, J. Barnwell, and J. Zhang, "Experiments on wireless power transfer with metamaterials," *Appl. Phys. Lett.*, vol. 98, no. 25, p. 254101, Jun. 2011.

[169] Y. Zhao and E. Leelarasmee, "Controlling the resonances of indefinite materials for maximizing efficiency in wireless power transfer," *Microw. Opt. Technol. Lett.*, vol. 56, no. 4, pp. 867–875, Apr. 2014.

[170] H. Kim and C. Seo, "Highly efficient wireless power transfer using metamaterial slab with zero refractive property," *Electron. Lett.*, vol. 50, no. 16, pp. 1158–1160, Jul. 2014.

[171] Y. Zhao, V. Vutipongsatorn, and E. Leelarasmee, "Improving the efficiency of wireless power transfer systems using metamaterials," in *2013 10th International Conference on Electrical Engineering/Electronics, Computer, Telecommunications and Information Technology*, 2013, pp. 1–4.

[172] A. L. A. K. Ranaweera, T. P. Duong, and J.-W. Lee, "Experimental investigation of compact metamaterial for high efficiency mid-range wireless power transfer applications," *J. Appl. Phys.*, vol. 116, no. 4, p. 43914, Jul. 2014.

[173] V. G. Veselago, "Electrodynamics of substances with simultaneously negative electrical and magnetic permeabilities," *Phys.-Uspekhi*, vol. 10, no. 4, pp. 504–509, 1968.

[174] J. Pendry, "Manipulating the Near Field With Metamaterials," *Opt. Photonics News*, vol. 15, no. 9, pp. 32–37, Sep. 2004.

[175] J. B. Pendry, "Negative refraction makes a perfect lens," *Phys. Rev. Lett.*, vol. 85, no. 18, p. 3966, 2000.

[176] A. Grbic and G. V. Eleftheriades, "Growing evanescent waves in negative-refractive-index transmission-line media," *Appl. Phys. Lett.*, vol. 82, no. 12, pp. 1815–1817, Mar. 2003.

[177] J. Choi and C. H. Seo, "High-efficiency wireless energy transmission using magnetic resonance based on negative refractive index metamaterial," *Prog. Electromagn. Res.*, vol. 106, pp. 33–47, 2010.

[178] C. L. Holloway, A. Dienstfrey, E. F. Kuester, J. F. O'Hara, A. K. Azad, and A. J. Taylor, "A discussion on the interpretation and characterization of metafilms/metasurfaces: The two-dimensional equivalent of metamaterials," *Metamaterials*, vol. 3, no. 2, pp. 100–112, Oct. 2009.

[179] J.-F. Chen *et al.*, "Metamaterial-based high-efficiency wireless power transfer system at 13.56 MHz for low power applications," *Prog. Electromagn. Res.*, vol. 72, pp. 17–30, 2017.

[180] T. Shaw, A. Roy, and D. Mitra, "Efficiency enhancement of wireless power transfer system using MNZ metamaterials," *Prog. Electromagn. Res.*, vol. 68, pp. 11–19, 2016.

[181] Z. Zhang, B. Zhang, B. Deng, X. Wei, and J. Wang, "Opportunities and challenges of metamaterial-based wireless power transfer for electric vehicles," *Wirel. Power Transf.*, vol. 5, no. 1, pp. 9–19, Mar. 2018.

[182] K. Chen and Z. Zhao, "Analysis of the Double-Layer Printed Spiral Coil for Wireless Power Transfer," *IEEE J. Emerg. Sel. Top. Power Electron.*, vol. 1, no. 2, pp. 114–121, Jun. 2013.

[183] H. Zhu, X. Luo, C. Zhao, Z. Hong, and Z. Huang, "Design and optimization of deep sub-wavelength metamaterials using a hybrid search algorithm," in *2017 IEEE Wireless Power Transfer Conference (WPTC)*, 2017, pp. 1–4.

[184] E. F. Kuester, M. A. Mohamed, M. Piket-May, and C. L. Holloway, "Averaged transition conditions for electromagnetic fields at a metafilm," *IEEE Trans. Antennas Propag.*, vol. 51, no. 10, pp. 2641–2651, Oct. 2003.

[185] M. C. K. Wiltshire, J. B. Pendry, W. Williams, and J. V. Hajnal, "An effective medium description of 'Swiss Rolls', a magnetic metamaterial," *J. Phys. Condens. Matter*, vol. 19, no. 45, p. 456216, Nov. 2007.

[186] C. L. Holloway, M. A. Mohamed, E. F. Kuester, and A. Dienstfrey, "Reflection and Transmission Properties of a Metafilm: With an Application to a Controllable Surface Composed of Resonant Particles," *IEEE Trans. Electromagn. Compat.*, vol. 47, no. 4, pp. 853–865, Nov. 2005.

[187] C. L. Holloway, E. F. Kuester, and A. Dienstfrey, “Characterizing Metasurfaces/Metafilms: The Connection Between Surface Susceptibilities and Effective Material Properties,” *IEEE Antennas Wirel. Propag. Lett.*, vol. 10, pp. 1507–1511, 2011.

[188] D. R. Smith, S. Schultz, P. Markoš, and C. M. Soukoulis, “Determination of effective permittivity and permeability of metamaterials from reflection and transmission coefficients,” *Phys. Rev. B*, vol. 65, no. 19, Apr. 2002.

APPENDIX A

A.1 RF MRI coils and SRs interactions: a physical interpretation

The theoretical approach described in the section 2.4.1 can be usefully interpreted through an equivalent physical interpretation. Referring to a medium characterized by a complex magnetic permeability μ, the magnetic flux produced by a coil *i* concatenated with the surface of a second coil *j* can be expressed as:

$$\Phi_{ij_{eff}} = \oiint_j \overrightarrow{b_i} \cdot \overrightarrow{i_n} dS = \mu_r \oiint_j \mu_0 \overrightarrow{h_i} \cdot \overrightarrow{i_n} dS = \mu_r \Phi_{ij_0} \tag{A.1}$$

where we defined $\overrightarrow{h_i}$ as the magnetic field produced by the coil *i* and Φ_{ij_0} as the magnetic flux in vacuum. Thus, it follows that the mutual coupling coefficient is dependent from an equivalent fictitious relative magnetic permeability μ_r, when the medium is not the vacuum:

$$M_{ij_{eff}} = \frac{\mu_r \Phi_{ij_0}}{I_i} = \mu_r M_{ij_0} \tag{A.2}$$

In our specific case, the insertion of the SRs in proximity of the RF coils produces an equivalent effect as to change the magnetic properties of the medium describing the inductive link. Thus, from eq. (2.20) we can extract this fictitious effective complex magnetic permeability through some algebraic manipulation:

$$\begin{aligned} Z_{12_{eff}} &= j\omega M_{12} - \frac{j\omega^3 N M_{13} M_{23} X_3}{R_3^2 + \omega^2 X_3^2} + \frac{\omega^2 N M_{13} M_{23} R_3}{R_3^2 + \omega^2 X_3^2} = \\ &= j\omega M_{12} \left(1 - \frac{\omega^2 N M_{13} M_{23} X_3}{M_{12}(R_3^2 + \omega^2 X_3^2)} - \frac{j\omega N M_{13} M_{23} R_3}{M_{12}(R_3^2 + \omega^2 X_3^2)}\right) \end{aligned} \tag{A.3}$$

Now, we can define:

$$\begin{aligned} \mu_r(\omega) &= \mu_r'(\omega) - j\mu_r''(\omega) = \\ &\left(1 - \frac{\omega^2 N M_{13} M_{23} X_3}{M_{12}(R_3^2 + \omega^2 X_3^2)}\right) - j \frac{\omega N M_{13} M_{23} R_3}{M_{12}(R_3^2 + \omega^2 X_3^2)} \end{aligned} \tag{A.4}$$

The decoupling approach described in section 2.4.1 is equal to null the real term and to make negligible the loss term of the equivalent complex magnetic permeability. Nullifying the real term leads to consider a medium with magnetic susceptibility equal to -1, thus realizing a perfect diamagnetic medium. In this sense, the medium (i.e. the SRs) reacts to the applied H field with a magnetization of the same amplitude but opposite sign, thus making null the mutual coupling between the MRI RF coils 1 and 2.

$$M = \chi_m H = -H \tag{A.5}$$

The introduced fictitious complex magnetic permeability is useful to give an alternative interpretation of the inductive link between the MRI RF coils, due to the presence of the SRs placed in between, explaining the procedure from a physical point of view rather than a circuital one.